DISSERTATION

IMPACTS OF HISTORIC ANTHROPOGENIC AEROSOL FORCING ON LARGE CLIMATE ENSEMBLES THROUGH THE LENS OF POLEWARD ENERGY TRANSPORT

Submitted by

Michael Robert Needham

Department of Atmospheric Science

In partial fulfillment of the requirements

For the Degree of Doctor of Philosophy

Colorado State University

Fort Collins, Colorado

Fall 2024

Doctoral Committee:

Advisor: David A. Randall

Maria Rugenstein
Peter Jan van Leeuwen
Jeremy Rugenstein

ABSTRACT

IMPACTS OF HISTORIC ANTHROPOGENIC AEROSOL FORCING ON LARGE CLIMATE ENSEMBLES THROUGH THE LENS OF POLEWARD ENERGY TRANSPORT

In discussions of the human impact on Earth's climate, aerosols receive much less attention than greenhouse gases. And yet, the change in the global mean effective radiative forcing from anthropogenic aerosols was roughly of the same magnitude (but of opposite sign) as the change in greenhouse gases throughout much of the twentieth century. Aerosols also represent the largest uncertainty in the effective radiative forcing, due to their complex interactions with clouds and solar radiation. Complicating this even further, aerosols are relatively short-lived within the atmosphere, and thus exhibit a large degree of variability in space and time.

This dissertation presents a set of studies which investigate the ways in which historic anthropogenic aerosols may have impacted the Earth's weather and climate, through the analysis of a large number historic climate model simulations which comprise so-called large ensembles. Analysis of these ensembles allows for the isolation of some forced signal (e.g., the influence of aerosols) from the noise (i.e., the background variability of the model). This leads to conclusions through the analysis of summary statistics across members of the ensemble population which would be impossible to make based on only one or a few simulations .

In particular, these studies show that the emission of aerosol precursors from Europe and North America increased the northward transport of heat from the southern into the northern hemisphere in an ensemble of simulations performed with version 2 of the Community Earth System Model (CESM2). The additional heat transport was in excess of 0.25 PW. This is an increase of at least 4-5% compared to the baseline maximum transport of between 5-6 PW which occurs in the mid-latitudes. At latitudes away from these maxima, the increase was a much larger percentage of the total.

This anomalous northward energy transport was accomplished by changes in both atmospheric and oceanic processes. These include a southward shift of the Intertropical Convergence Zone (ITCZ) associated with changes in the Hadley cells; an increase in the frequency of extratropical cyclones in the north Atlantic; a strengthening of the Atlantic Meridional Overturning Circulation (AMOC); as well as changes to multiple ocean processes across the Indo-Pacific. Comparison of these results to the literature indicates that this modeled response to aerosols in CESM2 is likely too large.

Furthermore, analysis of two additional large ensembles reveals that this over-sensitivity of CESM2 cannot be due to some deficiency in the model. Instead, it is demonstrated that the difference is the result of changes to the historical emission estimates between phase 5 and phase 6 of the Coupled Model Intercomparison Project (i.e., CMIP5 and CMIP6). This finding leads to the hypothesis that the higher interannual variability associated with a change from decadal-scale CMIP5 emissions to annual-scale CMIP6 emissions is the ultimate cause of the overzealous response of the model. Testing this hypothesis likely will provide the most fertile ground for future work.

ACKNOWLEDGEMENTS

This work would not have been possible without the guidance of David Randall, who served as my advisor for the six years I spent at Colorado State. I would also like to thank Maria Rugenstein, Peter Jan van Leeuwen, and Jeremy Rugenstein who sat on my doctoral committee. In addition, I want to express my gratitude to all of the students, faculty, and staff of the Department of Atmospheric Science. Lastly, I want to acknowledge all of the support I have received from my family over these past six years.

DEDICATION

To my family, especially Kelsey, Jude, and Etta

TABLE OF CONTENTS

LIST OF FIGURES

Chapter 1

Introduction: The Industrial Revolution, Air Pollution, and Links to Weather and Climate

1.1 Air Pollution Controls

From the perspective of the mid-2020s, proper stewardship of the environment is inextricably tied to the reduction of emissions of carbon dioxide and related greenhouse gases (Gulev et al. (2021)) due to their propensity to trap heat within the climate system. It is interesting to juxtapose this contemporary perspective with the early history the environmental movement, when carbon dioxide was essentially ignored. Instead, the focus was on more immediate concerns within the framework of the relationship between human beings and their environment, such as ambient air quality, toxic pollutants, and visibility in cities and national parks (United States Environmental Protection Agency, 2023).

This focus was entirely because of lived experience. Following the onset of the industrial revolution, formerly agrarian societies in Europe and North America became more urbanized as people moved away from the countryside towards factory and manufacturing jobs in cities, which were becoming increasingly crowded. This industrial activity was primarily powered by coal which, when burned for power, releases air pollutants like sulfur dioxide (SO_2) and soot. These industrial-sector coal emissions, alongside those from burning coal to support the growing population, contributed to poor ambient air quality (see Fig. 1.1) that regularly caused respiratory problems and was seen as a fact of life in many industrialized cities (Hanlon, 2020); the “smoky fog" endemic to 19th and early-20th century London is said to have inspired the portmanteau *smog*. Occasionally, when combined with certain meteorological conditions, this pollution could become trapped close to the surface and reach lethal concentrations: the first century or so after industrialization is littered with air pollution episodes with names like The

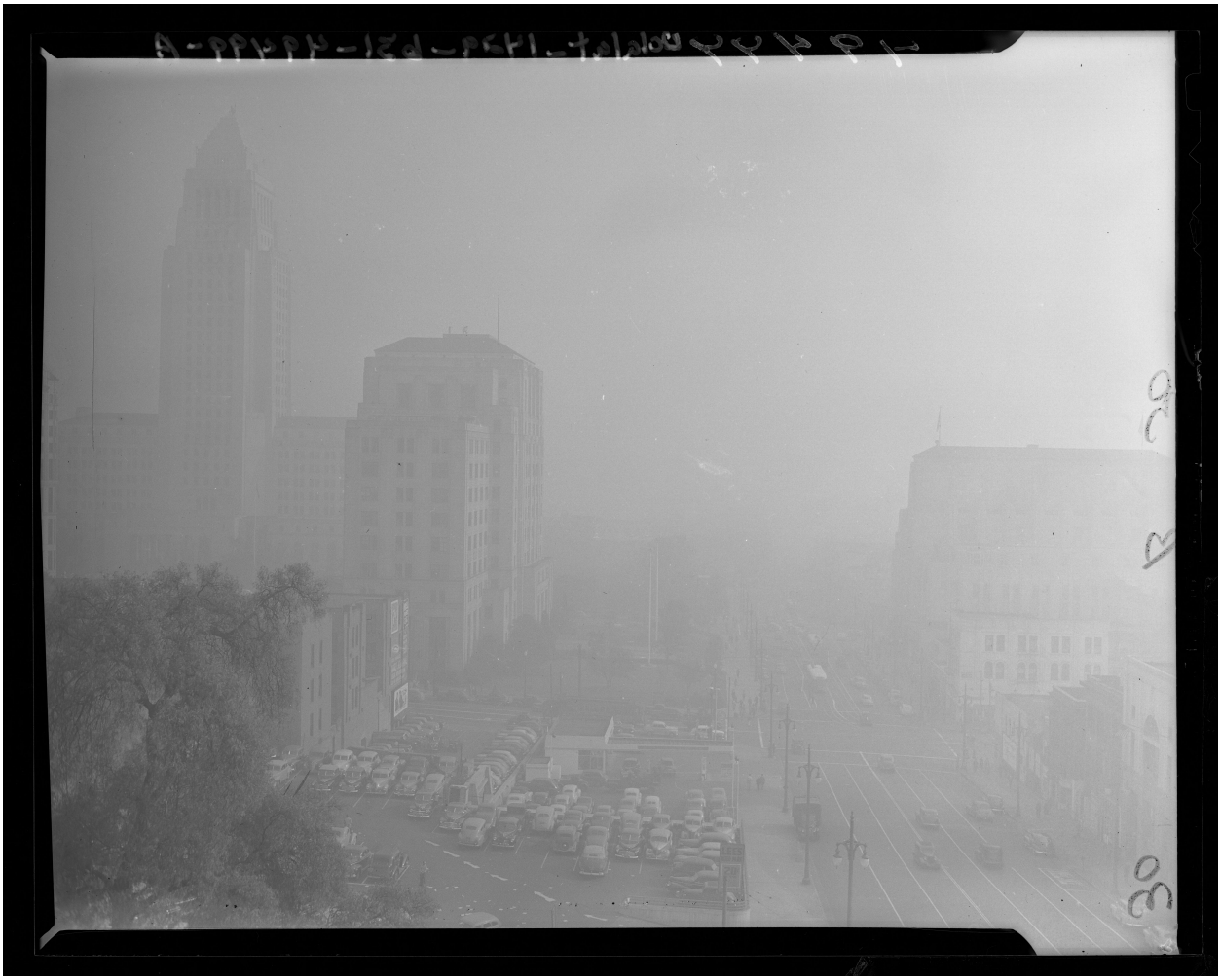

Figure 1.1: Photograph published by the Los Angeles Times on January 6, 1948, originally captioned "CIVIC CENTER DEFIED [sic] – Here is a view of part of the Civic Center yesterday when the eye-smarting smog was at its worst. The picture was taken from First and Olive Sts."; accessed via UCLA Library. Licensed under Creative Commons Attribution 4.0 International License

Great Smog of London[1] which led to the deaths of an estimated 4000 people over a five-day period in 1952 (City of London, 2022). It was against this backdrop that the many causes of air pollution were studied and eventually regulated through air quality legislation.

By the time of the passage of the 1970 Amendments to the Clean Air Act in the United States, the scientific understanding of air pollution had evolved to the point that the legislation was crafted to specifically target six common air pollutants for reduction. Among these six so-called “critera pollutants" was SO_2, which is produced by sources such as electricity generation, indus-

[1] Dramatized in episode 4 of the first season of Netflix’s *The Crown*

trial processes, and some tailpipe emissions (United States Environmental Protection Agency, 2023) among other, smaller sources. SO_2 exposure can lead to respiratory problems and also contributes to the formation of both smog and acid rain.

Over the last 50 years, the regulatory efforts targeting SO_2 and other criteria pollutants have been extremely effective in improving ambient air quality in the United States, with similar legislation leading to similarly improved air quality in many European countries. From the standpoint of human health, this is an unmitigated success. Estimates suggest that the Clean Air Act, as amended, prevents as many as 230,000 premature deaths every year in the United States (United States Environmental Protection Agency, 2011). Reductions in SO_2 have also contributed to reductions in acid rain as well as improvements in visibility at America's national parks.

Less commonly cited are the impacts of SO_2 emissions on weather and climate. SO_2 is one of the primary chemical precursors to sulfate aerosols, which can impact the earth's radiative balance by directly scattering incoming sunlight, or indirectly (Twomey, 1977; Albrecht, 1989) through changing the optical properties of clouds. In simple terms, these aerosols tend to *cool* the climate by scattering solar radiation and so work in opposition to planet-warming greenhouse gases (Gulev et al., 2021).

These radiative impacts lead to substantial impacts on weather and climate, which will be discussed in full in subsequent chapters. The overarching theme of this dissertation is to investigate the impact of anthropogenic emissions of industrial pollutants (using SO_2 as a bellwether for a wide range of chemical species) on weather and climate throughout the post-industrial period from 1850 to the near-present, as simulated by a state-of-the-art global earth system model (CESM2). Taken at face value, the model results suggest that these changes were felt across wide regions of the globe ranging from the tropics to the poles

It should not be surprising that that a forcing of this magnitude (Hoesly et al., 2018; Gulev et al., 2021) would be felt across many aspects of the climate. However the interconnected character of the system (i.e., through the coupling of the atmosphere, ocean, and cryosphere)

indicates a certain level of complexity, with the potential for numerous two-way interactions between different components. Then, to make this problem more tractable we will utilize as an overarching framework the basic thermodynamic requirement that the earth system redistributes incoming energy from the sun. This energetic perspective places certain constraints on the various aspects of the system, which we can leverage better understand these complicated relationships.

1.2 The Earth's Poleward Energy Transport

Poleward heat transport is a fundamental aspect of the earth system. More radiation is absorbed than emitted in the tropics, while the opposite is true near the poles. This simple observation, along with the assumption that the Earth is in energy balance with the outside universe implies a net transport of energy from lower to higher latitudes; a fact that has been known for many decades (Sverdrup, 1942; Riehl and Malkus, 1958; Bjerknes, 1964; Oort, 1971; Vonder Haar and Oort, 1973; Oort and Vonder Haar, 1976; Stone, 1978, see Fig. 1.2). The total meridional heat transport by the earth system could in principle be accomplished by any combination of atmospheric, oceanic, or solid-earth processes. In practice transport by the solid-earth (e.g. conduction, ground-water flow, plate tectonics) is negligible, and the vast majority of transport occurs via fluid flows in the atmosphere and oceans (Held, 2001; Trenberth and Stepaniak, 2004).

The poleward energy transport (hereafter PET) is not merely an abstract theoretical concept, but is instead directly related to many physical processes in the atmosphere and oceans. Indeed, one reason to study the PET is because it allows for a conceptual framework in which to connect seemingly unrelated aspects of the earth system. As an example, the requirement that the Atmosphere export energy from the tropics was crucial to the initial understanding of the existence and behavior of the Intertropical Convergence Zone (Riehl and Malkus, 1958; Neelin and Held, 1987), and the energetic theory of the ITCZ's position (e.g., Bischoff and Schneider, 2014; Schneider et al., 2014) allowed for an understanding of the connection between the ITCZ and the Atlantic Meridional Overturning Circulation (Chiang and Bitz, 2005; Frierson et al.,

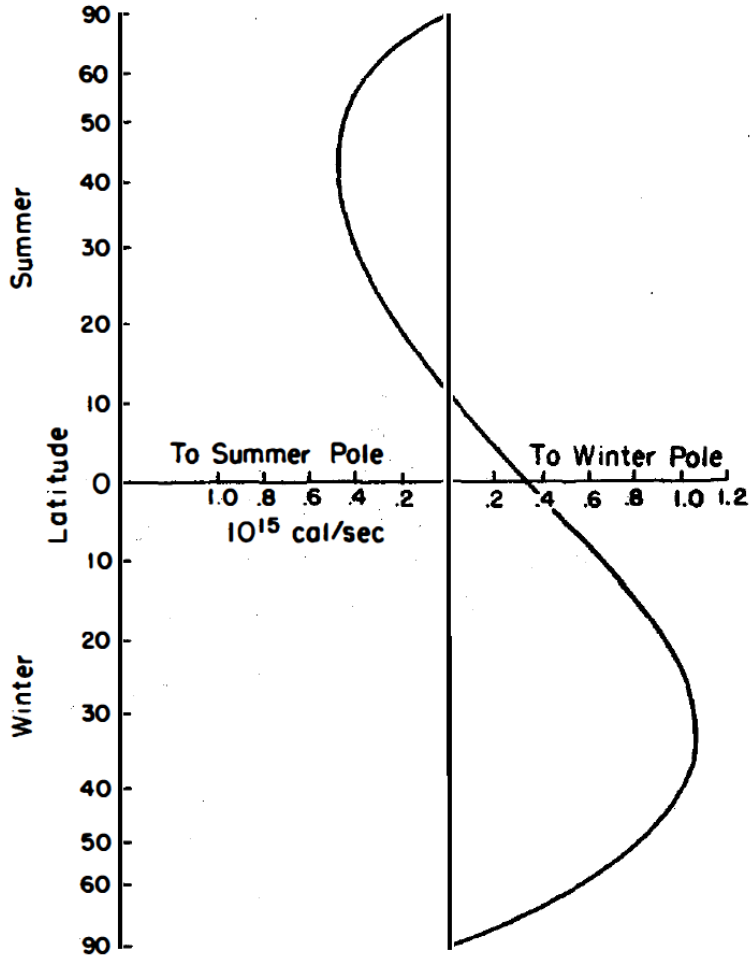

Figure 1.2: Originally published as Fig. 3 from Riehl and Malkus (1958). An estimate of the magnitude and meridional structure of the Earth's poleward transport based on observations from the 1950s. Note that even thought observations are entirely from the northern Hemisphere (using data from summer and winter seasons) the peak transport of about 1.1×10^{15} cal/sec (roughly 4.6 Petawatts, from the conversion factor of 4.184 Joules/calorie) is more or less correct.

2013; Donohoe et al., 2013; Bischoff and Schneider, 2014; Schneider et al., 2014; Moreno-Chamarro et al., 2019). In a general sense, the motivation for this approach is to show that the theoretical constraints of the PET can be used to generate testable hypotheses on how the earth system may respond to a particular forcing - in this case, in response to historic anthropogenic aerosol forcing.

As discussed in the previous section, the first century or so of industrialization was characterized by horrendous pollution that contributed to dangerous levels of air quality in many cities in Europe and North America. This pollution (particularly but not exclusively SO_2) also

impacted the earth's radiation budget by reflecting a large amount of additional solar radiation back to space relative to pre-industrial levels (Gulev et al., 2021). Unlike CO_2 (the twenty-*first* century's most discussed pollutant, which is long-lived and thus well-mixed throughout the atmosphere), industrial pollutants like SO_2 (and their chemical successor species like sulfuric acid) are relatively short lived and thus are typically spatially limited to the regions downwind from the source of emission. Then, their net radiative impact (from combining their direct impact with indirect implacts through their influence on clouds) is spatially *inhomogeneous*. For the period following the onset of industrialization, this meant that the radiative impact of these pollutants was largely confined to the midlatitudes of the northern hemisphere (roughly 30°-60°N), where pollution reduced the amount of solar radiation reaching the surface.

In broad terms (which will be expanded upon in subsequent chapters), this radiative impact meant that the northern mid-latitudes reflected more sunlight back to space compared to pre-industrial levels - while at the same time the tropical regions (in which the largest amount of solar radiation is absorbed) remained largely unaffected. This increased the temperature contrast between the equator and the northern middle latitudes. Consequently more energy needed to be transported in order to balance this energetic contrast. The specific ways that the atmosphere and oceans accomplished this additional heat transport is the focus of this thesis.

1.3 Segue

Before jumping into analysis of the impacts of aerosol emissions on weather and climate during the twentieth century, we must first develop the theoretical foundations of the poleward energy transport (PET), which will serve as our overarching framework. This leads us to Chapter 2 which provides the necessary theoretical background of the PET, alongside an overview of the radiative impact of historic anthropogenic aerosol emissions.

References

Albrecht, B. A. (1989). Aerosols, cloud microphysics, and fractional cloudiness. *Science*, 245(4923):1227–1230.

Bischoff, T. and Schneider, T. (2014). Energetic constraints on the position of the intertropical convergence zone. *J. Clim.*, 27(13):4937–4951.

Bjerknes, J. (1964). Atlantic Air-Sea interaction. *Adv. Geophys.*, 10:1–82.

Chiang, J. C. H. and Bitz, C. M. (2005). Influence of high latitude ice cover on the marine intertropical convergence zone. *Clim. Dyn.*, 25(5):477–496.

City of London (2022). 70 years since the great london smog. `https://www.london.gov.uk/programmes-strategies/environment-and-climate-change/environment-and-climate-change-publications/70-years-great-london-smog`. Accessed: 2024-4-17.

Donohoe, A., Marshall, J., Ferreira, D., and Mcgee, D. (2013). The relationship between ITCZ location and Cross-Equatorial atmospheric heat transport: From the seasonal cycle to the last glacial maximum. *J. Clim.*, 26(11):3597–3618.

Frierson, D. M. W., Hwang, Y.-T., Fučkar, N. S., Seager, R., Kang, S. M., Donohoe, A., Maroon, E. A., Liu, X., and Battisti, D. S. (2013). Contribution of ocean overturning circulation to tropical rainfall peak in the northern hemisphere. *Nat. Geosci.*, 6(11):940–944.

Gulev, S. K., Thorne, P. W., Ahn, J., Dentener, F. J., Domingues, C. M., Gerland, S., Gong, D., Kaufman, D. S., Nnamchi, H. C., Quaas, J., Rivera, J. A., Sathyendranath, S., Smith, S. L., Trewin, B., von Shuckmann, K., and Vose, R. S. (2021). Changing state of the climate system. In Masson-Delmotte, V., Zhai, P., Pirani, A., Connors, S. L., Péan, C., Berger, S., Caud, N., Chen, Y., Goldfarb, L., Gomis, M. I., Huang, M., Leitzell, K., Lonnoy, E., Matthews, J. B. R., Maycock, T. K., Waterfield, T., Yelekçi, O., Yu, R., and Zhou, B., editors, *Climate Change 2021: The Physical Science Basis. Contribution of Working Group I to the Sixth Assessment Report of the Intergovernmental Panel on Climate Change*, chapter 2. Cambridge University Press, Cambridge, United Kingdom and New York, NY, USA.

Hanlon, W. W. (2020). Coal smoke, city growth, and the costs of the industrial revolution. *Econ J*, 130(626):462–488.

Held, I. M. (2001). The partitioning of the poleward energy transport between the tropical ocean and atmosphere. *J. Atmos. Sci.*, 58(8):943–948.

Hoesly, R. M., Smith, S. J., Feng, L., Klimont, Z., Janssens-Maenhout, G., Pitkanen, T., Seibert, J. J., Vu, L., Andres, R. J., Bolt, R. M., Bond, T. C., Dawidowski, L., Kholod, N., Kurokawa, J.-I., Li, M., Liu, L., Lu, Z., Moura, M. C. P., O'Rourke, P. R., and Zhang, Q. (2018). Historical (1750–2014) anthropogenic emissions of reactive gases and aerosols from the community emissions data system (CEDS). *Geosci. Model Dev.*, 11(1):369–408.

Moreno-Chamarro, E., Marshall, J., and Delworth, T. L. (2019). Linking ITCZ migrations to the AMOC and north Atlantic/Pacific SST decadal variability. *J. Clim.*, 33(3):893–905.

Neelin, J. D. and Held, I. M. (1987). Modeling tropical convergence based on the moist static energy budget. *Mon. Weather Rev.*, 115(1):3–12.

Oort, A. H. (1971). The observed annual cycle in the meridional transport of atmospheric energy. *J. Atmos. Sci.*, 28(3):325–339.

Oort, A. H. and Vonder Haar, T. H. (1976). On the observed annual cycle in the Ocean-Atmosphere heat balance over the northern hemisphere. *J. Phys. Oceanogr.*, 6(6):781–800.

Riehl, H. and Malkus, J. S. (1958). On the heat balance in the equatorial trough zone. *Geophysica*, 6:503–537.

Schneider, T., Bischoff, T., and Haug, G. H. (2014). Migrations and dynamics of the intertropical convergence zone. *Nature*, 513(7516):45–53.

Stone, P. H. (1978). Constraints on dynamical transports of energy on a spherical planet. *Dyn. Atmos. Oceans*, 2(2):123–139.

Sverdrup, H. U. (1942). *The Oceans Their Physics, Chemistry, and General Biology*. Prentive-Hall, INC.

Trenberth, K. E. and Stepaniak, D. P. (2004). The flow of energy through the earth's climate system. *Q. J. R. Meteorol. Soc.*, 130(603):2677–2701.

Twomey, S. (1977). The influence of pollution on the shortwave albedo of clouds. *J. Atmos. Sci.*, 34(7):1149–1152.

United States Environmental Protection Agency (2011). The benefits and costs of the clean air act from 1990 to 2020. Technical report.

United States Environmental Protection Agency (2023). Our nation's air: Trends through 2022. `https://gispub.epa.gov/air/trendsreport/2023/#home`. Accessed: 2024-4-17.

Vonder Haar, T. H. and Oort, A. H. (1973). New estimate of annual poleward energy transport by northern hemisphere oceans. *J. Phys. Oceanogr.*, 3(2):169–172.

Chapter 2

Background, Data, and Methods

2.1 PET Theory and Background

In steady-state, the total PET (where “total" refers to the sum of atmospheric and oceanic) is typically calculated from the TOA fluxes of longwave and shortwave radiation (e.g., Hartmann, 2016). Once the total transport has been calculated, either the atmospheric or oceanic transport is calculated and the remaining component may be retrieved as a residual, or calculated independently (Oort, 1971; Vonder Haar and Oort, 1973; Oort and Vonder Haar, 1976; Trenberth, 1979; Trenberth and Caron, 2001; Pierrehumbert, 2002; Trenberth and Stepaniak, 2003b; Wunsch, 2005)

Interestingly, the total PET is usually *not* calculated from the vertical integral of the meridional advection of energy although this is not always the case (Armour et al., 2019; Cox et al., 2022). The reason for this is simply that the calculation from TOA fluxes is often much easier. Specifcally, it requires only two two-dimensional fields of the net longwave and shortwave radiation fluxes rather than four three dimensional fields of temperature, geopotential, specific humidity, and the meridional winds. Additionally, gridded atmospheric reanalysis products typically do not conserve mass, which can lead to problems accounting for the total energy transport (as discussed in the comment by Cox et al. (2023) regarding the study by Clark et al. (2022)). The calculation of the heat transport from radiative fluxes is based on the divergence theorem,

$$\iiint_V \Big(\nabla \cdot \mathbf{F}\Big) dV = \oiint_S \mathbf{F} \cdot \hat{n} dS, \tag{2.1}$$

and we briefly discuss it below.

Consider a region of the climate system ranging from the center of the earth to the top of the atmosphere (e.g., $0 < r < \infty$) and from the south pole to an arbitrary latitude φ_0 (e.g., $-\pi/2 <$

$\varphi < \varphi_0$), encompassing all longitudes[2]. Because it is a point with zero volume, the heat flux into or out of the south pole must be zero (e.g., $\mathbf{F}(-\pi/2, r) = 0$). For a similar reason, the heat flux into or out of the center of the earth must also be zero (e.g., $\mathbf{F}(\varphi, 0) = 0$)). With these simplifications, the surface integral in Eq. 2.1 can be split in two; a double integral over longitude and latitude, and double integral over longitude and altitude, which we rearrange[3] to

$$\overbrace{a\int_0^{\infty}\int_0^{2\pi}\mathbf{F}(\varphi'=\varphi,r')\,d\lambda'\,dr'}^{\text{Meridional Heat Flux}} = \underbrace{\iiint_V \Big(\nabla\cdot\mathbf{F}\Big)\,dV}_{\text{Heat Uptake}} - \overbrace{a^2\int_{-\frac{\pi}{2}}^{\varphi}\int_0^{2\pi}\mathbf{F}(\varphi',r'=\infty)\cos\varphi'\,d\lambda'\,d\varphi'}^{\text{Vertical Heat Flux}}. \tag{2.2}$$

Then, under the steady state assumption of no long term heat uptake or loss (i.e., the "Heat Uptake" term in Eq. 2.2 disappears), the net meridional export of energy is balanced by the net radiative input of energy across the top of the atmosphere. Finally, the time mean, zonally integrated meridional heat transport across a latitude φ_0 (e.g., $\overline{\Theta(\varphi_0)}^t$) can then be calculated as

$$\overline{\Theta_T(\varphi)}^t = 2\pi a^2 \int_{-\pi/2}^{\varphi_0} \overline{F_{LW}}^{t,\lambda} + \overline{F_{SW}}^{t,\lambda}\cos\varphi\,d\varphi, \tag{2.3}$$

where $\overline{F_{toa}}^{t,\lambda} = \overline{F_{LW}}^{t,\lambda} + \overline{F_{SW}}^{t,\lambda}$ is the time mean, zonal mean net flux of longwave and shortwave radiation across the top of the atmosphere.

If the region of consideration is changed to range from the center of the earth to the surface of the ocean (rather than to the top of the atmosphere), then a similar equation to Eq. 2.3 can

[2]This would be formally described as a spherical sector of the earth and atmosphere, centered on the south pole.

[3]The minus sign on the right hand side of Eq. 2.2 indicates that a net vertical flux *into* the region from the TOA must be balanced by a net meridional flux *out of* the region across the latitude φ. Different data sources have opposing sign conventions for (e.g.,) the top of atmosphere radiative flux, so Eq. 2.2 should be used with careful consideration to the physical direction of the heat and radiative fluxes.

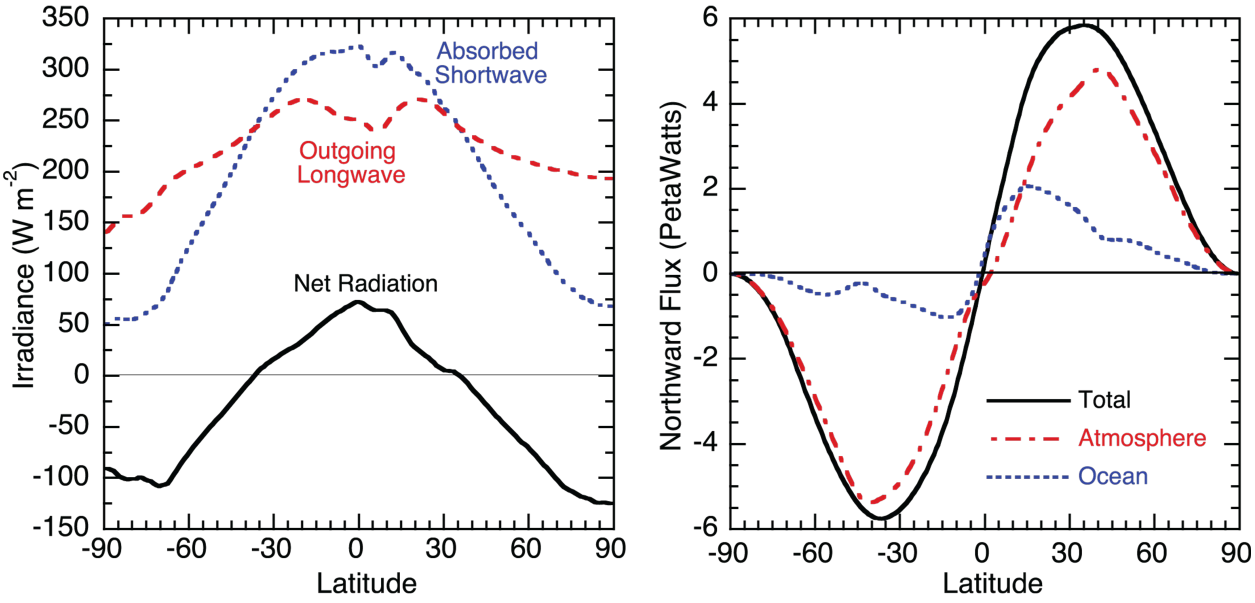

Figure 2.1: Left) The net flux of radiation at the top of the atmosphere, along with the net fluxes of the longwave and shortwave components. Right) The net poleward flux of energy calculated from the net TOA radiative flux in the left panel, along with contributions from Atmospheric and Oceanic transports. Both panels originally from Hartmann (2016), chapter 2.

be used to calculate the implied[4] heat transport by the oceans from surface fluxes of radiation and heat:

$$\overline{\Theta_S(\varphi_0)}^t = 2\pi a^2 \int_{-\pi/2}^{\varphi_0} \left(\overline{F_{LW}}^{t,\lambda} + \overline{F_{SW}}^{t,\lambda} + \overline{LE}^{t,\lambda} + \overline{SH}^{t,\lambda} \right) \cos\varphi d\varphi. \tag{2.4}$$

The difference between Eq. 2.3 and Eq. 2.4 then gives the atmospheric heat transport.

Eq. 2.3 can be referred to as the *energetic* method for calculating PET, as opposed to the *dynamic* method in which the left hand side of Eq. 2.2 is calculated directly by zonally and vertically integrating the meridional advection of energy by the atmosphere and oceans. A discussion of the dynamic and energetic methods is given by Armour et al. (2019), with further discussion by Donohoe et al. (2020) and Cox et al. (2022). Subsequent chapters utilize both methods for calculating the PET; utilization of the dynamic method in Ch. 4 was only possible because of the contribution of Tyler Cox, formerly of the University of Washington.

[4]Implied because the integral makes no explicit mention of the oceans compared to the solid earth. However in practice it is understood that the overwhelming majority of heat transport occurs in the oceans.

2.2 PET from Observations

Figure 2.1 shows the annual mean net flux of radiation across the top of the atmosphere (e.g., the integrand of Eq. 2.3), as well as the heat transport required by that distribution of radiative fluxes. The total transport (i.e., the solid black line in the right panel of Fig. 2.1) is a remarkably smooth (e.g., Trenberth and Stepaniak, 2003a) sinusoidal-like curve which is zero at the poles, reaches a maximum magnitude[5] near 35° of just below 6 petawatts in each hemisphere, and passes through zero near the equator. The red dash-dotted line in the right panel of Fig. 2.1 shows that the atmosphere accomplishes the lion's share of the transport at most latitudes, with the exception of the tropics in which the majority of the cross-equatorial transport occurs in the ocean (the blue dotted curve).

Another conclusion from Fig. 2.1 is that the distribution of shortwave radiation plays a larger role in setting the total energy transport than the longwave. As discussed in detail by Stone (1978), the total energy transport in steady-state is determined only by the top of atmosphere radiative fluxes. The outgoing longwave radiation ranges from a minimum value of about 150 Wm^{-2} at the south pole to a maximum value of about 250 Wm^{-2} on either side of the equator. In contrast, the absorbed solar radiation ranges from a minimum value of about 50 Wm^{-2} in the annual mean at the south pole, and a maximum value of greater than 300 Wm^{-2} at the equator. This is a range of 250 Wm^{-2} for the shortwave in contrast to a range of 100 Wm^{-2} for the longwave. Consistent with this interpretation, studies have shown that the total PET is particularly sensitive to processes which alter the distribution of absorbed solar radiation such as changes in polar ice and sulfate aerosols (Chiang and Bitz, 2005; Enderton and Marshall, 2009; Rose and Ferreira, 2012; Allen et al., 2015; Knietzsch et al., 2015; Irving et al., 2019; Lembo et al., 2019; Yukimoto et al., 2022; Shaw and Smith, 2022; Pearce and Bodas-Salcedo, 2023).

This observation - that the PET is particularly sensitive to processes which alter the absorbed solar radiation - provides the foundation for this thesis, in which we will analyze in detail

[5]Note that the "Net Radiation" in the left plot passes through zero at *exactly* the same latitude, illustrating the derivative-integral relationship between these two quantities.

the response of the PET to historic changes in shortwave absorption due to the influence of anthropogenic aerosols.

2.3 Anthropogenic Aerosol Forcing

2.3.1 Aerosol Indirect Radiative Effects

Aerosols are small particles of dust, salt, or other materials that are suspended in the atmosphere. The background level of aerosols contributes very little to the optical thickness of the atmosphere. However after dramatic events (e.g., volcanic eruptions, fires, and severe pollution), aerosols can significantly alter the local radiative characteristics. Aerosols impact the climate by changing the radiation balance, either through the direct scattering of incident radiation, or indirectly through their influence on clouds and precipitation (Petty, 2006; Gulev et al., 2021).

In addition to the direct scattering of radiation, aerosols *indirectly* impact the energy balance through their influence on clouds. The first indirect effect of aerosols (Twomey, 1977) is to increase the number of cloud condensation nuclei relative to a “pristine environment." A cloud with more CCN will tend to have droplets that are smaller because the mass of water is spread over a larger number of droplets. The second indirect effect of aerosols (Albrecht, 1989) increases the shortwave albedo by increasing the lifespan of clouds and reducing precipitation. In a polluted environment with an increased number of CCN, the precipitation rate is reduced because smaller cloud droplets are less likely to collide and coalesce into raindrops. The reduction in precipitation leads to clouds which persist longer than they otherwise would in a pristine environment. Both of these indirect effects act to increase the net shortwave albedo from clouds.

2.3.2 Historic Aerosol Trends

As mentioned in the previous chapter, the focus of this thesis is on the response of the atmosphere and oceans to historic aerosol forcing, through the framework of the PET. Fig. 2.2

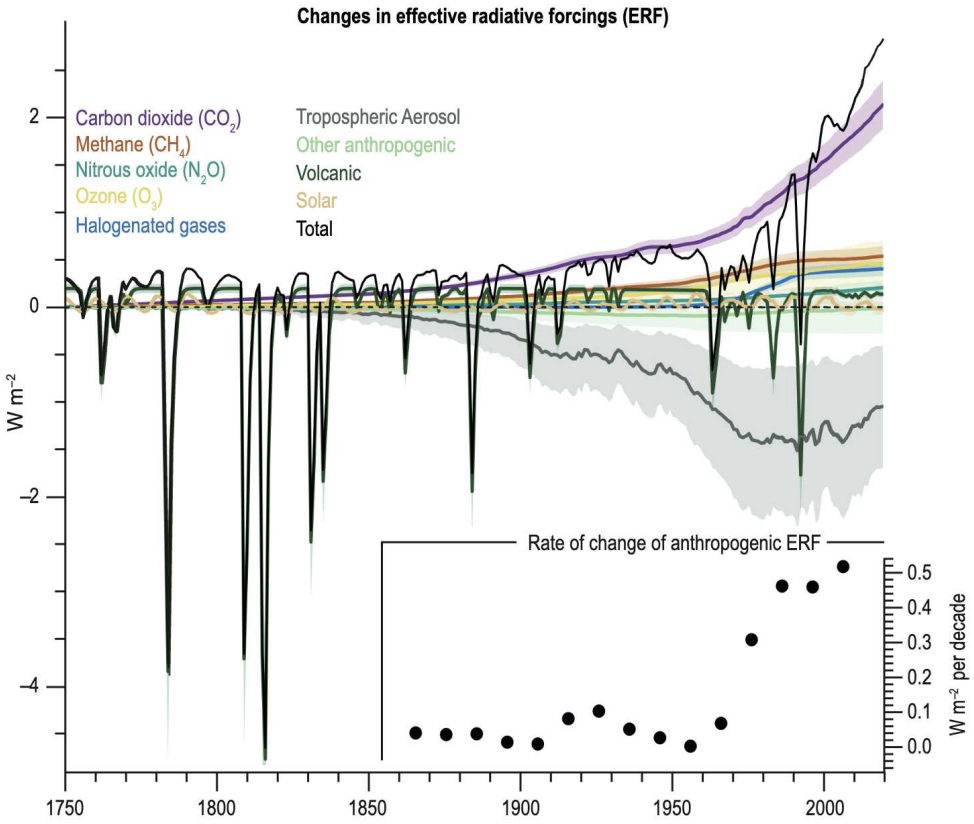

Figure 2.2: Estimated contribution to the global mean anomaly in effective radiative forcing from 1750-present from various anthropogenic and natural components. Originally published as Fig. 2.10 from chapter 2 of the Sixth Assessment Report by the International Panel on Climate Change (Gulev et al., 2021)

(originally from Gulev et al. (2021)) shows that tropospheric aerosols represent a large *negative* climate forcing that is of a similar magnitude to the *positive* climate forcing associated with greenhouse gases. Aerosols also represent the effective radiative forcing with the largest uncertainty, primarily due to the uncertain impact of aerosols on clouds (Zelinka et al., 2020; Wang et al., 2021).

The historic globally-integrated aerosol trend (i.e., the gray curve in Fig. 2.2) is characterized by a gradual increase in magnitude associated with increased pollution from industry, transportation, domestic uses (e.g., heating and cooking), agriculture, and other sources that peaks in the second half of the twentieth century (Hoesly et al., 2018; Gulev et al., 2021). The peak can be largely explained by an increasing awareness of the impact of pollutants on human health,

which led to the passage of air quality legislation in north America and western Europe (Brimblecombe, 2006; Aldy et al., 2020; Fowler et al., 2020). This legislation led to great improvements in public health for domestic populations, but also had the unintended impact of shifting the primary regions of aerosol emissions from western Europe and north America to east Asia and the Indian subcontinent (Hoesly et al., 2018) . The intended impact of early air quality legislation was to protect human health, and it was only later that the wider environmental impacts of pollution (e.g., acid rain, forest decline, and climate effects) became better understood (Fowler et al., 2020). An additional unintended impact of successful air pollution controls is to reduce the global aerosol burden which acts to increase the earth's energy imbalance (Hodnebrog et al., 2024).

2.4 Aerosols and Climate

Radiative forcing from aerosols deviates from that of greenhouse gases in a key way: greenhouse gases are long-lived and therefore well-mixed in the atmosphere, while aerosols are relatively short-lived so their radiative effects are primarily felt in the immediate region around the location of emission, or where the pollutants are transported by the winds (Fowler et al., 2020). Consequently, the climate impact of aerosols depends strongly on the location from which they are emitted (Shindell et al., 2010; Persad and Caldeira, 2018; Persad, 2023; Persad et al., 2023). The aerosol forcing has also been associated with an amplification of warming in the Arctic (Acosta Navarro et al., 2017; Deser et al., 2020; England et al., 2021; Aizawa et al., 2022).

2.4.1 Aerosol Impact on the ITCZ and Hadley Cells

This dependence on the location of emissions does not mean that aerosols' wider climate impacts (in contrast to direct and indirect radiative effects) are only felt locally. For example, the historic emissions of sulfur dioxide in the northern midlatitudes have been proposed as the root cause of southward shift of the tropical rainband during the late twentieth century (Hwang and Frierson, 2010; Allen et al., 2015), due to changes in the hemispheric difference in

absorbed solar radiation (Lembo et al., 2019; Irving et al., 2019; Yukimoto et al., 2022): as the northern hemisphere was cooled relative to the southern, the ITCZ shifted southward in order to transport additional energy northward, following the “energetic theory" (Donohoe et al., 2013; Bischoff and Schneider, 2014; Schneider et al., 2014) that the position of the ITCZ is determined by the requirement that the atmosphere balance the cross-equatorial energy imbalance between hemispheres. This theory predicts that the ITCZ shifts in response to a hemispheric difference in heating, although the magnitude of the shift is relatively small; approximately 3° of latitude toward the warmer hemisphere for each PW of hemispheric energy imbalance (Donohoe and Voigt, 2017).

2.4.2 Aerosol Impact on the AMOC

Arguably the most dramatic effect of aerosols on the climate is felt through their influence on the Atlantic meridional overturning circulation. The AMOC is the Atlantic branch of the global thermohaline circulation (Rahmstorf, 2002, 2003) and accomplishes a large percentage of the total poleward heat transport in the oceans (Bjerknes, 1964; Oort and Vonder Haar, 1976; Trenberth and Caron, 2001; Wunsch, 2005). The AMOC is understood to be a density-driven circulation; more specifically, it is driven by a meridional pressure gradient that is maintained when cold and salty (i.e., dense) surface water sinks in the north Atlantic. This formation of north Atlantic deep water is sensitive to processes which alter the sea surface density, and so the AMOC is considered to be particularly sensitive to outside forcings (Broecker, 1987, 1997; Lenton et al., 2008, 2019; Brovkin et al., 2021). This relationship is discussed in detail in Chapter 5.

2.5 Large Climate Ensembles for Isolating Forced Response from Internal Variability

The primary analysis chapters of this dissertation (Chs. 3-5) are exact republications of three scholarly articles published in peer-reviewed academic journals. As such they contain full de-

scriptions of the data and methods necessary for each study, so it would be redundant to discuss those points here. However a common feature of each of the studies is the utilization of large ensembles of historic climate simulations to separate the models' response to aerosol forcing from internal variability. Here, I will briefly discuss the overarching reason for why this ensembles approach has proven so useful for these studies.

The wider research question motivating these studies is to understand how the climate system responded to historic forcings, especially from anthropogenic aerosols, through the framework of the PET. The conclusion, based on analysis of a large ensemble of climate model simulations, is that historic anthropogenic aerosols altered the local shortwave radiative balance, which increased the energetic contrast between the tropics and midlatitudes, which in turn was balanced by anomalous poleward energy transport into the northern hemisphere. As we shall see in subsequent chapters, there is ample reason to believe that the *magnitude* of the response to aerosols is too large in CESM2, however this does not immediately indicate that the effect is entirely absent. Regardless, in the model this anomalous PET was accomplished in myriad ways; through alterations in both atmospheric and oceanic heat transports.

However it is important to keep in mind that these impacts are difficult to isolate from the background geophysical fluid commotion of the earth system. This challenge of separating the signal from the noise is made easier by utilizing a large number of simulations of the historic climate. The use of large ensembles presents a straightforward (but expensive) approach to this problem. The aggregate analysis of a number of simulations under the same external forcings - but with slightly different initial conditions - allows for isolation of the "forced response" of a particular model from the internal variability.

Take as an example the El Nino-Southern Oscillation, (ENSO, see NOAA Physical Sciences Laboratory, n.d.), which is understood to be one of the most significant modes of climate variability within the climate system. ENSO is *chaotic* in that its state at a particular instance is highly sensitive to previous conditions. For a collection of simulations initialized at slightly different states, the evolution of ENSO within each simulation will be independent from the

other simulations (i.e., for an arbitrary simulated year, the number of simulations in a particular ENSO state will roughly equal the number that would be predicted to be in that state by random chance). Put more simply, the average ENSO state across ensemble members (hereafter, the “ensemble mean") would be *extremely uninteresting*, because it is so largely determined by the internal variability of a given model than by any external forcing.

However, not all ensemble mean phenomena are so boring. In a general sense, whenever it is found that some phenomenon *is not* washed out in the ensemble mean, that observation provides evidence that the phenomenon is - at least to some degree - driven by external forcings which are common to all of the simulations. The work then moves to the quantification of the impact of external forcings compared to internal variability, and to the identification of which forcing(s) drive the phenomenon of interest. This is the approach taken in this work.

2.6 Segue

The two primary focuses of Chapter 3 are to first quantify the anomalous PET during the twentieth century in a large ensemble of historic climate simulations, and then to attribute that transport anomaly to anthropogenic aerosols. In Chapter 4, we further discuss this additional energy transport, and investigate the specific ways in which it was accomplished through changes in atmospheric and oceanic processes. Chapter 5 is concerned primarily with one of those oceanic processes - the Atlantic Meridional Overturning Circulation (AMOC), widely discussed as an important climatic “tipping-point" (e.g., Lenton et al., 2019). In Chapter 6, several additional topics are discussed briefly, all of which fall outside the scope of the primary, peer-reviewed chapters (i.e., Chs. 3-5). General conclusions are presented in the final chapter.

References

Juan C Acosta Navarro, Annica M L Ekman, Francesco S R Pausata, Anna Lewinschal, Vidya Varma, Øyvind Seland, Michael Gauss, Trond Iversen, Alf Kirkevåg, Ilona Riipinen, and Hans Christen Hansson. Future response of temperature and precipitation to reduced aerosol emissions as compared with increased greenhouse gas concentrations. *J. Clim.*, 30(3):939–954, February 2017. ISSN 0894-8755, 1520-0442. doi:10.1175/JCLI-D-16-0466.1.

Takuro Aizawa, Naga Oshima, and Seiji Yukimoto. Contributions of anthropogenic aerosol forcing and multidecadal internal variability to mid-20th century arctic cooling—CMIP6/DAMIP multimodel analysis. *Geophys. Res. Lett.*, 49(4), February 2022. ISSN 0094-8276, 1944-8007. doi:10.1029/2021gl097093.

B A Albrecht. Aerosols, cloud microphysics, and fractional cloudiness. *Science*, 245(4923):1227–1230, September 1989. ISSN 0036-8075. doi:10.1126/science.245.4923.1227.

Joseph E Aldy, Maximilian Auffhammer, Maureen L Cropper, Richard D Morgenstern, and Arthur G Fraas. Looking back at 50 years of the clean air act of 1970. *Resources Magazine*, May 2020.

Robert J Allen, Amato T Evan, and Ben B B Booth. Interhemispheric aerosol radiative forcing and tropical precipitation shifts during the late twentieth century. *J. Clim.*, 28(20):8219–8246, October 2015. ISSN 0894-8755, 1520-0442. doi:10.1175/JCLI-D-15-0148.1.

Kyle C Armour, Nicholas Siler, Aaron Donohoe, and Gerard H Roe. Meridional atmospheric heat transport constrained by energetics and mediated by Large-Scale diffusion. *J. Clim.*, 32(12): 3655–3680, June 2019. ISSN 0894-8755, 1520-0442. doi:10.1175/JCLI-D-18-0563.1.

Tobias Bischoff and Tapio Schneider. Energetic constraints on the position of the intertropical convergence zone. *J. Clim.*, 27(13):4937–4951, July 2014. ISSN 0894-8755, 1520-0442. doi:10.1175/JCLI-D-13-00650.1.

J Bjerknes. Atlantic Air-Sea interaction. *Adv. Geophys.*, 10:1–82, January 1964. ISSN 0065-2687. doi:10.1016/S0065-2687(08)60005-9.

Peter Brimblecombe. The clean air act after 50 years. *Weather*, 61(11):311–314, November 2006. ISSN 0043-1656, 1477-8696. doi:10.1256/wea.127.06.

W S Broecker. Thermohaline circulation, the achilles heel of our climate system: will man-made CO2 upset the current balance? *Science*, 278(5343):1582–1588, November 1997. ISSN 0036-8075, 1095-9203. doi:10.1126/science.278.5343.1582.

Wallace S Broecker. Unpleasant surprises in the greenhouse? `http://dx.doi.org/10.1038/328123a0`, July 1987. Accessed: 2023-7-27.

Victor Brovkin, Edward Brook, John W Williams, Sebastian Bathiany, Timothy M Lenton, Michael Barton, Robert M DeConto, Jonathan F Donges, Andrey Ganopolski, Jerry McManus, Summer Praetorius, Anne de Vernal, Ayako Abe-Ouchi, Hai Cheng, Martin Claussen, Michel Crucifix, Gilberto Gallopín, Virginia Iglesias, Darrell S Kaufman, Thomas Kleinen, Fabrice Lambert, Sander van der Leeuw, Hannah Liddy, Marie-France Loutre, David McGee, Kira Rehfeld, Rachael Rhodes, Alistair W R Seddon, Martin H Trauth, Lilian Vanderveken, and Zicheng Yu. Past abrupt changes, tipping points and cascading impacts in the earth system. *Nat. Geosci.*, 14(8):550–558, July 2021. ISSN 1752-0894. doi:10.1038/s41561-021-00790-5.

John C H Chiang and Cecilia M Bitz. Influence of high latitude ice cover on the marine intertropical convergence zone. *Clim. Dyn.*, 25(5):477–496, October 2005. ISSN 0930-7575, 1432-0894. doi:10.1007/s00382-005-0040-5.

Joseph P Clark, Steven B Feldstein, and Sukyoung Lee. Moist static energy transport trends in four global reanalyses: Are they downgradient? *Geophys. Res. Lett.*, 49(20), October 2022. ISSN 0094-8276, 1944-8007. doi:10.1029/2022gl098822.

Tyler Cox, Aaron Donohoe, Gerard H Roe, Kyle C Armour, and Dargan M W Frierson. Near invariance of poleward atmospheric heat transport in response to midlatitude orography. *J. Clim.*, 35(13):4099–4113, July 2022. ISSN 0894-8755, 1520-0442. doi:10.1175/JCLI-D-21-0888.1.

Tyler Cox, Aaron Donohoe, Kyle C Armour, Dargan M W Frierson, and Gerard H Roe. Comment on "moist static energy transport trends in four global reanalyses: Are they downgradient?" by clark et al. (2022). *Geophys. Res. Lett.*, 50(15), August 2023. ISSN 0094-8276, 1944-8007. doi:10.1029/2023gl102804.

Clara Deser, Adam S Phillips, Isla R Simpson, Nan Rosenbloom, Dani Coleman, Flavio Lehner, Angeline G Pendergrass, Pedro DiNezio, and Samantha Stevenson. Isolating the evolving contributions of anthropogenic aerosols and greenhouse gases: A new CESM1 large ensemble community resource. *J. Clim.*, 33(18):7835–7858, September 2020. ISSN 0894-8755, 1520-0442. doi:10.1175/JCLI-D-20-0123.1.

Aaron Donohoe and Aiko Voigt. Why future shifts in tropical precipitation will likely be small: The location of the tropical rain belt and the hemispheric contrast of energy input to the atmosphere. In S-Y Simon Wang, Jin-Ho Yoon, Christopher C Funk, and Robert R Gillies, editors, *Climate Extremes*, volume 6 of *Geophysical Monograph Series*, pages 115–137. John Wiley & Sons, Inc., Hoboken, NJ, USA, June 2017. ISBN 9781119068020, 9781119067849. doi:10.1002/9781119068020.ch8.

Aaron Donohoe, John Marshall, David Ferreira, and David Mcgee. The relationship between ITCZ location and Cross-Equatorial atmospheric heat transport: From the seasonal cycle to the last glacial maximum. *J. Clim.*, 26(11):3597–3618, June 2013. ISSN 0894-8755, 1520-0442. doi:10.1175/JCLI-D-12-00467.1.

Aaron Donohoe, Kyle C Armour, Gerard H Roe, David S Battisti, and Lily Hahn. The partitioning of meridional heat transport from the last glacial maximum to CO2 quadrupling in coupled climate models. *J. Clim.*, 33(10):4141–4165, April 2020. ISSN 0894-8755, 1520-0442. doi:10.1175/JCLI-D-19-0797.1.

Daniel Enderton and John Marshall. Explorations of Atmosphere–Ocean–Ice climates on an aquaplanet and their meridional energy transports. *J. Atmos. Sci.*, 66(6):1593–1611, June 2009. ISSN 0022-4928, 1520-0469. doi:10.1175/2008JAS2680.1.

Mark R England, Ian Eisenman, Nicholas J Lutsko, and Till J W Wagner. The recent emergence of arctic amplification. *Geophys. Res. Lett.*, 48(15):e2021GL094086, August 2021. ISSN 0094-8276. doi:10.1029/2021GL094086.

David Fowler, Peter Brimblecombe, John Burrows, Mathew R Heal, Peringe Grennfelt, David S Stevenson, Alan Jowett, Eiko Nemitz, Mhairi Coyle, Xuejun Lui, Yunhua Chang, Gary W Fuller, Mark A Sutton, Zbigniew Klimont, Mike H Unsworth, and Massimo Vieno. A chronology of

global air quality. *Philos. Trans. A Math. Phys. Eng. Sci.*, 378(2183):20190314, October 2020. ISSN 1364-503X, 1471-2962. doi:10.1098/rsta.2019.0314.

S K Gulev, P W Thorne, J Ahn, F J Dentener, C M Domingues, S Gerland, D Gong, D S Kaufman, H C Nnamchi, J Quaas, J A Rivera, S Sathyendranath, S L Smith, B Trewin, K von Shuckmann, and R S Vose. Changing state of the climate system. In V Masson-Delmotte, P Zhai, A Pirani, S L Connors, C Péan, S Berger, N Caud, Y Chen, L Goldfarb, M I Gomis, M Huang, K Leitzell, E Lonnoy, J B R Matthews, T K Maycock, T Waterfield, O Yelekçi, R Yu, and B Zhou, editors, *Climate Change 2021: The Physical Science Basis. Contribution of Working Group I to the Sixth Assessment Report of the Intergovernmental Panel on Climate Change*, chapter 2. Cambridge University Press, Cambridge, United Kingdom and New York, NY, USA, 2021.

Dennis L Hartmann. *Global Physical Climatology*. Elsevier, 2016. ISBN 9780123285317.

Øivind Hodnebrog, Gunnar Myhre, Caroline Jouan, Timothy Andrews, Piers M Forster, Hailing Jia, Norman G Loeb, Dirk J L Olivié, David Paynter, Johannes Quaas, Shiv Priyam Raghuraman, and Michael Schulz. Recent reductions in aerosol emissions have increased earth's energy imbalance. *Communications Earth & Environment*, 5(1):1–9, April 2024. ISSN 2662-4435, 2662-4435. doi:10.1038/s43247-024-01324-8.

Rachel M Hoesly, Steven J Smith, Leyang Feng, Zbigniew Klimont, Greet Janssens-Maenhout, Tyler Pitkanen, Jonathan J Seibert, Linh Vu, Robert J Andres, Ryan M Bolt, Tami C Bond, Laura Dawidowski, Nazar Kholod, June-Ichi Kurokawa, Meng Li, Liang Liu, Zifeng Lu, Maria Cecilia P Moura, Patrick R O'Rourke, and Qiang Zhang. Historical (1750–2014) anthropogenic emissions of reactive gases and aerosols from the community emissions data system (CEDS). *Geosci. Model Dev.*, 11(1):369–408, January 2018. ISSN 1991-959X, 1991-9603. doi:10.5194/gmd-11-369-2018.

Yen-Ting Hwang and Dargan M W Frierson. Increasing atmospheric poleward energy transport with global warming. *Geophys. Res. Lett.*, 37(24), December 2010. ISSN 0094-8276, 1944-8007. doi:10.1029/2010gl045440.

D B Irving, S Wijffels, and J A Church. Anthropogenic aerosols, greenhouse gases, and the uptake, transport, and storage of excess heat in the climate system. *Geophys. Res. Lett.*, 46(9): 4894–4903, May 2019. ISSN 0094-8276, 1944-8007. doi:10.1029/2019gl082015.

M-A Knietzsch, A Schröder, V Lucarini, and F Lunkeit. The impact of oceanic heat transport on the atmospheric circulation. *Earth Syst. Dyn.*, 6(2):591–615, September 2015. ISSN 2190-4979, 2190-4987. doi:10.5194/esd-6-591-2015.

Valerio Lembo, Doris Folini, Martin Wild, and Piero Lionello. Inter-hemispheric differences in energy budgets and cross-equatorial transport anomalies during the 20th century. *Clim. Dyn.*, 53(1):115–135, July 2019. ISSN 0930-7575, 1432-0894. doi:10.1007/s00382-018-4572-x.

Timothy M Lenton, Hermann Held, Elmar Kriegler, Jim W Hall, Wolfgang Lucht, Stefan Rahmstorf, and Hans Joachim Schellnhuber. Tipping elements in the earth's climate system. *Proc. Natl. Acad. Sci. U. S. A.*, 105(6):1786–1793, February 2008. ISSN 0027-8424, 1091-6490. doi:10.1073/pnas.0705414105.

Timothy M Lenton, Johan Rockström, Owen Gaffney, Stefan Rahmstorf, Katherine Richardson, Will Steffen, and Hans Joachim Schellnhuber. Climate tipping points - too risky to bet against. *Nature*, 575(7784):592–595, November 2019. ISSN 0028-0836, 1476-4687. doi:10.1038/d41586-019-03595-0.

NOAA Physical Sciences Laboratory. ENSO information. `https://psl.noaa.gov/enso/`, n.d. Accessed: 2024-8-6.

Abraham H Oort. The observed annual cycle in the meridional transport of atmospheric energy. *J. Atmos. Sci.*, 28(3):325–339, April 1971. ISSN 0022-4928. doi:10.1175/1520-0469(1971)028<0325:TOACIT>2.0.CO;2.

Abraham H Oort and Thomas H Vonder Haar. On the observed annual cycle in the Ocean-Atmosphere heat balance over the northern hemisphere. *J. Phys. Oceanogr.*, 6(6):781–800, November 1976. ISSN 0022-3670, 1520-0485. doi:10.1175/1520-0485(1976)006<0781:OTOACI>2.0.CO;2.

F A Pearce and A Bodas-Salcedo. Implied heat transport from CERES data: Direct radiative effect of clouds on regional patterns and hemispheric symmetry. *J. Clim.*, 36(12):4019–4030, May 2023. ISSN 0894-8755, 1520-0442. doi:10.1175/JCLI-D-22-0149.1.

G Persad, B H Samset, L J Wilcox, Robert J Allen, Massimo A Bollasina, Ben B B Booth, Céline Bonfils, Tom Crocker, Manoj Joshi, Marianne T Lund, Kate Marvel, Joonas Merikanto, Kalle Nordling, Sabine Undorf, Detlef P van Vuuren, Daniel M Westervelt, and Alcide Zhao. Rapidly evolving aerosol emissions are a dangerous omission from near-term climate risk assessments. *Environ. Res.: Climate*, 2(3):032001, June 2023. ISSN 2752-5295. doi:10.1088/2752-5295/acd6af.

G G Persad. The dependence of aerosols' global and local precipitation impacts on the emitting region. *Atmos. Chem. Phys.*, 23(6):3435–3452, 2023. doi:10.5194/acp-23-3435-2023.

Geeta G Persad and Ken Caldeira. Divergent global-scale temperature effects from identical aerosols emitted in different regions. *Nat. Commun.*, 9(1):3289, August 2018. ISSN 2041-1723. doi:10.1038/s41467-018-05838-6.

Grant W Petty. *A First Course in Atmospheric Radiation*. Sundog Publishing, Madison, WI, 2006. ISBN 9780972903318.

Raymond T Pierrehumbert. The hydrologic cycle in deep-time climate problems. *Nature*, 419 (6903):191–198, September 2002. ISSN 0028-0836. doi:10.1038/nature01088.

Stefan Rahmstorf. Ocean circulation and climate during the past 120,000 years. *Nature*, 419 (6903):207–214, September 2002. ISSN 0028-0836. doi:10.1038/nature01090.

Stefan Rahmstorf. Thermohaline circulation: The current climate. `http://dx.doi.org/10.1038/421699a`, February 2003. Accessed: 2023-7-27.

Brian E J Rose and David Ferreira. Ocean heat transport and water vapor greenhouse in a warm equable climate: A new look at the low gradient paradox. *J. Clim.*, 26(6):2117–2136, March 2012. ISSN 0894-8755, 1520-0442. doi:10.1175/JCLI-D-11-00547.1.

Tapio Schneider, Tobias Bischoff, and Gerald H Haug. Migrations and dynamics of the intertropical convergence zone. *Nature*, 513(7516):45–53, September 2014. ISSN 0028-0836, 1476-4687. doi:10.1038/nature13636.

Tiffany A Shaw and Zoë Smith. The midlatitude response to polar sea ice loss: Idealized Slab-Ocean aquaplanet experiments with thermodynamic sea ice. *J. Clim.*, 35(8):2633–2649, April 2022. ISSN 0894-8755, 1520-0442. doi:10.1175/JCLI-D-21-0508.1.

Drew Shindell, Michael Schulz, Yi Ming, Toshihiko Takemura, Greg Faluvegi, and V Ramaswamy. Spatial scales of climate response to inhomogeneous radiative forcing. *J. Geophys. Res.*, 115(D19), October 2010. ISSN 0148-0227, 2156-2202. doi:10.1029/2010jd014108.

Peter H Stone. Constraints on dynamical transports of energy on a spherical planet. *Dyn. Atmos. Oceans*, 2(2):123–139, May 1978. ISSN 0377-0265. doi:10.1016/0377-0265(78)90006-4.

Kevin E Trenberth. Mean annual poleward energy transports by the oceans in the southern hemisphere. *Dyn. Atmos. Oceans*, 4(1):57–64, August 1979. ISSN 0377-0265. doi:10.1016/0377-0265(79)90052-6.

Kevin E Trenberth and Julie M Caron. Estimates of meridional atmosphere and ocean heat transports. *J. Clim.*, 14(16):3433–3443, August 2001. ISSN 0894-8755. doi:10.1175/1520-0442(2001)014<3433:EOMAAO>2.0.CO;2.

Kevin E Trenberth and David P Stepaniak. Seamless poleward atmospheric energy transports and implications for the hadley circulation. *J. Clim.*, 16(22):3706–3722, November 2003a. ISSN 0894-8755, 1520-0442. doi:10.1175/1520-0442(2003)016<3706:spaeta>2.0.co;2.

Kevin E Trenberth and David P Stepaniak. Covariability of components of poleward atmospheric energy transports on seasonal and interannual timescales. *J. Clim.*, 16 (22):3691–3705, November 2003b. ISSN 0894-8755, 1520-0442. doi:10.1175/1520-0442(2003)016<3691:cocopa>2.0.co;2.

S Twomey. The influence of pollution on the shortwave albedo of clouds. *J. Atmos. Sci.*, 34(7):1149–1152, July 1977. ISSN 0022-4928, 1520-0469. doi:10.1175/1520-0469(1977)034<1149:TIOPOT>2.0.CO;2.

Thomas H Vonder Haar and Abraham H Oort. New estimate of annual poleward energy transport by northern hemisphere oceans. *J. Phys. Oceanogr.*, 3(2):169–172, April 1973. ISSN 0022-3670. doi:10.1175/1520-0485(1973)003<0169:NEOAPE>2.0.CO;2.

Chenggong Wang, Brian J Soden, Wenchang Yang, and Gabriel A Vecchi. Compensation between cloud feedback and aerosol-cloud interaction in CMIP6 models. *Geophys. Res. Lett.*, 48 (4), February 2021. ISSN 0094-8276, 1944-8007. doi:10.1029/2020gl091024.

Carl Wunsch. The total meridional heat flux and its oceanic and atmospheric partition. *J. Clim.*, 18(21):4374–4380, November 2005. ISSN 0894-8755, 1520-0442. doi:10.1175/JCLI3539.1.

Seiji Yukimoto, Naga Oshima, Hideaki Kawai, Makoto Deushi, and Takuro Aizawa. Role of interhemispheric heat transport and global atmospheric cooling in multidecadal trends of northern hemisphere precipitation. *Geophys. Res. Lett.*, 49(18), September 2022. ISSN 0094-8276, 1944-8007. doi:10.1029/2022gl100335.

Mark D Zelinka, Timothy A Myers, Daniel T McCoy, Stephen Po-Chedley, Peter M Caldwell, Paulo Ceppi, Stephen A Klein, and Karl E Taylor. Causes of higher climate sensitivity in CMIP6 models. *Geophys. Res. Lett.*, 47(1):1029, January 2020. ISSN 0094-8276, 1944-8007. doi:10.1029/2019GL085782.

Chapter 3

Anomalous Northward Energy Transport due to Anthropogenic Aerosols During the 20th Century

This chapter is an exact republication of the text and figures (with the exception of section numbering, which has been modified to align with the larger numbering of this dissertation) from the article of the same name (Needham and Randall, 2023) originally published in the *Journal of Climate* in July, 2023, under the DOI: **https://doi.org/10.1175/JCLI-D-22-0798.1**

Overview

In the tropics, the absorbed solar radiation is larger than the outgoing longwave radiation, while the opposite is true at high latitudes. This basic fact implies a poleward energy transport (PET) in both hemispheres, which is accomplished by the atmosphere and oceans. The magnitude of PET is determined by the top of atmosphere gradient in the net radiation flux, and small changes to this quantity must change the total PET in the absence of changes in heat uptake. We analyze a large ensemble of 50 historic climate simulations from the CESM LENS2 project and find a significant PET anomaly in the latter half of the twentieth century. The temporal evolution of this anomaly - with a rapid increase after 1950, a peak near 1975, and a rapid decrease in the 1990s - mirrors the historic trend of sulphur dioxide (SO_2, a significant aerosol predecessor) emissions from Europe and North America. This anomaly also appears in an analysis of

the PET calculated from ERA5 reanalyses and from the CESM2 Single Forcing Large Ensemble. Consistent with previous studies, we find that historic SO_2 emissions from Europe and North America brightened clouds which reflected additional solar radiation back to space in the mid-latitudes: this shortwave anomaly increased the meridional gradient in the net TOA radiation flux, and induced an anomalous northward energy transport. Finally, our results suggest that cryosphere processes become an additional important factor in setting the PET anomaly during the first years of the twenty-first century by contributing to the difference in absorbed solar radiation between hemispheres alongside cloud radiative effects.

Significance Statement

In this study, we analyze a large group of climate model simulations from 1850 to 2014 and find that this historical pollution changed the way that heat was transported from the tropics to the Earth's poles. We also find this change in heat transport when we analyzed an atmospheric reanalysis, which is a historical dataset that combines many meteorological observations into a best estimate of the past climate state. This extra reflection of sunlight from polluted clouds cooled the northern hemisphere, and we hypothesize that this cooling caused more heat transport out of the tropics. Lastly, we find that similar pollution emitted from China and India in more recent decades has not led to a change in the earth's heat transport because of counteracting changes in snow and ice in the northern hemisphere.

3.1 Introduction

Poleward energy transport (PET) is the necessary result of the meridional gradient in the TOA radiation flux between the tropics and the poles, and has been well understood for decades (Sverdrup, 1942; Riehl and Malkus, 1958; Bjerknes, 1964; Oort, 1971; Vonder Haar and Oort, 1973; Trenberth, 1979). This PET is almost entirely accomplished through atmospheric and oceanic transports (Held, 2001; Trenberth and Stepaniak, 2004), with only a small residual occurring via other geophysical processes such as river and groundwater flows and iceberg trans-

ports. Stone (1978) showed that for an arbitrary spherical planet, the total poleward energy transport is determined by orbital parameters (i.e, axial tilt, eccentricity, and obliquity), the OLR, and the planetary albedo. This then implies that the total PET is largely insensitive to the specifics of atmospheric and oceanic dynamics inasmuch as they do not alter the meridional albedo gradient through changes in, for example, cloud properties or polar ice. Recent work has supported this interpretation, with several studies examining the role of polar ice in determining the total PET through changes in the albedo (Enderton and Marshall, 2009; Rose and Ferreira, 2012; Knietzsch et al., 2015; Shaw and Smith, 2022). While it may seem an abstract concept, the PET is tied to many aspects of weather and climate, from the Arctic amplification of global warming (Hwang et al., 2011; Serreze and Barry, 2011; Screen et al., 2012; Huang et al., 2017; Previdi et al., 2021; Pithan and Jung, 2021) to the position of the Intertropical Convergence Zone (ITCZ; Chiang and Bitz, 2005; Kang et al., 2008; Marshall et al., 2013; Hwang et al., 2013; Frierson et al., 2013; Schneider et al., 2014; Adam et al., 2016; Donohoe and Voigt, 2017; Kang, 2020; Yukimoto et al., 2022).

An obvious question to consider is how the PET (and its constituent transports in the atmosphere and ocean) may respond to various climate forcings. For example, under greenhouse gas forcing the atmospheric energy transport is expected to increase due to increased latent energy transport by baroclinic eddies in a warmer atmosphere that holds more moisture (Held and Soden, 2006; Hwang and Frierson, 2010). Conversely, greenhouse warming may lead to a reduction in ocean energy transport due to a slowdown in the Atlantic Meridional Overturning Circulation (Rahmstorf et al., 2015; Caesar et al., 2018, 2021) in response to increased freshwater runoff into the north Atlantic from Greenland.

Anthropogenic aerosols also represent a major climate forcing with the same approximate global mean magnitude as, and opposite sign of, greenhouse gases (Fig. 2.10 from Gulev et al., 2021). However, aerosols typically have a much shorter lifetime than greenhouse gases, and thus are not well-mixed in the atmosphere. In practice, this means that the radiative impact of

aerosols can be extremely heterogeneous in space, and the resulting climate impact is sensitive to the location of emission (Shindell et al., 2010; Persad and Caldeira, 2018).

The historic trend in anthropogenic aerosol concentrations is of primary relevance to this study, which we investigate through the related trend sulphur dioxide (SO_2) emissions. While there are natural sources (especially volcanoes; Gulev et al., 2021), SO_2 is major pollutant, with a large fraction of emissions from the energy extraction and industrial sectors of the economy (Hoesly et al., 2018). In the atmosphere, SO_2 is oxidized to sulphuric acid (H_2SO_4), a major contributor to acid rain (Grennfelt et al., 2020). In the presence of ammonia (NH_3) or other alkaline agents, H_2SO_4 is neutralized to form sulphate aerosol (Larssen et al., 2006); sulphate aerosols impact the climate directly by scattering radiation, and indirectly through changes in clouds and precipitation (Twomey, 1977; Albrecht, 1989; Rosenfeld et al., 2014; Hoesly et al., 2018; Naik et al., 2021).

The Community Emissions Data System (CEDS; Hoesly et al., 2018), used as one of the forcing agents for the Coupled Model Intercomparison Project, Phase 6 (CMIP6; Eyring et al., 2016), records our current best estimate of the trend in SO_2 emissions from 1750 to the near-present. SO_2 emissions increased rapidly in the decades following the Second World War, mirroring the trend exhibited by all pollutants. However, in contrast to pollutants like CO_2, SO_2 emissions began to decline in Europe and North America in the last quarter of the twentieth century due to emission control policies. As emissions declined in Europe and North America, the primary source region shifted to Asia (see Figs. 2 and 3 of Hoesly et al., 2018), which is presently responsible for around half of annual SO_2 emissions. Recent studies have suggested that this increase and then decline in sulphate emissions from the industrialized West has enhanced the cooling during the mid-20th century and the recently observed amplification of warming in the Arctic (Acosta Navarro et al., 2016; Deser et al., 2020; England et al., 2021; Aizawa et al., 2022).

Hwang et al. (2013) found that historic sulphate aerosols shifted the ITCZ southward in the late 20th century. They proposed a mechanism whereby aerosol direct and indirect effects decrease local solar absorption in the northern midlatitudes, which induces an anomalous Hadley

circulation. The upper branch transports anomalous dry static energy (DSE, the combination of potential energy and enthalpy) from the southern to the northern hemisphere. Conversely, the lower branch then transports anomalous latent energy (LE) southward, leading to the southward precipitation shift they observed in gridded observations, a reanalysis product, and in the ensemble mean of a subset of CMIP3/5 models. Similar changes in cross-equatorial transport in response to aerosols were found in the context of CMIP5 historical simulations performed with all forcings, greenhouse gas-only forcing, and anthropogenic aerosol-only forcing (Allen et al., 2015; Irving et al., 2019; Lembo et al., 2019). Consistent with these results, Yukimoto et al. (2022) found that precipitation trends in the northern hemisphere were largely driven by changes in cross-equatorial heat transport associated with an anomalous Hadley circulation in historical simulations performed with the latest version of the Meteorological Research Institute Earth System Model (MRI-ESM2.0), and suggested that aerosol forcing may be the primary driver of hemispheric precipitation trends due to the impact on solar radiation.

In this study, we analyze the trends in poleward energy transport at all latitudes in a large ensemble of historical climate simulations. We find a significant northward anomaly in the total atmospheric plus oceanic transport from about 10°S-40°N which peaks in approximately 1975. This anomaly occurs in each member of a large ensemble of historical climate simulations (Rodgers et al., 2021) performed with the Community Earth System Model, version 2 (Danabasoglu et al., 2020). Further investigation of a set of single-forcing simulations (Simpson et al., 2022) leads us to attribute this anomaly to historical emissions of SO_2 from Europe and North America which altered the meridional radiation gradient at the TOA through changes in the shortwave cloud radiative effect in the midlatitudes. We also find that the PET is much less sensitive to twenty-first century SO_2 emissions from Asia, likely due to the increasing importance of cryosphere processes.

3.2 Methods

3.2.1 Data

Analysis is primarily performed on output from the CESM2 Large Ensemble (hereafter CESM2-LE, Rodgers et al., 2021). The CESM2-LE is a 100-member large ensemble which covers the period from 1850-2100 forced by the CMIP6 (Eyring et al., 2016) historical and SSP3-7.0 protocols. Fifty simulations from the large ensemble utilize the biomass burning (BMB) forcing from the CMIP6 protocol, which incorporates satellite observations of wildfires from 1997-2014, while the remaining fifty simulations utilize a smoothed BMB forcing designed to remove the abrupt change in interannual variability and nearly conserve total emissions (Rodgers et al., 2021; Fasullo et al., 2022). We have repeated our analysis for each of these two fifty-member sub-ensembles and found qualitatively similar results (not shown). The simulations with the smoothed BMB forcing had a slightly larger PET anomaly at certain latitudes in the northern hemisphere, but this difference was not found to be statistically significant during most years at most latitudes.

Our analysis is limited to the historical period (1850-2014), and we independently analyzed each of the 50 ensemble members which were forced by the smoothed BMB forcing prior to calculating ensemble-mean statistics. The CESM2-LE energy and moisture budgets were calculated from monthly mean radiation fields at the TOA and surface, and from monthly mean heat flux and precipitation fields at the surface. These budgets were then used to calculate the atmospheric heat transport (AHT) using a polar cap integration method, described in the following section. The AHT was then added to the oceanic heat transport (OHT, directly output by the ocean model on monthly timescales and averaged to annual means) to give the total PET.

In addition to the CESM2-LE, we also analyze the CESM2 Single Forcing Large Ensemble (hereafter CESM2-SF Simpson et al., 2022). The CESM2-SF uses an "only" approach in which each ensemble member is forced by one time-evolving forcing while all other forcings are held at 1850 levels. CESM2-SF includes four 15-member sub-ensembles: (1) greenhouse gases (GHG); (2) anthropogenic aerosols (AAER); (3), biomass burning (BMB, which uses the smoothed forc-

ing described previously); and (4) "everything else" (EE). From the CESM2-SF, we are primarily interested in the AAER sub-ensemble in which only the "anthropogenic aerosol" forcing evolves in time, but analysis of the other sub-ensembles is included for completeness. Again, our analysis is limited to the years 1850-2014.

Lastly, we also calculate the PET from the ERA5 atmospheric reanalysis (Hersbach et al., 2020). The ERA5 PET is then compared to the PET from the CESM2-LE and both show the same first-order behavior over their common time period of 1959-2014, although we find that the ERA5 trend is smaller in magnitude.

3.2.2 Poleward Energy Transport

Neglecting marginal transports (e.g., rivers, groundwater flows, and icebergs), the poleward energy transport across an arbitrary latitude φ_0 can be calculated as the sum of AHT and OHT at that latitude.

The AHT can be calculated from a dynamic or an energetic perspective (Armour et al., 2019; Donohoe et al., 2020; Cox et al., 2022). In the dynamic perspective, the energy transports associated with fluid motions are integrated zonally and vertically throughout the depth of the atmosphere; from the energetic perspective the AHT is constrained by the fluxes of heat and radiation into the atmosphere at the TOA and the surface. The dynamic method allows for the decomposition of AHT into contributions from the mean meridional circulation and from eddies, but requires a much larger volume of data (e.g., 3D fields of temperature, humidity and wind). For this study we calcualte AHT from the energetic perspective to more easily analyze the heat transport in these large ensembles of climate simulations. Future work will utilize the dynamic perspective to investigate how historic forcing alters the heat transport associated with the mean and eddy components of the atmospheric circulation.

From the energetic perspective, the AHT can be calculated (e.g., Trenberth and Stepaniak, 2003) by integrating the zonal mean time mean difference between the net radiative flux at the TOA and the energy flux at the surface (i.e., the net sensible and latent heat flux from the land

surface and ocean to the atmosphere, combined with the net radiative flux), from the south pole to φ_0:

$$\overline{AHT}^t(\varphi_0) = 2\pi a^2 \int_{-\pi/2}^{\varphi_0} \overline{F_T - F_S}^{t,\lambda} \cos\varphi' \mathrm{d}\varphi', \tag{3.1}$$

with the boundary condition

$$\overline{AHT}^t(-\pi/2) = \overline{AHT}^t(\pi/2) = 0. \tag{3.2}$$

In Eq. 3.1, $\overline{\chi}^t$ denotes the time mean of a quantity χ, and $\overline{\chi}^{t,\lambda}$ denotes the zonal mean of the time mean of χ. F_T and F_S denote the net flux at the TOA and surface, respectively. The boundary condition at $\varphi = \pi/2$ is enforced by applying a uniform correction to the integrand to ensure that its global mean is zero.

Equation 3.1 is essentially an application of the divergence theorem. Under the assumption of no long-term heat uptake, which is valid for the atmosphere on timescales of a year or longer, the (vertical) convergence of energy from the TOA and surface into a "spherical cap" region defined by the limits of integration in Eq. 3.1 must be balanced by the (horizontal) divergence of energy from the cap. This represents the flux of energy across φ_0. A similar calculation yields the atmospheric LE transport if $\overline{F}^{t,\lambda}$ is replaced with difference between evaporation and precipitation, in energy units. Then, the total atmospheric transport minus LE transport gives the atmospheric DSE transport.

The assumption of no long-term heat uptake on yearly timescales *does not hold* for the ocean in the way that it does for the atmosphere. Then, a polar cap integration like Eq. 3.1 using $\overline{F_S}^{t,\lambda}$ would conflate oceanic heat transport and oceanic heat uptake. To avoid this, oceanic heat transport was not calculated from surface fluxes, but was instead taken directly from CESM2 ocean model monthly mean output (model field "N_HEAT"), interpolated onto the coarser atmospheric model grid, and then averaged to annual means. The total poleward energy transport was then calculated as the sum of the AHT and OHT.

In practice, there is not a large difference between the PET calculated using the method described above, and a more simple method of integrating the TOA energy balance, even though there has been a large amount of ocean heat uptake over the historical period (e.g., Huguenin et al., 2022). However these two methods do give noticeably different results when applied to the CESM2-LE simulations under the SSP3-7.0 future forcing scenario (i.e., simulated years 2015-2100, not shown).

3.3 Results

3.3.1 Climatology of PET in CESM2-LE

Figure 3.1 shows the total poleward energy transport (black), the transport by the atmosphere and oceans (red and blue solid lines, respectively), and the atmospheric transport of latent energy and dry static energy (cyan and orange dashed lines for LE and DSE, respectively) from the CESM2-LE for the period from 1851-1900. The shading represents the 5th to 95th percentile among ensemble members, as a measure of ensemble spread.

Figure 3.1 is consistent with previous studies of PET in the earth system (e.g., Trenberth and Caron, 2001; Yang et al., 2015). The total PET is a smooth, almost sinusoidal curve showing the transport of energy from the tropics to the poles, with peak values of almost 6 PW near 35° in each hemisphere. The constituent transports in the atmosphere and oceans are much less smooth, and yet they combine to give a total transport which is remarkably "seamless" (Trenberth and Stepaniak, 2003) with latitude from the tropics to the extratropics. The spread in PET is clearly attributable to the spread in OHT, with very little variability evident in the AHT.

Broad characteristics of the atmospheric global circulation are evident in the curves for DSE and LE transport. In the tropics LE transport is equatorward, rather than poleward, due to the advection of moisture by the near-surface branches of the Hadley cells (Hwang et al., 2013; Yukimoto et al., 2022). This moisture convergence drives deep convection in the intertropical convergence zone (ITCZ) where energy is lifted and eventually exported poleward as DSE by the mean meridional circulation (Riehl and Malkus, 1958; Neelin and Held, 1987). Away from the

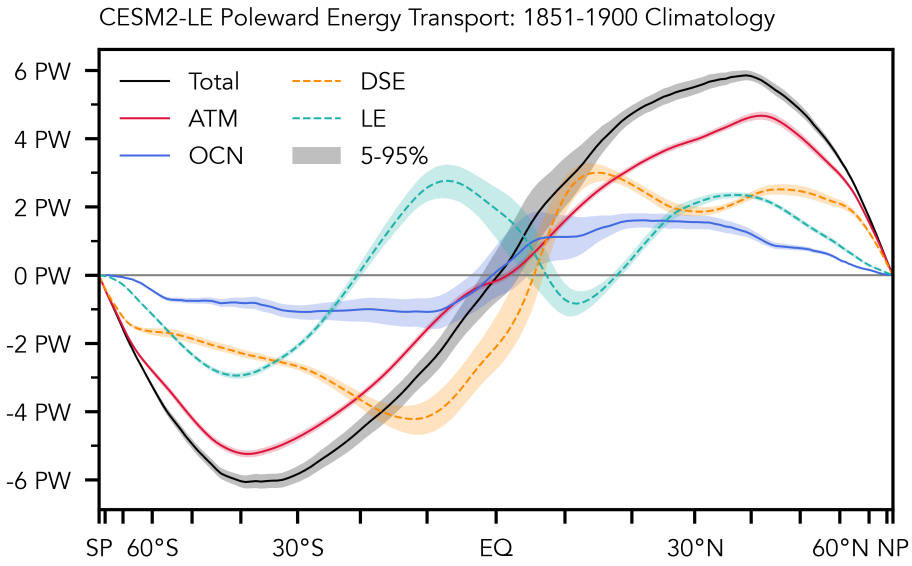

Figure 3.1: CESM2-LE 1851-1900 ensemble mean zonally integrated northward energy transport (black) decomposed into contributions from the atmosphere (red), and oceans (blue). Atmospheric transport is further decomposed into dry static energy (orange) and latent energy (cyan) transports, in dashed lines. The shading around each line represents the 5th to 95th percentile among ensemble members. Note that the horizontal axis is scaled by the sine of latitude.

equator transient and stationary eddies act to transport LE and DSE in the same direction. This eddy transport has been modeled as the simple down-gradient diffusion of energy (Hwang and Frierson, 2010; Siler et al., 2018; Armour et al., 2019; Lu et al., 2022), although a recent study by Clark et al. (2022) has suggested that the change in MSE transport does not follow the change in the MSE gradient in four global reanalyses over the last four decades.

3.3.2 Short-term variability in PET

The PET was calculated for each of the 50 CESM2-LE ensemble members with smoothed BMB for each year from 1851-2100. From this timeseries we then calculated the anomalous PET anomaly relative to the 1851-1900 ensemble mean climatology. The PET anomaly at each latitude from 1851-2014 is shown in the contours of Fig. 3.2. The contours show a combination of short-term and long-term variability; vertical "pulses" lasting a few years on top of a decadal-scale trend of increasing and then decreasing PET anomaly. The high-frequency pulses are primarily due to oceanic heat transport variability (e.g., Trenberth and Fasullo, 2017; Tren-

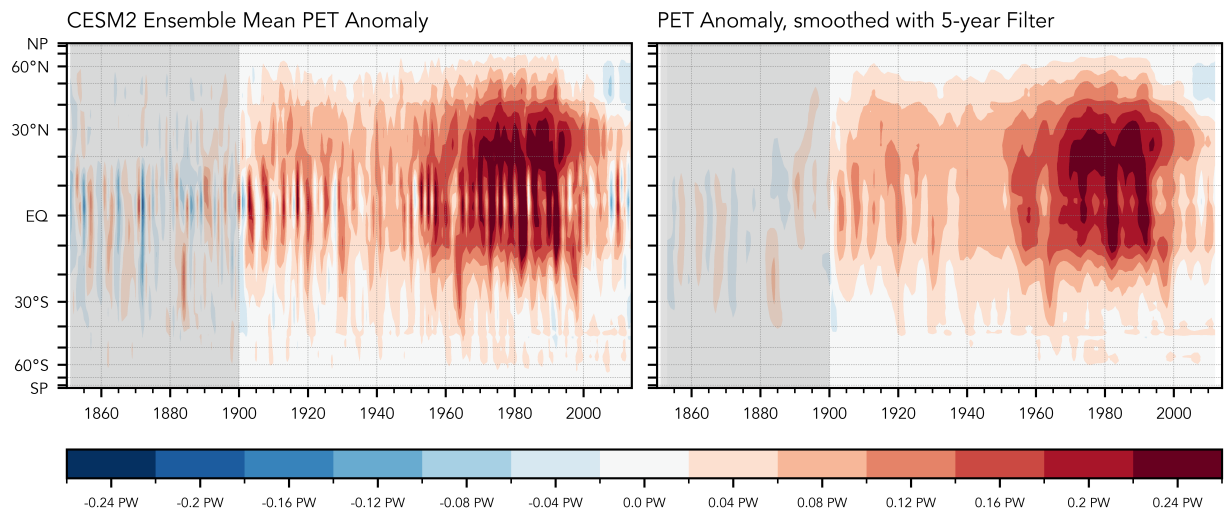

Figure 3.2: Left) Ensemble mean anomalous total energy transport calculated as the sum of atmospheric and oceanic transports relative to the baseline (1851-1900, shaded in gray). Red shading indicates anomalously northward transport. Note that the vertical axis is scaled by the sine of latitude. **Right)** same as **Left)**, but smoothed with a 5-year gaussian filter, as described in the text.

berth et al., 2019; Trenberth and Zhang, 2019). This behavior is beyond the scope of this study, so a 5-year gaussian filter with a standard deviation of 1 year has been used to smooth this and subsequent timeseries in order to focus on the decadal-scale behavior: the lower-frequency variability (i.e., the right panel of Fig. 3.2) is the subject of the remainder of this study.

3.3.3 Long-term PET trends in CESM2-LE and ERA5

Perhaps more striking than the high-frequency pulses observed in Fig. 3.2 is the decadal-scale behavior. The PET anomaly shows a positive trend at most latitudes through the course of the twentieth century which reaches its largest magnitude of approximately +0.25 PW in the roughly rectangular region bounded by 10°S-40°N and 1965-1990, consistent with the findings of Irving et al. (2019); Lembo et al. (2019).

To increase our confidence in the robustness of this trend, we calculate the PET from ERA5 atmospheric reanalyses for each full year of the ERA5 record (1959-2021). Due to the absence of an ocean model, we calculate the PET in the reanalysis following the energetic method by performing a polar cap integration on the annual mean TOA radiation fields calculated from

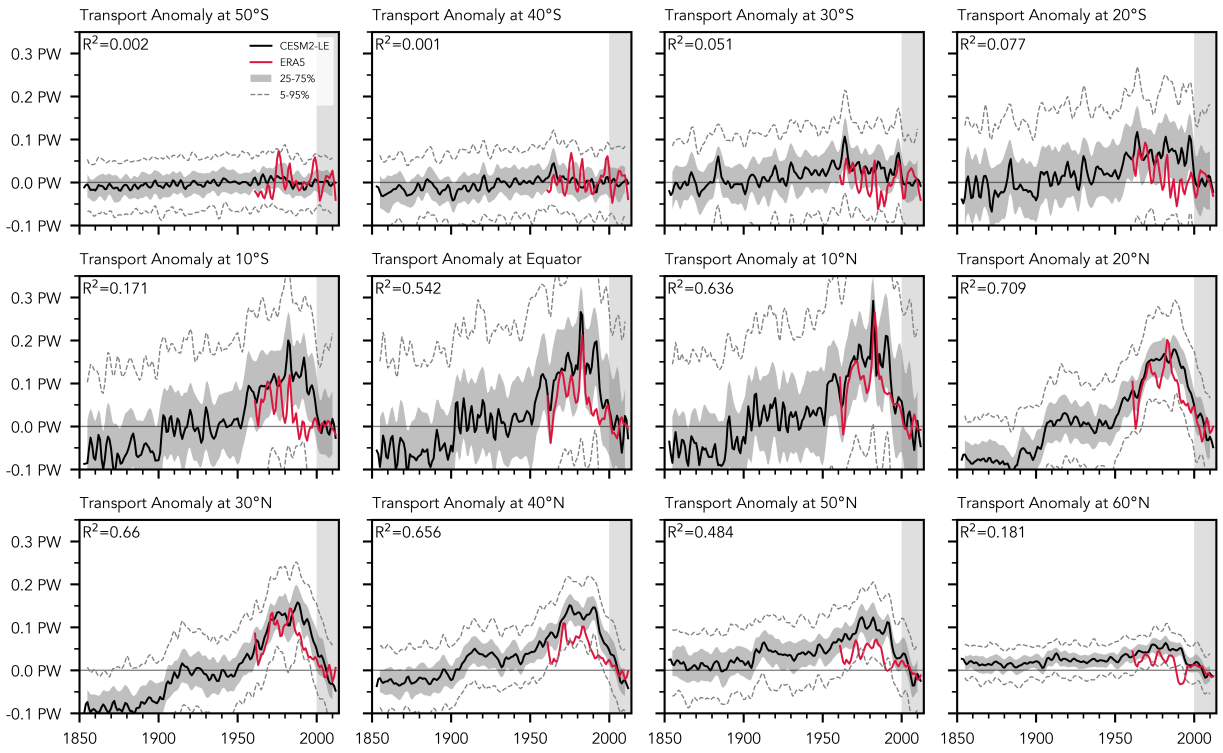

Figure 3.3: Timeseries of anomalous energy transport (positive northward) at various latitudes. The CESM2-LE ensemble mean transport is shown in black, while the ERA5 transport is shown in red. The correlation coefficient between the ensemble mean CESM2-LE and ERA5 timeseries for their common period is shown in the top-left corner of each plot. Note that anomalies in this plot are relative to 2000-2014 (shaded rectangular region).

monthly-mean reanalysis data. Anomalies were then calculated relative to a baseline, with the results shown in Fig. 3.3 alongside the CESM2-LE curves. The ERA5 data was smoothed using a 5-year gaussian filter, identical to the filter used on the CESM2-LE data. Note that for this figure the years 2000-2014 were chosen as a common baseline for CESM2-LE and ERA5.

Each panel in Fig. 3.3 shows the PET anomaly (again, relative to 2000-2014) at a particular latitude for ERA5 and CESM2-LE. The black curve shows the CESM2-LE ensemble mean. The shading around the black curve shows the 25th to 75th percentile among CESM2-LE ensemble members, and the dashed gray lines represent the 5th to 95th percentile. The red line shows the ERA5 anomaly. The correlation coefficient in the top-left corner is between the CESM2-LE ensemble mean and the ERA5 data for the common period. The primary conclusion from Fig. 3.3 is that the same PET anomaly is found in both the CESM2-LE and in ERA5. The ERA5 PET

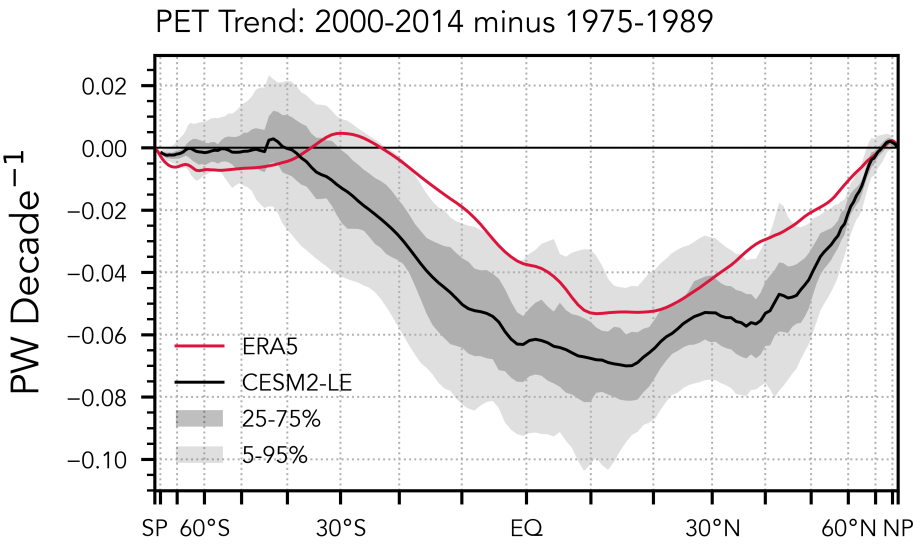

Figure 3.4: Trend in PET at each latitude for CESM2-LE (black line, shading) and ERA5 (red line). The trend is calculated as the difference of the average of 2000-2014 minus the average of 1975-1989 using the smoothed timeseries.

anomaly is of a similar magnitude, and is moderately or highly correlated with the CESM2-LE anomaly from 10°S to 60°N (R^2 greater than 0.2, and as large as 0.7), even though the ERA5 data contains variability that is smoothed out in the ensemble mean of 50 members. The fact that this anomaly is observed in both datasets also provides increased confidence in the forcings applied to the CESM2-LE and CMIP6 simulations.

The PET trend at each latitude is quantified in Fig. 3.4 for both the CESM2-LE and for ERA5. The average PET anomaly at each latitude was calculated for the two 15-year periods of 2000-2014 and 1975-1989. The difference between the two periods was then scaled by the time difference (i.e., 25 years) to give a PET trend in petawatts per decade. The shading once again represents the interquartile range or the 5th to 95th percentile among CESM2-LE ensemble members.

From Fig. 3.4, the CESM2-LE appears to overestimate the PET at most latitudes: at the latitudes of interest (approximately 10°S-40°S) the magnitude of the ERA5 trend is occasionally smaller than the 5th percentile, and almost always smaller than the 25th percentile of ensemble members. However, the two curves are broadly similar, with the largest magnitude trend

found between the equator and 20°N. The CESM2-LE trend here is about -0.07 PW per decade, while the ERA5 trend is about -0.05 PW per decade. Both curves show essentially zero trend poleward of about 70° in each hemisphere.

3.3.4 PET and SO_2 Emissions

We now turn to the underlying cause of the twentieth century PET anomaly. This anomaly occurs too early to result from anthropogenic greenhouse forcing or related effects (e.g., reduction in polar ice). Instead, our hypothesis is that this anomalous northward PET is due to anthropogenic SO_2 emissions.

To test this hypothesis we repeat our analysis using the CESM2 Single Forcing Large Ensemble (CESM2-SF). The PET was calculated for each simulation in each sub-ensemble (e.g., for each simulation with only AAER forcing, or with only GHG forcing), with timeseries plots of the PET anomaly shown in Fig. 3.5 at various latitudes alongside the original CESM2-LE timeseries. The "everything else" (EE) ensemble does not show long-term trends and has been omitted for clarity. Again, a 5-year gaussian filter was applied to smooth out high-frequency variability.

The curves for the AAER simulations (blue) shows a similar PET anomaly which peaks around 1975 that is absent in the GHG (red) or the BMB (green) curves. In the northern hemisphere (e.g., 30°N), the blue AAER curve almost exactly follows the black CESM2-SF curve. In the southern hemisphere (e.g., 30°S) the blue AAER curve is larger than the CESM2-LE curve, but is offset somewhat by the negative red GHG curve. This suggests some sort of linear cancellation in the PET response to forcing by aerosols and GHGs in the southern hemisphere which is not evident in the north.

At most latitudes and years, the curves associated with individual forcings add together to give the PET anomaly from the CESM2-LE ensemble mean (i.e., the red, blue, and green curves add together to give the black curve). The exception is from about 2000-2014 and from 20°S to 20°N. Here, the anomaly in the AER simulations (blue) remains large and positive, the anomaly in the CEMS2-LE simulations (black) decreases towards zero, and the anomaly in the GHG (red)

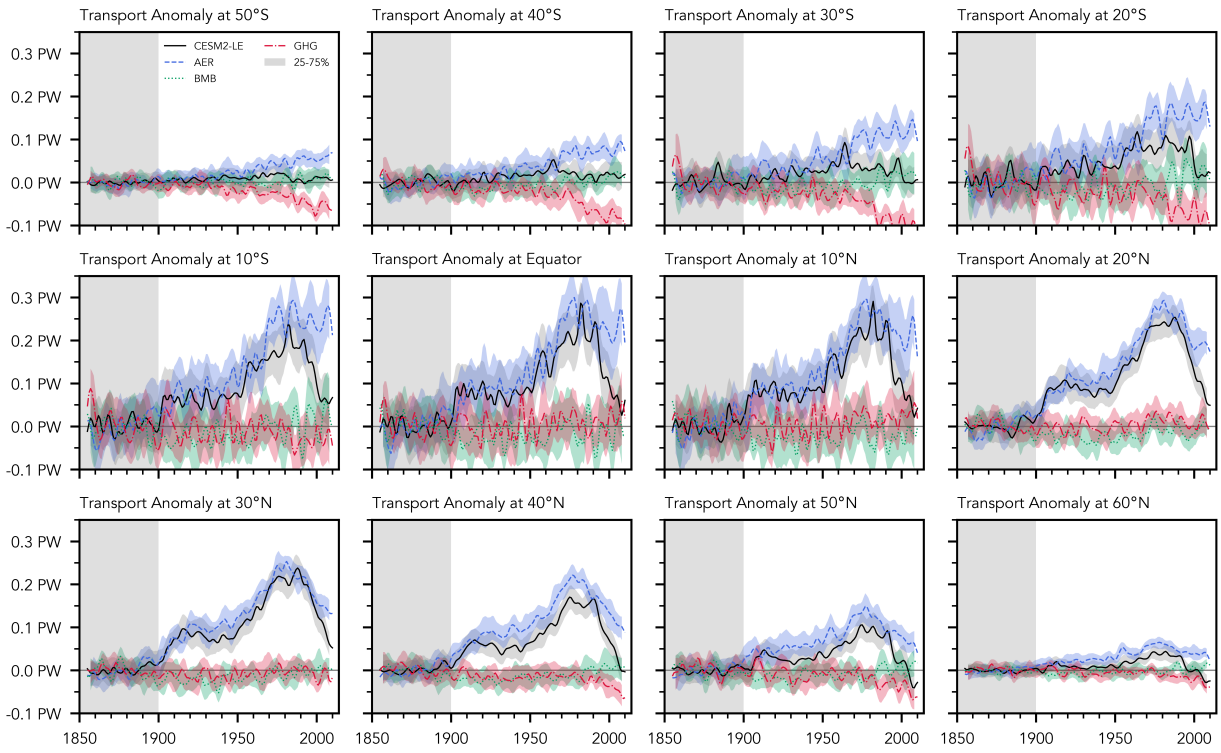

Figure 3.5: As in Fig. 3.3, but for the comparison between the CESM2-LE and the CESM2-SF using the 1851-1900 baseline (shaded gray region).

and BMB (green) simulations is negative but is too small to counteract the AER simulations. The impact of the EE simulation is negligible here (not shown). This suggests that some non-linear interaction between the various forcing agents reduces the PET anomaly in the first 15 years of the twenty-first century, which will be discussed in the conclusion section.

As further support for the anthropogenic SO_2 hypothesis, Fig. 3.6 shows the SO_2 emissions from the Community Emissions Data System (CEDS; Hoesly et al., 2018), used as one of the forcings to the CESM2-LE and CESM2-SF AAER simulations. These data provide an estimate of historical emissions and not of optical depth; however, the short lifetime of SO_2 implies a high level of correlation between SO_2 emissions and optical depth. The bottom-left panel shows a timeseries of the zonal mean SO_2 emissions from 1850 to 2014. There is a clear maximum centered around 50°N which peaks in about 1980 and decreases rapidly after about 1990. At the same time there is a secondary maximum centered around 40°N. After 1990, 40°N becomes the

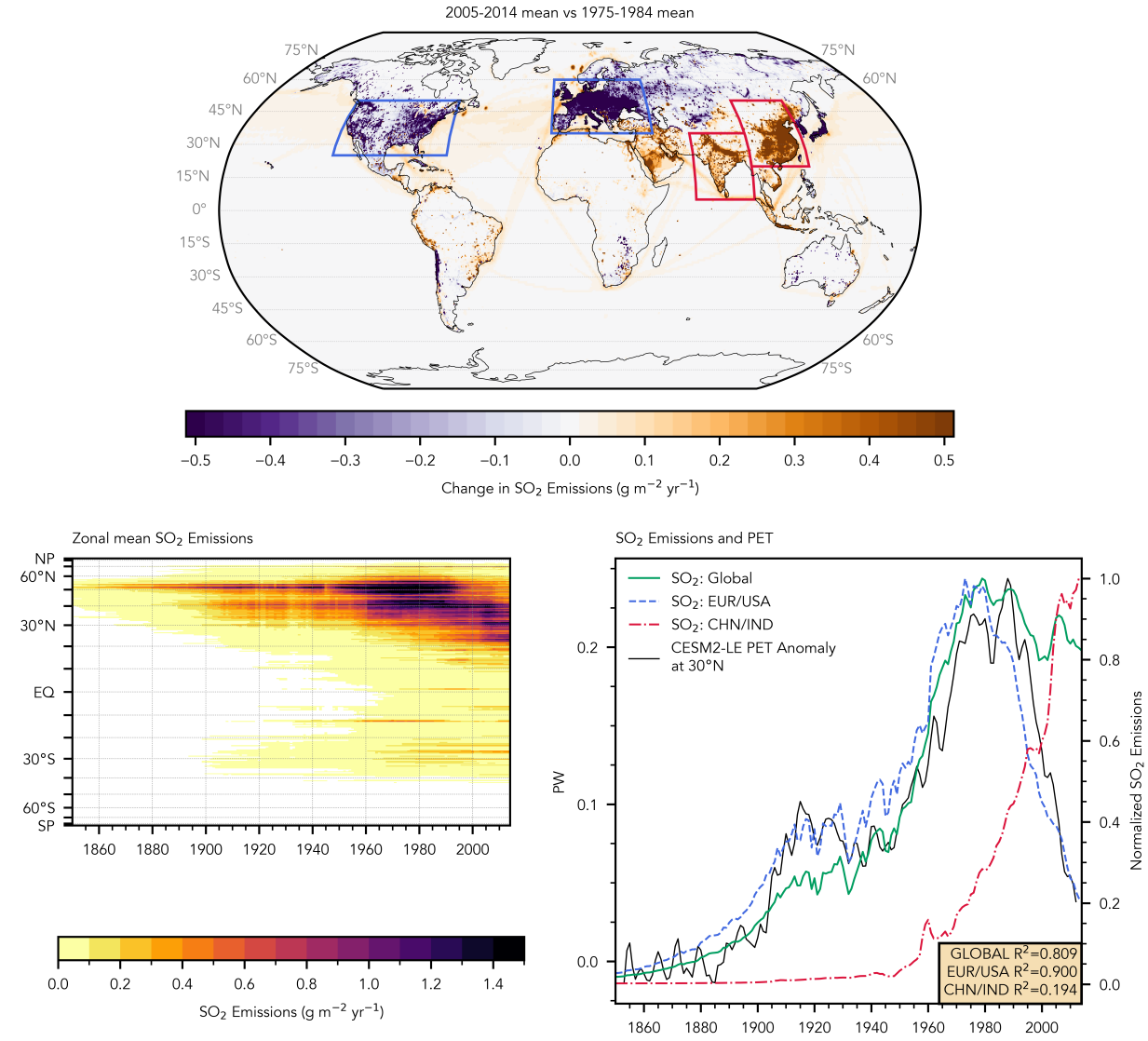

Figure 3.6: Top) Difference between time-mean SO_2 emissions for 2005-2014 minus 1975-1984. Bottom Left) Zonal mean SO_2 emissions from CEDS used as a contribution to the total anthropogenic aerosol forcing to the CESM2-LE. Values less than 0.01 g m^{-2}yr−1 masked. Bottom Right) Time series of normalized global SO_2 emissions from CEDS (Green Line: Global, Blue Dashed Line: Europe and USA, Red Dash-Dotted Line: China and India), and ensemble mean CESM2-LE PET anomaly at 30°N (Black Line). Latitude and longitude limits for boxes drawn to define regions are included in the text.

primary latitude of SO_2 emissions, and by the twenty-first century is joined by other maxima between 20°N-40°N.

The map in Fig. 3.6 shows the difference between the time-mean SO_2 emissions from the years 1975-1984, and those of the years 2005-2014. Purple (orange) colors show regions of re-

duced (increased) SO_2 emissions over the thirty year period. The decrease seen in North America and Europe can be explained by a combination of air quality legislation, a shift from manufacturing to service-based economies, and the fall of the former Soviet Union. At the same time, the orange regions in China, India, Southeast Asia and the Maritime Continent, and parts of the middle east are the consequence of rapid economic and population growth and increases in manufacturing (Hoesly et al., 2018). Also evident are increases in SO_2 emissions along prominent global shipping lanes.

The map and bottom-left panel show that the global SO_2 emissions did not simply peak and decrease over the historical period; instead, there is a complicated regional pattern and opposite trends in opposite regions. We now briefly investigate how those regional differences in SO_2 emissions correspond to the PET anomaly. The bottom-right panel of Fig. 3.6 shows the SO_2 emissions for the entire globe (green), combined emissions for Europe and the United States (EUR: 10°W-45°E, 35°N-60°N; USA: 125°W-65°W, 25°N-50°N; blue dashed line), and combined emissions for China and India (CHN: 95°E-125°E, 20°N-50°N; IND: 65°E-95°E, 5°N-35°N; red dash-dotted line). Emissions are normalized to give a maximum emission rate of 1. Also shown in black is the CESM2-LE ensemble mean PET anomaly at 30°N. From the beginning of the record through roughly 1975 the PET tracks closely with both the global emissions and emissions from only Europe and the United States (which made up the vast majority of emissions). After this period the green and blue curves diverge as SO_2 emissions decrease in the west and increase in other parts of the world, and the PET anomaly curve is highly correlated with the decline of emissions in Europe and North America (R^2=0.91). Throughout this time period the emissions from China and India are much less correlated with the PET anomaly (R^2=0.18) even though they combine to make up about half of global emissions by the end of the record. This is reminiscent of the work of Persad and Caldeira (2018), who showed that aerosol emissions from Western Europe had a global cooling effect that was fourteen times as strong as the same mass of aerosol emitted from India. The CHN/IND SO_2 emissions also mirror the ubiquitous

CO_2 emission trend (e.g., Fig. 2 of Hoesly et al., 2018), a point which we will return to in a few paragraphs.

Figure 3.7: Correlation between SO_2 emissions from various regions (rows) and CESM2-LE Ensemble Mean PET (columns, top table) CESM2-LE Ensemble Mean ASR (columns, bottom table) at various latitudes . Shading in each cell represents the value of the R^2 correlation coefficient.

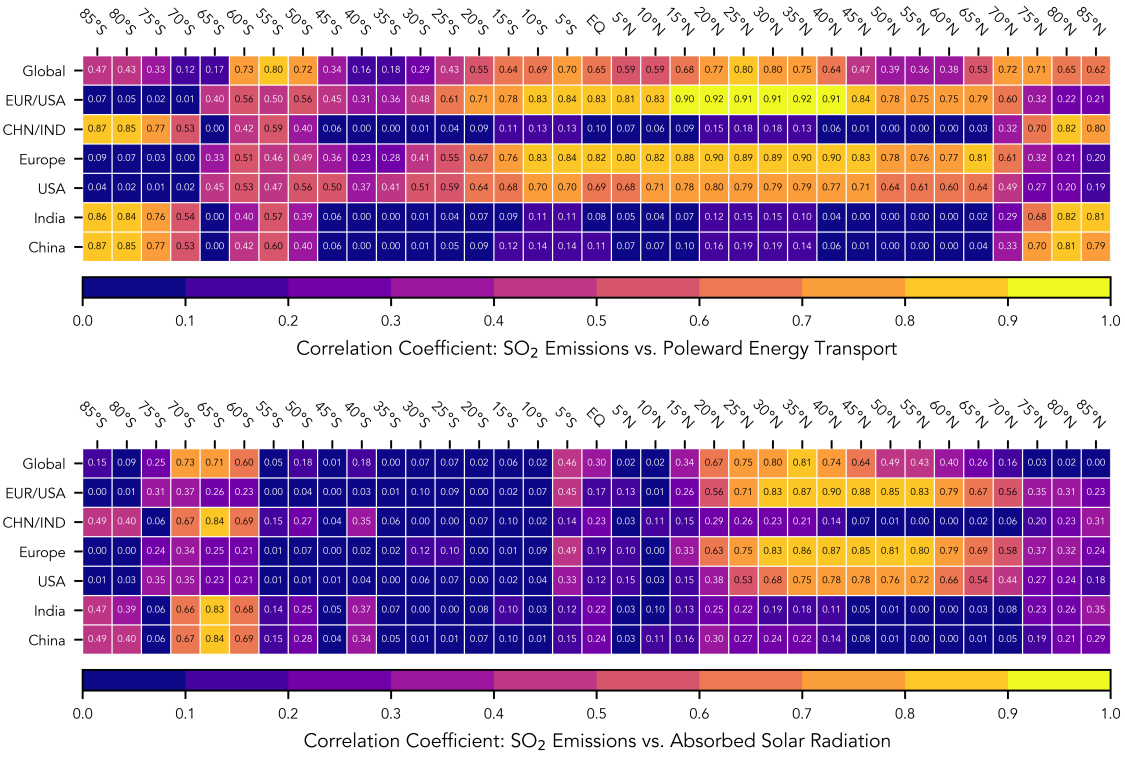

To emphasize the robustness of the relationship between the PET anomaly and SO_2 emissions, the top table in Fig. 3.7 shows the correlation coefficient at every 5° of latitude between the CESM2-LE ensemble mean PET and the SO_2 emissions from various regions. This Table shows that the correlations shown in the bottom right panel of Fig. 3.6 are not outliers: the global emission trend shows moderate correlation with the PET anomaly at most non-polar latitudes; the EUR/USA emissions are even more highly correlated, with R^2 >=0.5 for all latitudes between 25°S-70°N; and the CHN/IND emissions are very *uncorrelated* with the PET anomaly at most latitudes equatorward of 65° in either hemisphere. The Table also indicates that the emissions from Europe are slightly more correlated with the PET anomaly than those from the

USA. It is unclear whether this is evidence of a stronger relationship between EUR emissions and PET or is merely the result of chance.

The table also shows a high degree of correlation between emissions from CHN/IND and the PET anomaly near the poles. However, the authors do not believe this is a real relationship for several reasons: 1) the CHN/IND emissions of SO_2 increase in a way that is reminiscent of the increase in CO_2 which is expected to lead to an increase in poleward energy transport (Hwang and Frierson, 2010), 2) there is no obvious mechanism to explain how a northern hemispheric cooling from SO_2 emissions would lead to increased energy transport towards the south pole, and 3) the PET anomaly at these latitudes is at least an order of magnitude smaller than the PET anomaly near the equator (see Fig. 3.2).

The bottom table of Fig. 3.7 shows the correlation of SO_2 emissions with the zonal mean absorbed solar radiation (ASR, the difference between incoming and reflected shortwave radiation at the top of the atmosphere). Similar to our interpretation of the top table, we find that global SO_2 emissions are highly correlated (R^2=0.8) with the trend in ASR at a range of latitudes. These latitudes range from 205° N to 60°N, encompassing the industrialized countries of the northern hemisphere. We will discuss this link between SO_2, PET, and ASR further in the following section.

3.4 Discussion

3.4.1 Aerosol-Radiative Effects

We have shown that historical SO_2 emissions from Europe and North America are highly correlated with the anomalous northward heat transport in the mid-to-late twentieth century. The exact way in which sulphate aerosols mediate changes in atmospheric and oceanic heat transports will be the subject of an upcoming study, but we briefly discuss one important component here.

Aerosol-radiative effects occur in the longwave, but are largest in the shortwave. The (typically smaller) aerosol direct effect describes the direct scattering of radiation by aerosols, while

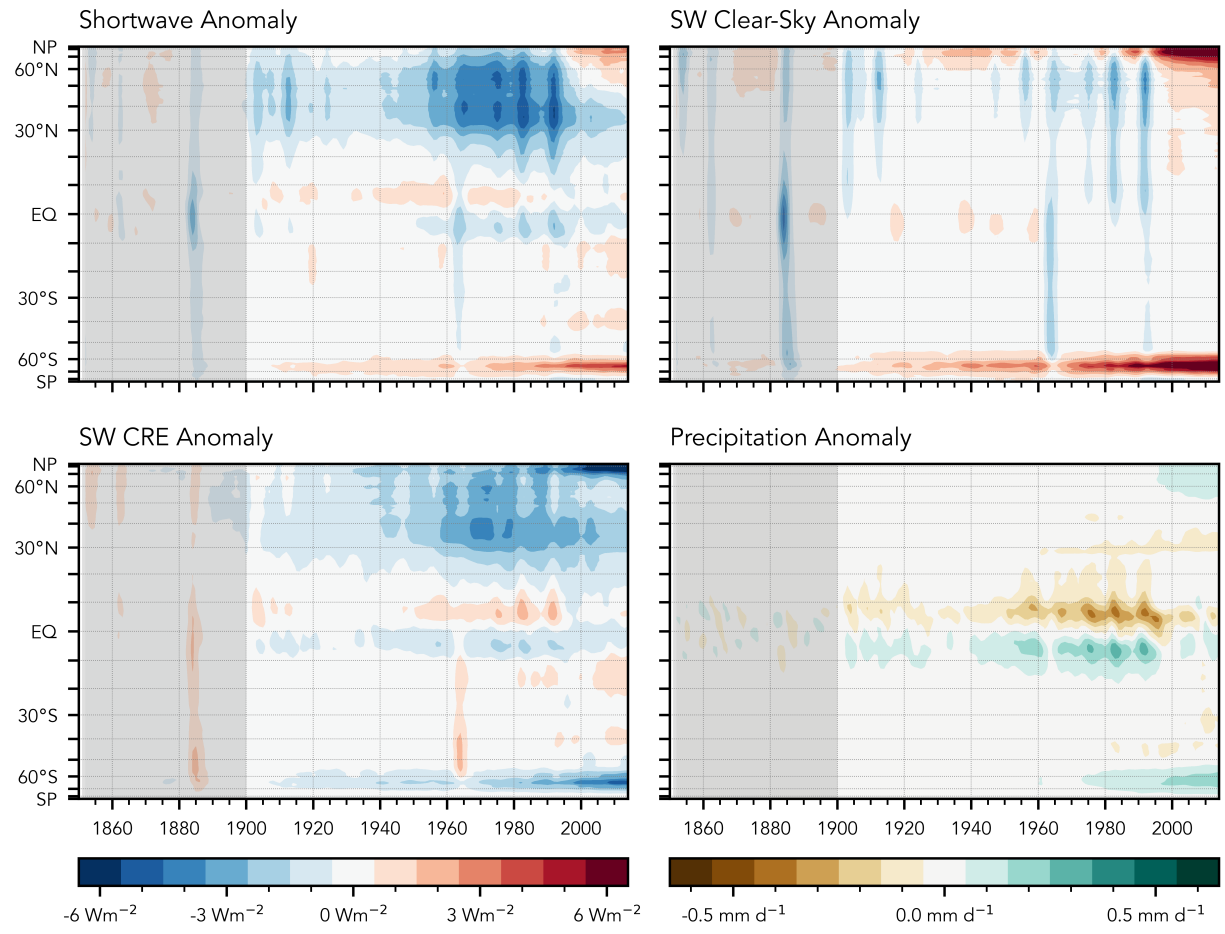

Figure 3.8: Top Left) Anomalous ensemble mean zonal mean shortwave flux at TOA, relative to 1851-1900 average. Top Right) Same as top left, but for the clear-sky shortwave flux at TOA. Bottom Left) Same as top left, but for the shortwave cloud radiative effect at the TOA (defined as full-sky minus clear-sky). Bottom Right) Same as top left, but for the total precipitation rate.

the (typically larger) aerosol indirect effect encompasses radiative impacts from aerosol-induced changes in clouds and precipitation (Twomey, 1977; Albrecht, 1989). We suspect that enhanced SO_2 emissions could have increased the reflection of shortwave radiation in the midlatitudes near the sources of emission, which would have increased the meridional albedo gradient. Following the argument of Stone (1978), the increased albedo gradient would imply an increase in northward energy transport to compensate for the reduction in absorbed shortwave radiation.

As a first-look at this explanation, the CESM2-LE ensemble mean full-sky shortwave anomaly relative to 1851-1900 is shown in the top left panel of Fig. 3.8, along with the clear-sky anomaly

(top right) and the shortwave cloud radiative effect (CRE, the difference between full-sky and clear-sky radiation, bottom left; Ramanathan, 1987; Allan, 2011). The full-sky anomaly shows a perturbation between 30°N-60°N centered around 1975. This full-sky perturbation is similar to, but poleward of, the PET anomaly in Fig. 3.2: it increases steadily through the twentieth century, increases rapidly after WWII, peaks near 1975, then decreases.

When comparing the clear-sky and CRE plots the perturbation appears to come primarily from the shortwave CRE, suggesting that the changes to the TOA shortwave balance - which lead to changes in the PET - are caused by aerosol cloud radiative effects rather than by the direct scattering of radiation. The largest signal in the clear-sky field prior to 2000 appears to be associated with high-frequency pulses associated with volcanoes. Eruptions inject sulphate aerosols into the stratosphere (Kremser et al., 2016) where there is not enough moisture to form optically thick clouds, compared to anthropogenic aerosols which primarily remain in the troposphere and often serve as cloud condensation nuclei.

Of course, clouds are not the only facet of the earth system which have the potential to alter the TOA shortwave balance. Another important component is northern hemisphere ice. A reduction in sea ice during the early twenty-first century may be the cause of the large *positive* shortwave anomaly found at northern high latitudes (see top-right corner of plots in the top row of Fig. 3.8). This *positive* ice-driven clear-sky anomaly occurred at the same time as SO_2 was primarily emitted from CHN/IND, and acted to counteract the *negative* cloud radiative effect anomaly so that the total shortwave anomaly reduced in magnitude.

In the context of PET, these figures suggest that SO_2 emissions from Europe and North America led to changes in cloud properties near the latitude of emission (i.e., 30°N-50°N). This different cloud regime increased the reflection of shortwave radiation back to space, which sharpened the meridional albedo gradient. The reduction in solar absorption in the midlatitudes required to anomalous northward energy transport.

One obvious impact of the SO_2-induced changes in PET, first identified by Hwang et al. (2013) and replicated here, can be seen in the bottom-right panel of Fig. 3.8, which shows the

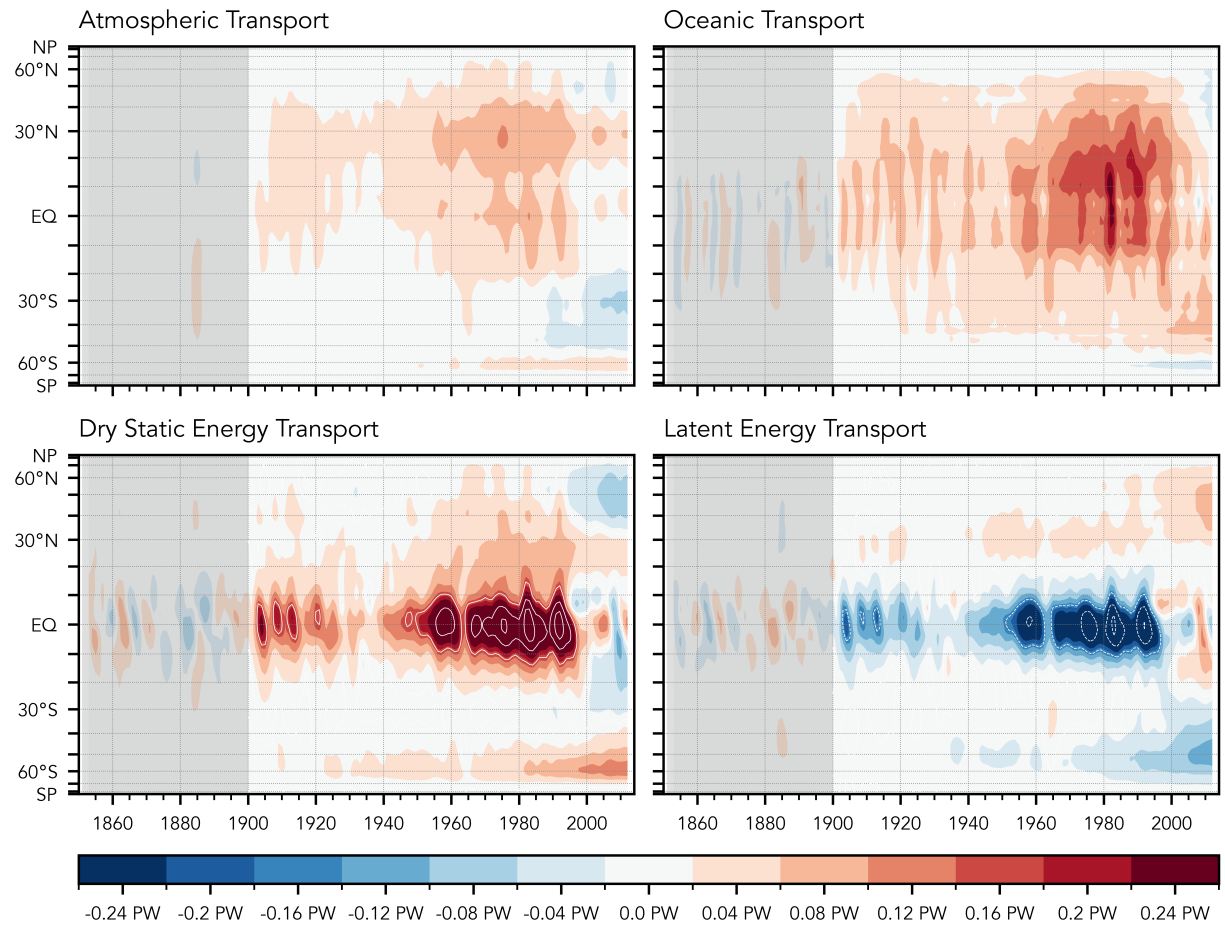

Figure 3.9: As in Fig. 3.2, but for the four constituent transports in Fig. 3.1. The white contours in bottom panels are drawn in increments of ± 0.16 PW, with negative values dashed. Note that these fields have also been smoothed with a 5-year filter.

precipitation anomaly relative to the 1851-1900 baseline. The peak and subsequent reduction in SO_2 emissions in Europe and North America corresponds to a southward advance and eventual retreat of the zonal mean equatorial rainband associated with the ITCZ and the anomalous Hadley circulation (Hwang et al., 2013; Yukimoto et al., 2022).

3.4.2 Partition of PET

So far this study has focused on the total PET by the climate system. However, the partition of energy transport between the atmosphere and ocean is also of importance. These contribu-

tions are shown in the top row of Fig. 3.9, and timeseries at different latitudes are shown in Fig. 3.10.

The top panels of Fig. 3.9 indicate that the PET anomaly first illustrated in Fig. 3.2 is composed of changes to both AHT and OHT. These changes are of a similar magnitude, and a similar temporal behavior, although there are differences in the latitudinal structure. The AHT anomaly is largest in the northern hemisphere from 20°N to 40°. Away from the equator, the majority of the atmospheric energy transport is accomplished by stationary and transient eddies. This suggests that aerosol forcing may have increased the energy transport associated with eddies in CESM2, a possibility that will be investigated in future work.

The AHT anomaly at the equator is still large, if slightly smaller than the anomaly centered at 30°N. The further decomposition of AHT into dry static energy transport and latent energy transport (bottom row of Fig. 3.9) indicates that this anomaly is the residual of the much larger and offsetting anomalies in these two constituent transports. A southward ITCZ shift as seen in Fig. 3.8 is driven by an increase in southward latent energy transport (blue contours) associated with an anomalous Hadley circulation. This more southerly position allows the ITCZ to export more dry static energy to the north, consistent with the energetic understanding of ITCZ dynamics (Donohoe et al., 2013; Bischoff and Schneider, 2014; Schneider et al., 2014; Adam et al., 2016).

The OHT anomaly appears to be somewhat larger than the AHT anomaly, with magnitude in excess of 0.2 PW compared to 0.16 PW. This OHT anomaly is also consistent with previous analyses of CESM2 specifically and CMIP6 models more generally that have found an increase in the strength of the AMOC in response to aerosol forcing (Menary et al., 2020; Hassan et al., 2021; Robson et al., 2022; Simpson et al., 2022). This suggests that the OHT anomaly is primarily due to changes in the AMOC.

The relative importance of the contributions to the total PET anomaly can be quantified by comparing the AHT and OHT timeseries at various latitudes in Fig. 3.10. From 10°S to 20°N the OHT anomaly is clearly larger than the AHT anomaly, sometimes by as much as a factor of

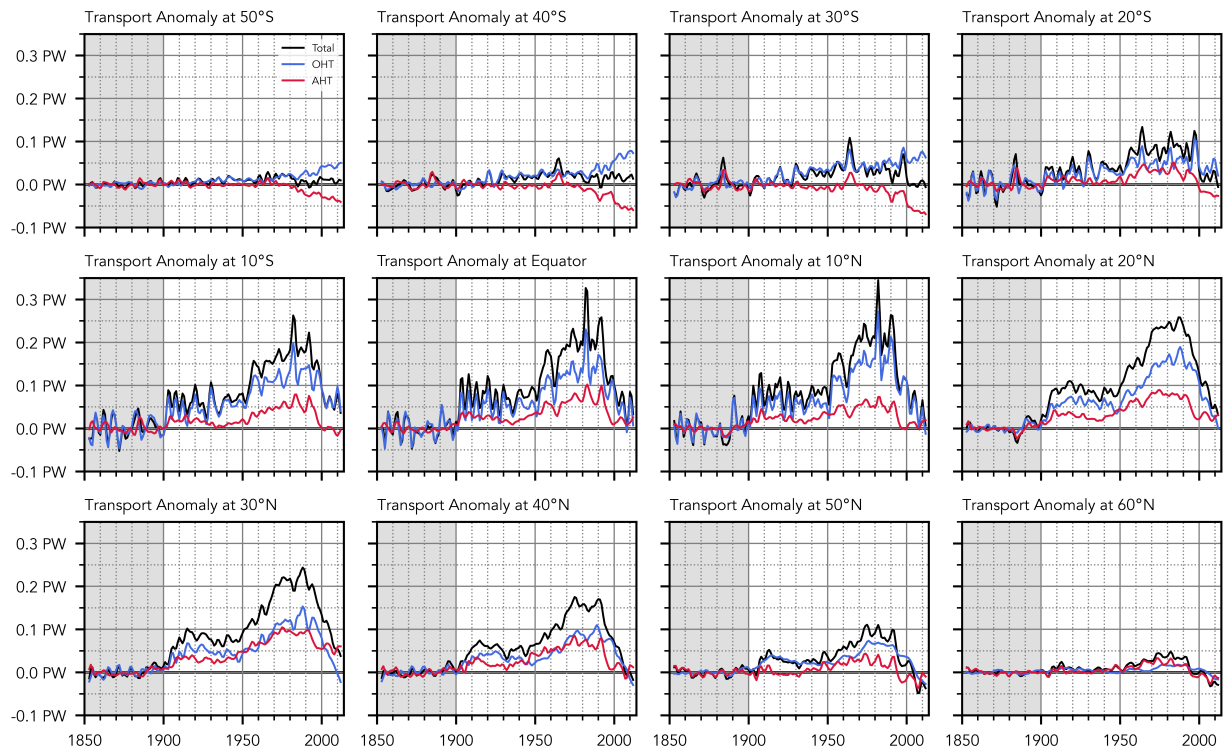

Figure 3.10: Timeseries of PET (black), OHT (blue), and AHT (red) anomalies at various latitudes, relative to the 1851-1900 baseline, and smoothed by the 5-year Gaussian filter.

3. In contrast, at 20°S and from 30°N to 50°N the AHT and OHT are approximately the same magnitude.

3.4.3 Nonlinear relationship between PET, Aerosol Emissions, and the Cryosphere

Figure 3.6 raises an interesting question of why SO_2 emissions in the twenty-first century - primarily from China and south Asia - are not correlated with the PET in a similar way to twentieth century emissions from Europe and North America. Here, we discuss several possible answers to this question.

One possibility is that the large quantity of black carbon emitted from China and India (Hoesly et al., 2018) offset the shortwave effect of the sulphate aerosols during the final years of the historical period. Black carbon, primarily emitted from residential biomass burning for heating and cooking, is a strong absorber of shortwave radiation. It is conceivable, then, that

the large quantity of black carbon emitted in the early years of the twenty-first century absorbed enough shortwave radiation to counteract the effect of SO_2 emissions. However, our results do not support this interpretation: the fact that the CESM2-SF AAER simulations, which include black carbon alongside SO_2 (Simpson et al., 2022), do show a major PET anomaly in the twenty-first century suggests that a different emissions regime is not likely to be the cause of the disconnect between the SO_2 forcing and the PET anomaly.

In fact, the difference between the PET anomaly found in the full CESM2-LE simulations and the anomaly found in the CESM2-SF AAER simulations is a key point. This indicates that the lack of a PET anomaly cannot be attributed to different responses to aerosols between the USA/EUR and IND/CHN regions (e.g., local cloud properties, latitude of emission, proximity to the AMOC, etc.) If these regional differences were the reason for the difference in the PET anomaly, then we would expect to see see a much more rapid decrease in the PET anomaly in the AAER simulations. Indeed, to first order, the PET anomaly in the AAER simulations appears to largely follow the global SO_2 emission trend (cf. Fig. 3.5 and the bottom panel of Fig. 3.6).

Instead of considering regional differences in response to aerosol emissions, the question now becomes what other processes could lead to a reduction in the shortwave anomaly (Fig. 3.8). From about 1995 through 2014, the northern hemisphere shortwave anomaly becomes less negative, and even becomes positive in the northern high latitudes. A comparison of the other panels of Fig. 3.8 indicates that this reduction is primarily driven by a positive *clear-sky* shortwave anomaly, with only a small reduction in the magnitude of the negative CRE anomaly during these years. That this clear-sky shortwave anomaly is driven by a high-latitude process suggests a cryosphere process as the likely cause.

To quantify this change in the shortwave field, Fig. 3.11 shows the hemispheric difference in absorbed solar radiation (ASR_HD). The ASR_HD was found by calculating the area-weighted average of the net shortwave flux at the TOA in both hemispheres, and then taking the difference of the southern minus the northern hemisphere (this convention was chosen so that

anomalies are positive throughout the historical period). This calculation was repeated for the net shortwave flux at the surface, and the net shortwave absorption within the atmosphere.

Panels in the left column of Fig. 3.11 show the ASR_HD for the CESM2-LE and for each of the CESM2-SF sub-ensembles; the right panel shows the comparison between the CESM2-LE and a linear sum of the ensemble means of each of the CESM2-SF sub-ensembles (e.g., AAER + BMB + GHG + EE). The shading in the right column shows the fifth to ninety-fifth percentile among CESM2-LE ensemble members.

The behavior of the curves in the left panel is quite similar to the analogous curves for the PET anomaly in Fig. 3.5. This is not surprising: the ASR_HD has previously been used as rough metric for the AMOC (Menary et al., 2020; Robson et al., 2022), and thus its relevance to the total poleward energy transport is obvious due to the large amount of cross-equatorial heat transport in the Atlantic basin (Trenberth and Fasullo, 2017; Trenberth et al., 2019; Forget and Ferreira, 2019; Newsom et al., 2021). In the absence of changes in the outgoing longwave radiation, the ASR_HD determines the amount of cross-equatorial energy transport that is required to maintain hemispheric energy balance. If the anomaly in the ASR_HD is positive (which indicates a darker southern hemisphere), this implies a larger amount of energy must be transported northward across the equator, consistent with the PET anomaly found in this study.

The primary take-away from Fig. 3.11 is that the CESM2-LE ASR_HD is largely recreated from a linear sum of CESM2-SF sub-ensembles from the beginning of the historical period until about 1995. After this point, the CESM2-LE curve drops rapidly, but the linear sum stays at about the same level (ignoring the large peaks clearly associated with the volcanic eruptions of Mt. Pinatubo and El Chichón in 1991 and 1982, respectively). This indicates a nonlinear response of the ASR_HD - and by extension the PET - to these climate forcings in CESM2 around the turn of the twenty-first century.

Comparison of the three panels in the right column indicates that this difference in ASR_HD between the CESM2-LE and the linear sum of CESM2-SF sub-ensembles is driven by the surface component of the shortwave, again consistent with an impact from cryosphere processes.

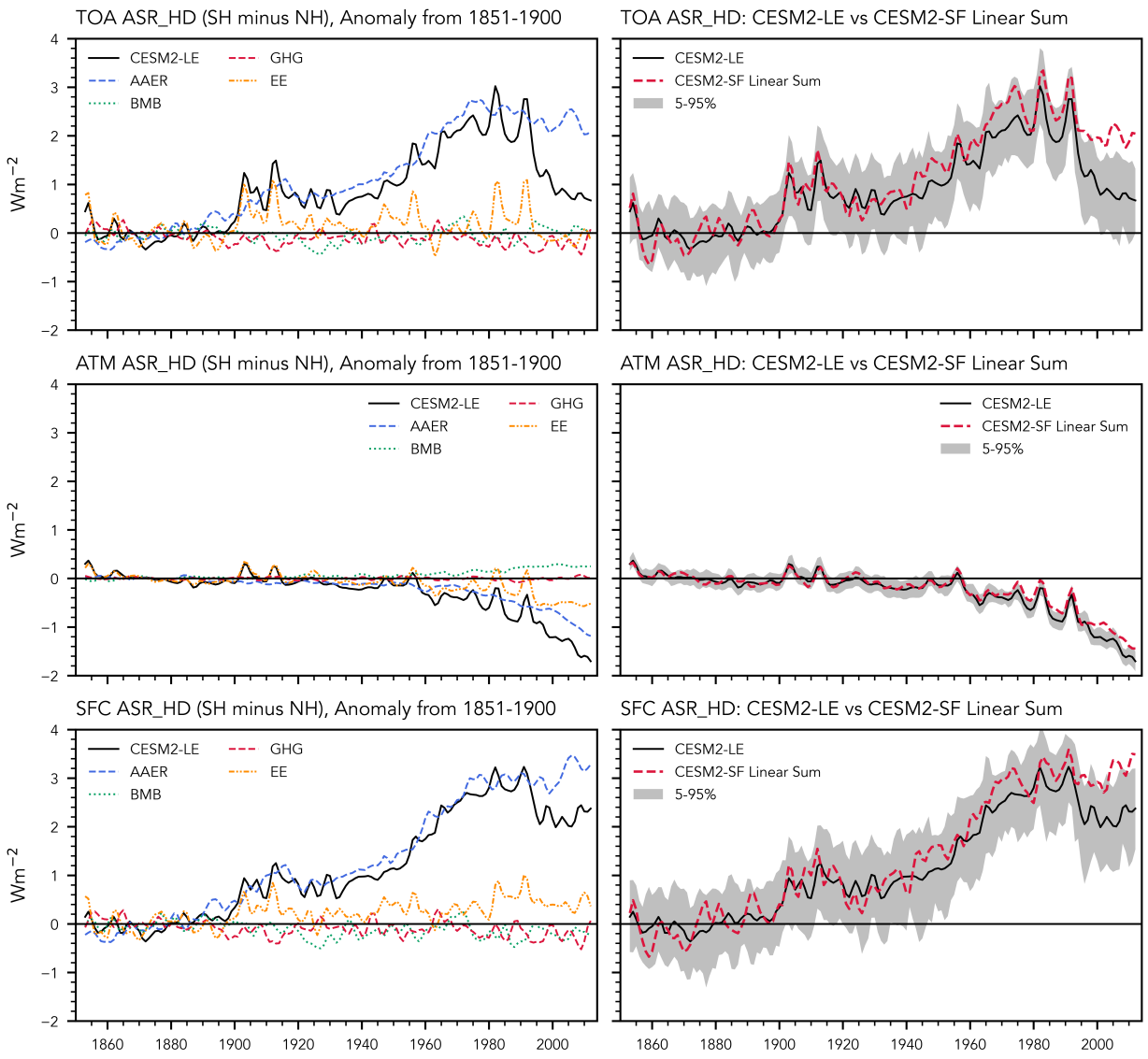

Figure 3.11: Positive values indicate that the NH reflects more shortwave radiation than the SH. Note that the shading in the right panel shows the range between the fifth and ninety-fifth percentiles, in comparison to the interquartile range of earlier figures.

This complicated relationship between aerosol emissions, surface shortwave radiation, and the cryosphere in the CESM2-SF simulations was discussed in detail by Simpson et al. (2022). In particular, Simpson et al. (2022) described that the relationship between aerosol emissions and northern hemisphere ice was state dependent: the cryosphere responses to aerosols was different in a cooler climate where aerosols were emitted alone compared to a warmer climate where aerosols were emitted alongside greenhouse gases. They found that an imposed aerosol forc-

ing in a climate *without* greenhouse gas warming increased the average snow cover by a larger amount than the same aerosol forcing in a climate *with* greenhouse warming. This leads to a larger surface albedo in the high latitudes of the cooler climate.

This state dependent relationship appears to explain why the ASR_HD - and by extension the PET - from CESM2-LE is not recreated by a simple linear sum of the CESM2-SF sub-ensembles from 2000-2014. This can be seen in the bottom panels of Fig. 3.11, where the linear sum of the ASR_HD from the CESM2-SF sub-ensembles (red dashed line, right panel) is larger than the ASR_HD from the CESM2-LE simulations (black line, right panel), due to the contribution from the AAER simulations (blue dashed line, left panel). In turn, this helps to explain why SO_2 emissions from India and China appear to have a smaller impact on the PET: the cryosphere processes counteract the shortwave impact of aerosols emitted from these regions. Cryosphere processes do not have the same impact during the last half of the twentieth century when emissions from Europe and North America were largest.

As an aside, our results for CESM2 are in contrast to those of Menary et al. (2020), who found that the ASR_HD in CMIP6 models was largely recreated from a linear sum of the ASR_HD in DAMIP simulations. This suggests that the rapid recovery in the PET anomaly after 1995 may be specific to CESM2, while the PET anomaly itself is likely a feature of a large number of CMIP6 models.

3.5 Conclusions

We have shown a robust link between historic anthropogenic SO_2 emissions and anomalous northward energy transport in the latter half of the twentieth century. Our study goes beyond previous studies which focused on the cross-equatorial transport to characterize the historic PET anomaly at all latitudes. This anomalous PET has been found in a large ensemble of climate simulations, a second ensemble of simulations forced only by historic anthropogenic aerosol emissions, as well in an atmospheric reanalysis.

Consistent with previous studies, we find that northern hemisphere anthropogenic SO_2 emissions - specifically from Europe and North America - increased the reflection of shortwave radiation back to space, primarily due to aerosol-radiative effects on clouds. By the early twenty-first century the zonal mean shortwave anomaly (Fig. 3.8) had become much smaller; consequently, the PET anomaly (Fig. 3.2) decreased as well. Our results suggest that this reduction in the shortwave anomaly is due to the increasing importance of cryosphere processes around and after the turn of the twenty-first century which complicate the simple relationship between SO_2 and PET found during the twentieth century.

Future work will explore the potential pathways that may explain how an increase in the reflection of shortwave radiation by mid-latitude clouds leads to an increase in the total northward energy transport by the atmosphere and oceans. For the oceans, it is possible that anthropogenic emissions over land may alter the surface energy balance over oceans, downstream of the source of emissions. This possibility is reminiscent of previous work which have attempted to characterize the impact of aerosol emissions on tropical cyclones through the framework of tropical cyclone potential intensity (Sobel et al., 2019, and references therein). In principle, this downstream effect could lead to a stronger SST gradient and a larger amount of energy transport even without a change in the ocean currents. However it appears that ocean currents do in fact change in CESM2 during the historical period: Simpson et al. (2022) found that the Atlantic meridional overturning circulation (AMOC) in CESM2 strengthened in response to historic forcing, largely driven by aerosol emissions.

The temporal evolution of the AMOC anomaly in the CESM2 Large Ensemble is quite similar to the PET anomaly discussed in this study (cf. Fig. 10 of Simpson et al. (2022) to Figs. 3.3 and 3.11, above). This is not surprising based on the amount of heat that is transported by the AMOC. We emphasize that the total PET anomaly discussed in this study cannot be immediately dismissed as a byproduct of the CESM2 AMOC response to historical forcing. Perhaps one-third of the total heat transport anomaly is due to an increase in atmospheric transport, as shown in Figs. 3.9 and 3.10.

From an annual-mean, zonal-mean perspective the cross-equatorial AHT anomaly is likely driven by an anomalous Hadley circulation (Hwang et al., 2013; Yukimoto et al., 2022), and the AHT further north is likely driven by changes in stationary and transient eddy heat transports. One possibility is that a reduction in absorbed shortwave radiation would increase the temperature difference between the tropics and the poles. Then, the energy transport would become more efficient leading to an increase in energy transport without requiring a change in the winds. A related possibility is that a sharper temperature gradient would lead to stronger and/or more frequent baroclinic eddies in the midlatitude winters, which could transport more energy towards the poles. A clearer understanding of the PET trends in different seasons and in different regions is crucial to fully understand the historical behavior we have described.

References

Acosta Navarro, J. C., Varma, V., Riipinen, I., Seland, Ø., Kirkevåg, A., Struthers, H., Iversen, T., Hansson, H.-C., and Ekman, A. M. L. (2016). Amplification of arctic warming by past air pollution reductions in europe. *Nat. Geosci.*, 9(4):277–281.

Adam, O., Bischoff, T., and Schneider, T. (2016). Seasonal and interannual variations of the energy flux equator and ITCZ. part i: Zonally averaged ITCZ position. *J. Clim.*, 29(9):3219–3230.

Aizawa, T., Oshima, N., and Yukimoto, S. (2022). Contributions of anthropogenic aerosol forcing and multidecadal internal variability to mid-20th century arctic cooling—CMIP6/DAMIP multimodel analysis. *Geophys. Res. Lett.*, 49(4).

Albrecht, B. A. (1989). Aerosols, cloud microphysics, and fractional cloudiness. *Science*, 245(4923):1227–1230.

Allan, R. P. (2011). Combining satellite data and models to estimate cloud radiative effect at the surface and in the atmosphere. *Met. Apps*, 18(3):324–333.

Allen, R. J., Evan, A. T., and Booth, B. B. B. (2015). Interhemispheric aerosol radiative forcing and tropical precipitation shifts during the late twentieth century. *J. Clim.*, 28(20):8219–8246.

Armour, K. C., Siler, N., Donohoe, A., and Roe, G. H. (2019). Meridional atmospheric heat transport constrained by energetics and mediated by Large-Scale diffusion. *J. Clim.*, 32(12):3655–3680.

Bischoff, T. and Schneider, T. (2014). Energetic constraints on the position of the intertropical convergence zone. *J. Clim.*, 27(13):4937–4951.

Bjerknes, J. (1964). Atlantic Air-Sea interaction. *Adv. Geophys.*, 10:1–82.

Caesar, L., McCarthy, G. D., Thornalley, D. J. R., Cahill, N., and Rahmstorf, S. (2021). Current atlantic meridional overturning circulation weakest in last millennium. *Nat. Geosci.*, 14(3):118–120.

Caesar, L., Rahmstorf, S., Robinson, A., Feulner, G., and Saba, V. (2018). Observed fingerprint of a weakening atlantic ocean overturning circulation. *Nature*, 556(7700):191–196.

Chiang, J. C. H. and Bitz, C. M. (2005). Influence of high latitude ice cover on the marine intertropical convergence zone. *Clim. Dyn.*, 25(5):477–496.

Clark, J. P., Feldstein, S. B., and Lee, S. (2022). Moist static energy transport trends in four global reanalyses: Are they downgradient? *Geophys. Res. Lett.*

Cox, T., Donohoe, A., Roe, G. H., Armour, K. C., and Frierson, D. M. W. (2022). Near invariance of poleward atmospheric heat transport in response to midlatitude orography. *J. Clim.*, 35(13):4099–4113.

Danabasoglu, G., Lamarque, J.-F., Bacmeister, J., Bailey, D. A., DuVivier, A. K., Edwards, J., Emmons, L. K., Fasullo, J., Garcia, R., Gettelman, A., Hannay, C., Holland, M. M., Large, W. G., Lauritzen, P. H., Lawrence, D. M., Lenaerts, J. T. M., Lindsay, K., Lipscomb, W. H., Mills, M. J., Neale, R., Oleson, K. W., Otto-Bliesner, B., Phillips, A. S., Sacks, W., Tilmes, S., Kampenhout, L., Vertenstein, M., Bertini, A., Dennis, J., Deser, C., Fischer, C., Fox-Kemper, B., Kay, J. E., Kinnison, D., Kushner, P. J., Larson, V. E., Long, M. C., Mickelson, S., Moore, J. K., Nienhouse, E., Polvani, L., Rasch, P. J., and Strand, W. G. (2020). The community earth system model version 2 (CESM2). *J. Adv. Model. Earth Syst.*, 12(2).

Deser, C., Phillips, A. S., Simpson, I. R., Rosenbloom, N., Coleman, D., Lehner, F., Pendergrass, A. G., DiNezio, P., and Stevenson, S. (2020). Isolating the evolving contributions of anthropogenic aerosols and greenhouse gases: A new CESM1 large ensemble community resource. *J. Clim.*, 33(18):7835–7858.

Donohoe, A., Armour, K. C., Roe, G. H., Battisti, D. S., and Hahn, L. (2020). The partitioning of meridional heat transport from the last glacial maximum to CO2 quadrupling in coupled climate models. *J. Clim.*, 33(10):4141–4165.

Donohoe, A., Marshall, J., Ferreira, D., and Mcgee, D. (2013). The relationship between ITCZ location and Cross-Equatorial atmospheric heat transport: From the seasonal cycle to the last glacial maximum. *J. Clim.*, 26(11):3597–3618.

Donohoe, A. and Voigt, A. (2017). Why future shifts in tropical precipitation will likely be small: The location of the tropical rain belt and the hemispheric contrast of energy input to the atmosphere. In Wang, S.-Y. S., Yoon, J.-H., Funk, C. C., and Gillies, R. R., editors, *Climate Extremes*, volume 6 of *Geophysical Monograph Series*, pages 115–137. John Wiley & Sons, Inc., Hoboken, NJ, USA.

Enderton, D. and Marshall, J. (2009). Explorations of Atmosphere–Ocean–Ice climates on an aquaplanet and their meridional energy transports. *J. Atmos. Sci.*, 66(6):1593–1611.

England, M. R., Eisenman, I., Lutsko, N. J., and Wagner, T. J. W. (2021). The recent emergence of arctic amplification. *Geophys. Res. Lett.*, 48(15):e2021GL094086.

Eyring, V., Bony, S., Meehl, G. A., Senior, C. A., Stevens, B., Stouffer, R. J., and Taylor, K. E. (2016). Overview of the coupled model intercomparison project phase 6 (CMIP6) experimental design and organization. *Geosci. Model Dev.*, 9(5):1937–1958.

Fasullo, J. T., Lamarque, J.-F., Hannay, C., Rosenbloom, N., Tilmes, S., DeRepentigny, P., Jahn, A., and Deser, C. (2022). Spurious late historical-era warming in CESM2 driven by prescribed biomass burning emissions. *Geophys. Res. Lett.*, 49(2).

Forget, G. and Ferreira, D. (2019). Global ocean heat transport dominated by heat export from the tropical pacific. *Nat. Geosci.*, 12(5):351–354.

Frierson, D. M. W., Hwang, Y.-T., Fučkar, N. S., Seager, R., Kang, S. M., Donohoe, A., Maroon, E. A., Liu, X., and Battisti, D. S. (2013). Contribution of ocean overturning circulation to tropical rainfall peak in the northern hemisphere. *Nat. Geosci.*, 6(11):940–944.

Grennfelt, P., Engleryd, A., Forsius, M., Hov, Ø., Rodhe, H., and Cowling, E. (2020). Acid rain and air pollution: 50 years of progress in environmental science and policy. *Ambio*, 49(4):849–864.

Gulev, S. K., Thorne, P. W., Ahn, J., Dentener, F. J., Domingues, C. M., Gerland, S., Gong, D., Kaufman, D. S., Nnamchi, H. C., Quaas, J., Rivera, J. A., Sathyendranath, S., Smith, S. L., Trewin, B., von Shuckmann, K., and Vose, R. S. (2021). Changing state of the climate system. In Masson-Delmotte, V., Zhai, P., Pirani, A., Connors, S. L., Péan, C., Berger, S., Caud, N., Chen, Y., Goldfarb, L., Gomis, M. I., Huang, M., Leitzell, K., Lonnoy, E., Matthews, J. B. R., Maycock, T. K., Waterfield, T., Yelekçi, O., Yu, R., and Zhou, B., editors, *Climate Change 2021: The Physical Science Basis. Contribution of Working Group I to the Sixth Assessment Report of the Intergovernmental Panel on Climate Change*, chapter 2. Cambridge University Press, Cambridge, United Kingdom and New York, NY, USA.

Hassan, T., Allen, R. J., Liu, W., and Randles, C. A. (2021). Anthropogenic aerosol forcing of the atlantic meridional overturning circulation and the associated mechanisms in CMIP6 models. *Atmos. Chem. Phys.*, 21(8):5821–5846.

Held, I. M. (2001). The partitioning of the poleward energy transport between the tropical ocean and atmosphere. *J. Atmos. Sci.*, 58(8):943–948.

Held, I. M. and Soden, B. J. (2006). Robust responses of the hydrological cycle to global warming. *J. Clim.*, 19(21):5686–5699.

Hersbach, H., Bell, B., Berrisford, P., Hirahara, S., Horányi, A., Muñoz-Sabater, J., Nicolas, J., Peubey, C., Radu, R., Schepers, D., Simmons, A., Soci, C., Abdalla, S., Abellan, X., Balsamo, G., Bechtold, P., Biavati, G., Bidlot, J., Bonavita, M., Chiara, G., Dahlgren, P., Dee, D., Diamantakis, M., Dragani, R., Flemming, J., Forbes, R., Fuentes, M., Geer, A., Haimberger, L., Healy, S., Hogan, R. J., Hólm, E., Janisková, M., Keeley, S., Laloyaux, P., Lopez, P., Lupu, C., Radnoti, G., Rosnay, P., Rozum, I., Vamborg, F., Villaume, S., and Thépaut, J. (2020). The ERA5 global reanalysis. *Q.J.R. Meteorol. Soc.*, 146(730):1999–2049.

Hoesly, R. M., Smith, S. J., Feng, L., Klimont, Z., Janssens-Maenhout, G., Pitkanen, T., Seibert, J. J., Vu, L., Andres, R. J., Bolt, R. M., Bond, T. C., Dawidowski, L., Kholod, N., Kurokawa, J.-I., Li, M., Liu, L., Lu, Z., Moura, M. C. P., O'Rourke, P. R., and Zhang, Q. (2018). Historical (1750–2014) anthropogenic emissions of reactive gases and aerosols from the community emissions data system (CEDS). *Geosci. Model Dev.*, 11(1):369–408.

Huang, Y., Xia, Y., and Tan, X. (2017). On the pattern of CO2 radiative forcing and poleward energy transport. *J. Geophys. Res.*, 122(20):10,578–10,593.

Huguenin, M. F., Holmes, R. M., and England, M. H. (2022). Drivers and distribution of global ocean heat uptake over the last half century. *Nat. Commun.*, 13(1):4921.

Hwang, Y.-T. and Frierson, D. M. W. (2010). Increasing atmospheric poleward energy transport with global warming. *Geophys. Res. Lett.*, 37(24).

Hwang, Y.-T., Frierson, D. M. W., and Kang, S. M. (2013). Anthropogenic sulfate aerosol and the southward shift of tropical precipitation in the late 20th century. *Geophys. Res. Lett.*, 40(11):2845–2850.

Hwang, Y.-T., Frierson, D. M. W., and Kay, J. E. (2011). Coupling between arctic feedbacks and changes in poleward energy transport. *Geophys. Res. Lett.*, 38(17).

Irving, D. B., Wijffels, S., and Church, J. A. (2019). Anthropogenic aerosols, greenhouse gases, and the uptake, transport, and storage of excess heat in the climate system. *Geophys. Res. Lett.*, 46(9):4894–4903.

Kang, S. M. (2020). Extratropical influence on the tropical rainfall distribution. *Current Climate Change Reports*, 6(1):24–36.

Kang, S. M., Held, I. M., Frierson, D. M. W., and Zhao, M. (2008). The response of the ITCZ to extratropical thermal forcing: Idealized slab-ocean experiments with a GCM. *J. Clim.*, 21(14):3521–3532.

Knietzsch, M.-A., Schröder, A., Lucarini, V., and Lunkeit, F. (2015). The impact of oceanic heat transport on the atmospheric circulation. *Earth Syst. Dyn.*, 6(2):591–615.

Kremser, S., Thomason, L. W., von Hobe, M., Hermann, M., Deshler, T., Timmreck, C., Toohey, M., Stenke, A., Schwarz, J. P., Weigel, R., Fueglistaler, S., Prata, F. J., Vernier, J.-P., Schlager, H., Barnes, J. E., Antuña-Marrero, J.-C., Fairlie, D., Palm, M., Mahieu, E., Notholt, J., Rex, M., Bingen, C., Vanhellemont, F., Bourassa, A., Plane, J. M. C., Klocke, D., Carn, S. A., Clarisse, L., Trickl, T., Neely, R., James, A. D., Rieger, L., Wilson, J. C., and Meland, B. (2016). Stratospheric aerosol-observations, processes, and impact on climate. *Rev. Geophys.*, 54(2):278–335.

Larssen, T., Lydersen, E., Tang, D., He, Y., Gao, J., Liu, H., Duan, L., Seip, H. M., Vogt, R. D., Mulder, J., Shao, M., Wang, Y., Shang, H., Zhang, X., Solberg, S., Aas, W., Okland, T., Eilertsen, O., Angell, V., Li, Q., Zhai, D., Xiang, R., Xiao, J., and Luo, J. (2006). Acid rain in china. *Environ. Sci. Technol.*, 40(2):418–425.

Lembo, V., Folini, D., Wild, M., and Lionello, P. (2019). Inter-hemispheric differences in energy budgets and cross-equatorial transport anomalies during the 20th century. *Clim. Dyn.*, 53(1):115–135.

Lu, J., Zhou, W., Kong, H., Ruby Leung, L., Harrop, B., and Song, F. (2022). On the diffusivity of moist static energy and implications for the polar amplification response to climate warming. *J. Clim.*, -1(aop):1–51.

Marshall, J., Donohoe, A., Ferreira, D., and McGee, D. (2013). The ocean's role in setting the mean position of the Inter-Tropical convergence zone. *Clim. Dyn.*, 42(7):1967–1979.

Menary, M. B., Robson, J., Allan, R. P., Booth, B. B. B., Cassou, C., Gastineau, G., Gregory, J., Hodson, D., Jones, C., Mignot, J., Ringer, M., Sutton, R., Wilcox, L., and Zhang, R. (2020). Aerosol-forced AMOC changes in CMIP6 historical simulations. *Geophys. Res. Lett.*, 47(14).

Naik, V., Szopa, S., Adhikary, B., Artaxo, P., Berntsen, T., Collins, W. D., Fuzzi, S., Gallardo, L., Kiendler Scharr, A., Klimont, Z., Liao, H., Unger, N., and Zanis, P. (2021). Short-Lived climate forcers. In Masson-Delmotte, V., Zhai, P., Pirani, A., Connors, S. L., Péan, C., Berger, S., Caud, N., Chen, Y., Goldfarb, L., Gomis, M. I., Huang, M., Leitzell, K., Lonnoy, E., Matthews, J. B. R.,

Maycock, T. K., Waterfield, T., Yelekçi, O., Yu, R., and Zhou, B., editors, *Climate Change 2021: The Physical Science Basis. Contribution of Working Group I to the Sixth Assessment Report of the Intergovernmental Panel on Climate Change*, chapter 6. Cambridge University Press, Cambridge, United Kingdom and New York, NY, USA.

Needham, M. R. and Randall, D. A. (2023). Anomalous northward energy transport due to anthropogenic aerosols during the 20th century. *J. Clim.*, -1(aop):1–37.

Neelin, J. D. and Held, I. M. (1987). Modeling tropical convergence based on the moist static energy budget. *Mon. Weather Rev.*, 115(1):3–12.

Newsom, E. R., Thompson, A. F., Adkins, J. F., and Galbraith, E. D. (2021). A hemispheric asymmetry in poleward ocean heat transport across climates: Implications for overturning and polar warming. *Earth Planet. Sci. Lett.*, 568:117033.

Oort, A. H. (1971). The observed annual cycle in the meridional transport of atmospheric energy. *J. Atmos. Sci.*, 28(3):325–339.

Persad, G. G. and Caldeira, K. (2018). Divergent global-scale temperature effects from identical aerosols emitted in different regions. *Nat. Commun.*, 9(1):3289.

Pithan, F. and Jung, T. (2021). Arctic amplification of precipitation changes - the energy hypothesis. *Geophys. Res. Lett.*

Previdi, M., Smith, K. L., and Polvani, L. M. (2021). Arctic amplification of climate change: a review of underlying mechanisms. *Environ. Res. Lett.*, 16(9):093003.

Rahmstorf, S., Box, J. E., Feulner, G., Mann, M. E., Robinson, A., Rutherford, S., and Schaffernicht, E. J. (2015). Exceptional twentieth-century slowdown in atlantic ocean overturning circulation. *Nat. Clim. Chang.*, 5(5):475–480.

Ramanathan, V. (1987). The role of earth radiation budget studies in climate and general circulation research. *J. Geophys. Res.*, 92(D4):4075.

Riehl, H. and Malkus, J. S. (1958). On the heat balance in the equatorial trough zone. *Geophysica*, 6:503–537.

Robson, J., Menary, M. B., Sutton, R. T., Mecking, J., Gregory, J. M., Jones, C., Sinha, B., Stevens, D. P., and Wilcox, L. J. (2022). The role of anthropogenic aerosol forcing in the 1850–1985 strengthening of the AMOC in CMIP6 historical simulations. *J. Clim.*, 35(20):3243–3263.

Rodgers, K. B., Lee, S.-S., Rosenbloom, N., Timmermann, A., Danabasoglu, G., Deser, C., Edwards, J., Kim, J.-E., Simpson, I. R., Stein, K., Stuecker, M. F., Yamaguchi, R., Bódai, T., Chung, E.-S., Huang, L., Kim, W. M., Lamarque, J.-F., Lombardozzi, D. L., Wieder, W. R., and Yeager, S. G. (2021). Ubiquity of human-induced changes in climate variability. *Earth Syst. Dyn.*, 12(4):1393–1411.

Rose, B. E. J. and Ferreira, D. (2012). Ocean heat transport and water vapor greenhouse in a warm equable climate: A new look at the low gradient paradox. *J. Clim.*, 26(6):2117–2136.

Rosenfeld, D., Andreae, M. O., Asmi, A., Chin, M., de Leeuw, G., Donovan, D. P., Kahn, R., Kinne, S., Kivekäs, N., Kulmala, M., Lau, W., Schmidt, K. S., Suni, T., Wagner, T., Wild, M., and Quaas, J. (2014). Global observations of aerosol-cloud-precipitation-climate interactions. *Rev. Geophys.*, 52(4):750–808.

Schneider, T., Bischoff, T., and Haug, G. H. (2014). Migrations and dynamics of the intertropical convergence zone. *Nature*, 513(7516):45–53.

Screen, J. A., Deser, C., and Simmonds, I. (2012). Local and remote controls on observed arctic warming. *Geophys. Res. Lett.*, 39(10).

Serreze, M. C. and Barry, R. G. (2011). Processes and impacts of arctic amplification: A research synthesis. *Glob. Planet. Change*, 77(1-2):85–96.

Shaw, T. A. and Smith, Z. (2022). The midlatitude response to polar sea ice loss: Idealized Slab-Ocean aquaplanet experiments with thermodynamic sea ice. *J. Clim.*, 35(8):2633–2649.

Shindell, D., Schulz, M., Ming, Y., Takemura, T., Faluvegi, G., and Ramaswamy, V. (2010). Spatial scales of climate response to inhomogeneous radiative forcing. *J. Geophys. Res.*, 115(D19).

Siler, N., Roe, G. H., and Armour, K. C. (2018). Insights into the Zonal-Mean response of the hydrologic cycle to global warming from a diffusive energy balance model. *J. Clim.*, 31(18):7481–7493.

Simpson, I. R., Rosenbloom, N., Danabasoglu, G., Deser, C., Yeager, S. G., McCluskey, C. S., Yamaguchi, R., Lamarque, J.-F., Tilmes, S., Mills, M. J., and Rodgers, K. B. (2022). The CESM2 single forcing large ensemble and comparison to CESM1: Implications for experimental design. Prepublished Manuscript.

Sobel, A. H., Camargo, S. J., and Previdi, M. (2019). Aerosol versus greenhouse gas effects on tropical cyclone potential intensity and the hydrologic cycle. *Journal of Climate; Boston*, 32(17):5511–5527.

Stone, P. H. (1978). Constraints on dynamical transports of energy on a spherical planet. *Dyn. Atmos. Oceans*, 2(2):123–139.

Sverdrup, H. U. (1942). *The Oceans Their Physics, Chemistry, and General Biology*. Prentive-Hall, INC.

Trenberth, K. E. (1979). Mean annual poleward energy transports by the oceans in the southern hemisphere. *Dyn. Atmos. Oceans*, 4(1):57–64.

Trenberth, K. E. and Caron, J. M. (2001). Estimates of meridional atmosphere and ocean heat transports. *J. Clim.*, 14(16):3433–3443.

Trenberth, K. E. and Fasullo, J. T. (2017). Atlantc meridional heat transports computed from balancing earth's energy locally. *Geophys. Res. Lett.*, 44(4):1919–1927.

Trenberth, K. E. and Stepaniak, D. P. (2003). Seamless poleward atmospheric energy transports and implications for the hadley circulation. *J. Clim.*, 16(22):3706–3722.

Trenberth, K. E. and Stepaniak, D. P. (2004). The flow of energy through the earth's climate system. *Q. J. R. Meteorol. Soc.*, 130(603):2677–2701.

Trenberth, K. E. and Zhang, Y. (2019). Observed interhemispheric meridional heat transports and the role of the indonesian throughflow in the pacific ocean. *J. Clim.*, 32(24):8523–8536.

Trenberth, K. E., Zhang, Y., Fasullo, J. T., and Cheng, L. (2019). Observation-Based estimates of global and basin ocean meridional heat transport time series. *J. Clim.*, 32(14):4567–4583.

Twomey, S. (1977). The influence of pollution on the shortwave albedo of clouds. *J. Atmos. Sci.*, 34(7):1149–1152.

Vonder Haar, T. H. and Oort, A. H. (1973). New estimate of annual poleward energy transport by northern hemisphere oceans. *J. Phys. Oceanogr.*, 3(2):169–172.

Yang, H., Li, Q., Wang, K., Sun, Y., and Sun, D. (2015). Decomposing the meridional heat transport in the climate system. *Clim. Dyn.*, 44(9):2751–2768.

Yukimoto, S., Oshima, N., Kawai, H., Deushi, M., and Aizawa, T. (2022). Role of interhemispheric heat transport and global atmospheric cooling in multidecadal trends of northern hemisphere precipitation. *Geophys. Res. Lett.*, 49(18).

Chapter 4

Aerosol-Induced Changes in Atmospheric and Oceanic Heat Transports in the CESM2 Large Ensemble

This chapter is an exact republication of the text and figures (with the exception of section numbering, which has been modified to align with the larger numbering of this dissertation) from the article of the same name (Needham et al., 2024a) originally published in the *Journal of Climate* in August, 2024, under the DOI: **10.1175/JCLI-D-23-0455.1**

Overview

The total poleward energy transport (PET) is set by the top of atmosphere radiation flux, and is therefore sensitive to any process which can alter those fluxes, particularly in the shortwave. One example is the direct and indirect effects of anthropogenic aerosols, which increase the local reflection of solar radiation back to space. The historic emission of sulphur dioxide, which peaked in the northern midlatitudes during the 1980s, has been proposed as a primary contributor to historic anomalies in cross-equatorial energy transport, as well as related processes such as a shift in the tropical rainband.

In this study, we analyze simulations from the CESM2 large ensemble and single-forcing projects to better understand the forced response of PET to historical forcings. First, analysis of the single-forcing project reveals that the position of the ITCZ responds in a non-linear manner to greenhouse gas forcing in CESM2. This type of non-linearity has been found previously in the context of the aerosol-only simulations in the CESM2 single-forcing project, but may be the first identification of a similar effect in the greenhouse gas-only simulations.

Second, through analysis of the full CESM2 large ensemble simulations, we find that anomalous heat transport occurred in both the atmosphere (through the mean meridional circulation and atmospheric eddies) and in the oceans (through the Atlantic and Indo-Pacific sectors) due to a variety of related processes including the Hadley cells, the midlatitude storm tracks, the Atlantic Meridional Overturning Circulation (AMOC), and the Pacific wind-driven subtropical gyre.

Significance Statement

In this study, we investigate how the earth system changed the transport of energy from the tropics to the poles in response to historic pollution. We analyze a large number of climate model simulations of the recent past (1850-present) and find that historic emissions of sulphur dioxide caused the model to transport more energy in the form of stronger ocean currents, stronger storms, and stronger prevailing winds. This is because the modeled currents in the Atlantic were too sensitive to historic pollution and transported too much warm water northward.

4.1 Introduction

Virtually every phenomenon of the climate system is ultimately driven by the absorption of radiative energy from the sun, and the requirement that the earth balance this solar heating via the blackbody emission of longwave radiation (Kiehl and Trenberth, 1997; Trenberth et al., 2009; von Schuckmann et al., 2016). This balance does not hold instantaneously at each point, but

rather holds in an aggregate sense, both spatially and temporally. Observations (Ramanathan, 1987; Ramanathan et al., 1989; Loeb et al., 2018) show that the equatorial regions absorb more shortwave energy than they lose to longwave emission, while the opposite is true at the poles. This fact necessitates a poleward energy transport (PET) out of the tropics, of which the vast majority is accomplished by the atmosphere and oceans (Sverdrup, 1942; Riehl and Malkus, 1958; Bjerknes, 1964; Oort, 1971; Vonder Haar and Oort, 1973; Trenberth, 1979; Held, 2001; Trenberth and Stepaniak, 2004; Czaja and Marshall, 2006). Then, any changes in the spatial pattern of the radiative balance at the top of the atmosphere imply a corresponding change in the PET (Chiang and Bitz, 2005; Enderton and Marshall, 2009; Rose and Ferreira, 2012; Knietzsch et al., 2015; Shaw and Smith, 2022; Pearce and Bodas-Salcedo, 2023).

In a recent study, Needham and Randall (2023, hereafter NR23) showed that a large ensemble of historical climate simulations (the CESM2-LE; Rodgers et al., 2021) performed with the second version of the Community Earth System Model (CESM2; Danabasoglu et al., 2020) produced a large positive (i.e., northward) anomaly in the total PET over a large range of latitudes, primarily between 30°S and 60°N. They found a similar anomaly in the PET calculated from ERA5 atmospheric reanalysis (Hersbach et al., 2020) with a magnitude somewhat smaller than the ensemble mean from the CESM2-LE but still within the ensemble spread. Their further analysis of the CESM2 single-forcing large ensemble (Simpson et al., 2023) led NR23 to conclude that the anomaly was primarily driven by anthropogenic aerosol emissions, which cooled the northern hemisphere relative to the southern and induced anomalous northward heat transport in both the atmosphere and oceans. Similar energetic changes in response to aerosol forcing have been found in atmosphere/mixed layer-ocean GCM simulations (Ming and Ramaswamy, 2011), in CMIP3- and CMIP5-generation models (Hwang et al., 2013; Irving et al., 2019; Lembo et al., 2019, and references therein) as well as in a different CMIP6-generation model (Yukimoto et al., 2022).

These types of energetic changes are known to impact various aspect of the climate system. For example, as a part of the broader body of literature on the energetic theory (Chiang and

Bitz, 2005; Kang et al., 2008; Marshall et al., 2013; Frierson et al., 2013; Schneider et al., 2014; Adam et al., 2016; Donohoe and Voigt, 2017; Kang, 2020; Yukimoto et al., 2022) of the position of the Inter-tropical convergence zone (ITCZ), Hwang et al. (2013) analyzed the southward shift of the ITCZ during the latter half of the twentieth century in response to aerosol forcing in the Northern Hemisphere. They proposed a mechanism where an anomalous Hadley circulation was induced that increased the cross-equatorial heat transport in order to balance the aerosol cooling of the Northern hemisphere.

In this study, we build on the analysis of NR23 to answer the immediate question of how modeled fluid flows in the CESM2-LE changed in the oceans and atmosphere to accomplish the anomalous heat transport indicated by the TOA energy balance. Additionally, we use this energetic framework to uncover a novel example of a change in a single CESM2-SF sub-ensemble which does not extend to the simulations forced by all inputs: we find that the change in atmospheric heat transport *due only to greenhouse gases* leads to a shift in the ITCZ which further analysis indicates is absent from the full CESM2-LE. We also hope this study demonstrates that this type of unified energetic framework is an efficient way to generate testable hypotheses on how some forcing may impact various aspects of the climate system.

4.2 Methods

4.2.1 Data

As in NR23, we primarily analyze the historical (1850-2014) simulations of the CESM2 large ensemble (Rodgers et al., 2021), which includes 100 ensemble members driven by the same anthropogenic aerosol, greenhouse gas, and other forcing datasets used in the Coupled Model Inter-comparison Project Phase 6 (CMIP6, Eyring et al., 2016). The exception is for biomass burning (BMB): 50 of the ensemble members use the CMIP6 BMB forcing dataset, while the remaining 50 members use a smoothed BMB forcing dataset. The smoothed dataset is used to avoid the discontinuity in the CMIP6 BMB field associated with including satellite monitoring of wildfires (1997-2014; Fasullo et al., 2022). Therefore the analysis that follows uses the

50 ensemble members with smoothed BMB forcing, unless otherwise noted. Additionally, we analyze output from the CESM2 single-forcing large ensemble (CESM2-Sf Simpson et al., 2023) which is described in full in section 4.3. Lastly, we briefly analyze a long 2000 year pre-industrial control simulation (Danabasoglu et al., 2020) performed with CESM2 for the purpose of investigating the link between ENSO variability and heat transport anomalies in the Indo-Pacific in the absence of changes in external forcings.

Primary post-processing of model outputs was performed using Python with extensive use of the xarray package (Hoyer and Hamman, 2017) for calculations utilizing data from netCDF files. Additionally, TempestExtremes v2.1 (Ullrich et al., 2021) was used to identify trajectories of extratropical cyclones in section 4.5.

4.2.2 Calculation of Poleward Energy Transport

We use the same oceanic heat transport fields as NR23: the CESM2 monthly mean ocean model field “N_HEAT" is read directly from model output files to retrieve the global zonally integrated ocean heat transport, and the zonally integrated ocean heat transport in the Atlantic basin. The Indo-Pacific heat transport is then calculated as the difference between the total and Atlantic heat transports at each latitude. The separation between ocean basins becomes ambiguous south of the African continent, so Atlantic and Indo-Pacific heat transports are only shown north of 35°S.

The method used to calculate the atmospheric heat transports, however, is different than that used by NR23. NR23 used an energetic method to calculate the atmospheric heat transport from a polar-cap integral of the net TOA minus surface energy balance. This method relied on the assumption of no long-term heat uptake in the atmosphere, which was deemed to be valid on timescales longer than a year. However this effectively lowered the temporal resolution and only allowed for analysis of the annual mean atmospheric heat transport for any given simulation.

To analyze seasonal rather than annual means, and to decompose the heat transport into contributions from the mean meridional circulation (MMC) and from eddies, we require heat transport on monthly timescales. Therefore, we analyze the atmospheric heat transport in the CESM2 large ensemble calculated using the dynamic method described in Cox et al. (2022), alongside calculations of the atmospheric overturning streamfunction.

With the dynamic method, the atmospheric heat transport is calculated by vertically integrating the meridional advection of moist static energy (MSE, i.e., vh for $h = c_p T + gz + L_v q$) at each model grid point and for each timestep. This method also allows for the explicit separation of the MSE transport into contributions from the mean meridional circulation and from eddies. For further discussion on the difference between the energetic and dynamic methods, see Armour et al. (2019).

As in NR23, heat transport anomalies are defined so that a positive value indicates anomalous northward transport.

4.3 Attribution of Heat Transport Changes

NR23 attributed the anomaly in the *total* poleward energy transport entirely to anthropogenic aerosol forcing. Is the same true for the oceanic and atmospheric components of the energy transport? To answer this question, we analyze simulations from the CESM2 single-forcing large ensemble (Simpson et al., 2023) using atmospheric and oceanic heat transport fields which were originally calculated by NR23. Briefly, these simulations were performed with all forcings held fixed at pre-industrial levels except for the forcing of interest (e.g., greenhouse gases) which was allowed to evolve in time. The forcings are greenhouse gases (hereafter GHG2; 15 members), anthropogenic aerosols (AAER2; 20 members), biomass burning (BMB2; 15 members), and everything else (EE2; 15 members). An additional “all-but-aerosol" subensemble (xAER2; 10 members) was performed in which all forcings were allowed to evolve in time *except* for the aerosol forcing, which was fixed at pre-industrial levels. This configura-

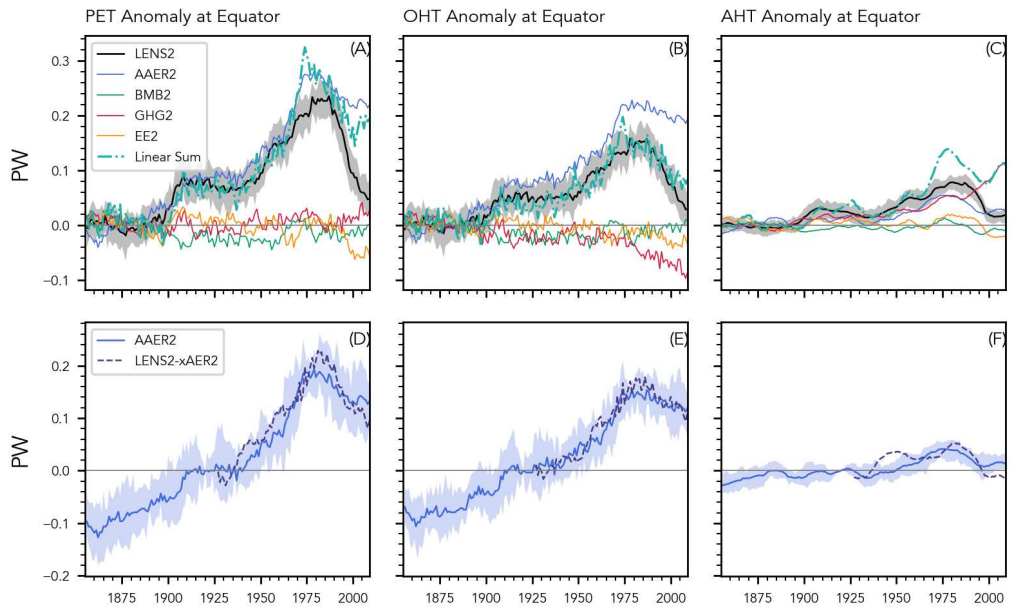

Figure 4.1: Top Row: Anomaly in poleward energy transport at the equator from the CESM2-LE and CESM2-SF sub-ensembles, alongside the linear sum from the CESM2-SF sub-ensemble means (dashed line, composed of the sum of the AAER2, BMB2, EE2, and GHG2 sub-ensemble means). Panels **B** and **C** show the oceanic and atmospheric components, respectively, which add together to give the total PET anomaly in Panel **A**. Bottom Row: as in the top row, but for the CESM2-SF "only-aerosol" and "all-but-aerosol" sub-ensembles (AAER2 and LENS2 minus xAER2, respectively). The shading indicates the inter-quartile range among ensemble members.

tion is similar to the configuration of the original CESM1 single-forcing large ensemble (Deser et al., 2020), which utilized this "all-but-one" approach for each of the forcings.

Panels A-C of Fig. 4.1 show the total, oceanic, and atmospheric heat transport anomaly at the equator for the CESM2-LE (black curve) and for the sub-ensemble means from CESM2-SF. At first glance, panels B and C would appear to *refute* the claim that aerosols are the primary driver of both OHT and AHT contributions to the PET. Specifically, we see that the anomaly in the cross-equatorial AHT and OHT due to greenhouse gases (GHG2; red curve) is very similar to the curve for the cross-equatorial AHT anomaly due to aerosols (AAER2; blue curve). This indicates that greenhouse gas forcing leads to an anomaly in both the oceanic and atmospheric components in the GHG2 simulations.

However, these plots require careful consideration to be interpreted correctly: a key conclusion of Simpson et al. (2023) is that the "only-one" experimental setup the AAER2 simulations

leads to different results in quantifying the impact of aerosols on CESM2 compared to the “all-but-one" approach (i.e., the xAER2 simulations). The plots in the top row of Fig. 4.1 indicate that a similar dynamic occurs with the GHG-only simulations which, to our knowledge, has not been previously discussed in the literature.

To explain this dynamic we first note that the red curve in panel A is largely flat which indicates essentially no change in the total poleward energy transport in the GHG2 simulations. This is unsurprising as theory (Stone, 1978) indicates that the total PET can only be altered from changes in the meridional gradient of the TOA radiative flux. Historic anthropogenic aerosol forcing was primarily confined to the region between 30°N-60°N, although during the twenty-first century aerosol emissions have primarily shifted to East and South Asia (Hoesly et al., 2018). This contrasts with greenhouse gases, which are known to be well-mixed within the atmosphere. Consequently, the direct radiative effect of greenhouse gases cannot lead to a large hemispheric asymmetry in the TOA radiative flux, as is found from the anthropogenic aerosol forcing. It is still conceivable that some *forced response* to greenhouse gases could impact the hemispheric energy gradient, although from Fig. 4.1 A this does not appear to be the case in the GHG2 simulations.

Second, we note also that the linear sum (dashed line in panels A-C) of the sub-ensemble mean heat transport from the GHG2, BMB2, EE2, and AAER2 simulations diverges from the LENS2 heat transport due to the atmospheric component in panel C. This finding is the key point of this discussion as it indicates that the linear combination of the isolated effects of the individual CESM2-SF sub-ensembles cannot explain changes in AHT ca. 1975. Furthermore, it is then impossible to attribute the discrepancy in the AHT anomaly to a particular forcing without additional analysis: there must be an important non-linear process contributing to the AHT anomaly.

We can investigate (and ultimately reject) one possibility, which is that the same aerosol-cryosphere-albedo feedback discussed by Simpson et al. (2023) may be the cause of this non-linearity in the AHT response. However this cannot be the case, as shown in the bottom panels

of Fig. 4.1. These panels demonstrate that the simulations in which only the aerosol forcing evolves in time (AAER2) and the simulations in which all forcings *except* the aerosol forcing evolve in time (xAER2) agree on the change in the PET, OHT, and AHT at the equator relative to the baseline period starting in 1920. Therefore, the non-linearity seen in panel C cannot be the result of the aerosol component of the forcing. Instead, the larger value for the AHT anomaly from the linear sum of CESM2-SF simulations (grey line in panel C) compared to the full CESM2-LE ensemble mean (black line) appears to be primarily due to the GHG sub-ensemble.

With this result in mind, we can now demonstrate a first example of how to utilize changes in the PET to generate hypotheses about how the model responded to changes in external forcings. To begin this process, we note that the cross-equatorial AHT is known to be strongly tied to the position of the ITCZ, as discussed in the introduction. Theory predicts that a relative cooling of the northern hemisphere relative to the southern will tend to shift the mean position of the ITCZ southward. The changes in cross-equatorial AHT in Fig. 4.1 C would then suggest changes in the position of the ITCZ in these various simulations. This can be seen in panel A of Fig. 4.2 for the CESM2-LE and for the CESM2-SF sub-ensembles. Here, we have identified the annual mean position of the ITCZ as the annual mean latitude of the zonal-mean precipitation maximum. Similar to Fig. 4.1, the linear sum of the sub-ensemble mean ITCZ position (dashed line in panel B) diverges from the LENS2 ensemble mean towards the end of the historical period. From panel C of Fig. 4.2 we find that this cannot be due to the aerosol forcing, as the AAER2 and xAER2 simulations are in agreement, similar to panels D-F of Fig. 4.1.

The combination of Figs. 4.1 and 4.2 act as an effective vantage point from which to diagnose the ways in which various phenomena in CESM2 respond to the different forcing configurations. We will first consider the GHG2 simulations and note again that the total PET (red curve in Fig. 4.1 A) is flat, which indicates no change in the inter-hemispheric energy gradient. The OHT on the other hand is negative, consistent with a weakened AMOC in these simulations as described by Simpson et al. (2023). By construction, the difference in PET and OHT must equal

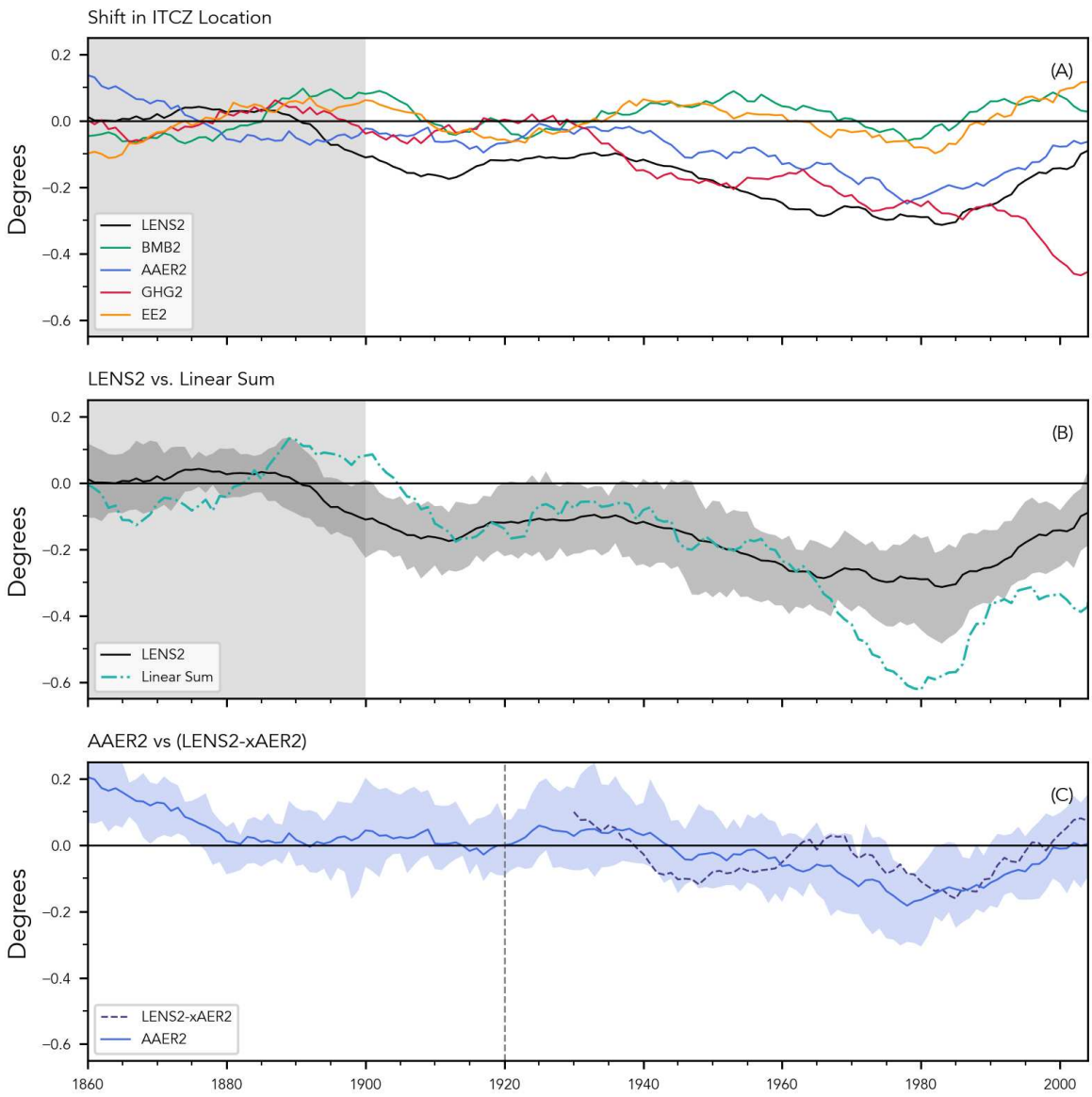

Figure 4.2: Panel A) Shift in the annual mean position of the ITCZ (defined as the annual mean of the monthly mean maximum of the zonal mean precipitation rate) for the CESM2-LE and for the sub-ensembles of the CESM2-SF project. **Panel B)** as in **A** but comparing the CESM2-LE (with shading showing the inter-quartile range among the 50 ensemble members) to the linear sum of the sub-ensemble means from the CESM2-SF project (dashed line). **Panel C** as in **A** but comparing the influence of anthropogenic aerosols on the ITCZ position based on the CESM2-SF “only-aerosol" and “all-but-aerosol" sub-ensembles. Note that the influence of aerosols using the xAER2 simulations is found by subtracting the xAER2 ensemble members from the LENS2 ensemble mean

.

the AHT: we then observe that the AHT change is of the opposite sign, and we have linked this positive anomaly to the southward shift in the ITCZ in Fig. 4.2. Taken together this suggests a

mechanism in the GHG2 simulations where greenhouse warming *in the absence of other forcings* leads to a slowdown of the AMOC (likely due to freshwater runoff from Greenland) with a corresponding southward shift of the ITCZ to ensure energetic balance (e.g., Chiang and Bitz, 2005).

To our knowledge this is the first identification of a nonlinear response of CESM2 to greenhouse gas forcing analagous to the nonlinear response to aerosol forcing described by Simpson et al. (2023). It is possible that this is due to the strongly non-linear behavior of the AMOC in CESM2 as described by Simpson et al. (2023), and in a recent study by Needham et al. (2024b). Unfortunately, this point is difficult to investigate further due to the lack of an “all-but-GHG" set of simulations in the CESM2-SF. This topic clearly warrants further investigation, but is outside the scope of the current study. For our purposes here, it is enough to conclude that the *apparent* influence of GHGs on OHT and AHT (e.g., the red curves in Fig. 4.1) is limited to the GHG-only simulations of the CESM2-SF large ensemble, and does not extend to the full CESM2-LE simulations.

Contrast this with what is seen in the AAER2 simulations: the PET anomaly in this case is certainly not flat, and both the OHT and AHT anomalies are positive. Then, this indicates thhat the AMOC strengthens rather than weakens, while the ITCZ still shifts southward. In short, the ITCZ and AMOC here work together to balance a third factor - namely a northern hemisphere cooling due to a change in the aerosol forcing. As we shall see, the behavior of the full CESM2-LE simulations much more closely follows that of the AAER2 simulations, with a series of distinct phenomena working *together* to balance the aerosol cooling. We will briefly return to the CESM2 single-forcing simulations in a later section as part of our discussion of changes in extratropical cyclones in response to aerosol forcing. However the remainder of this study will be primarily focused on changes in the full CESM2 large ensemble.

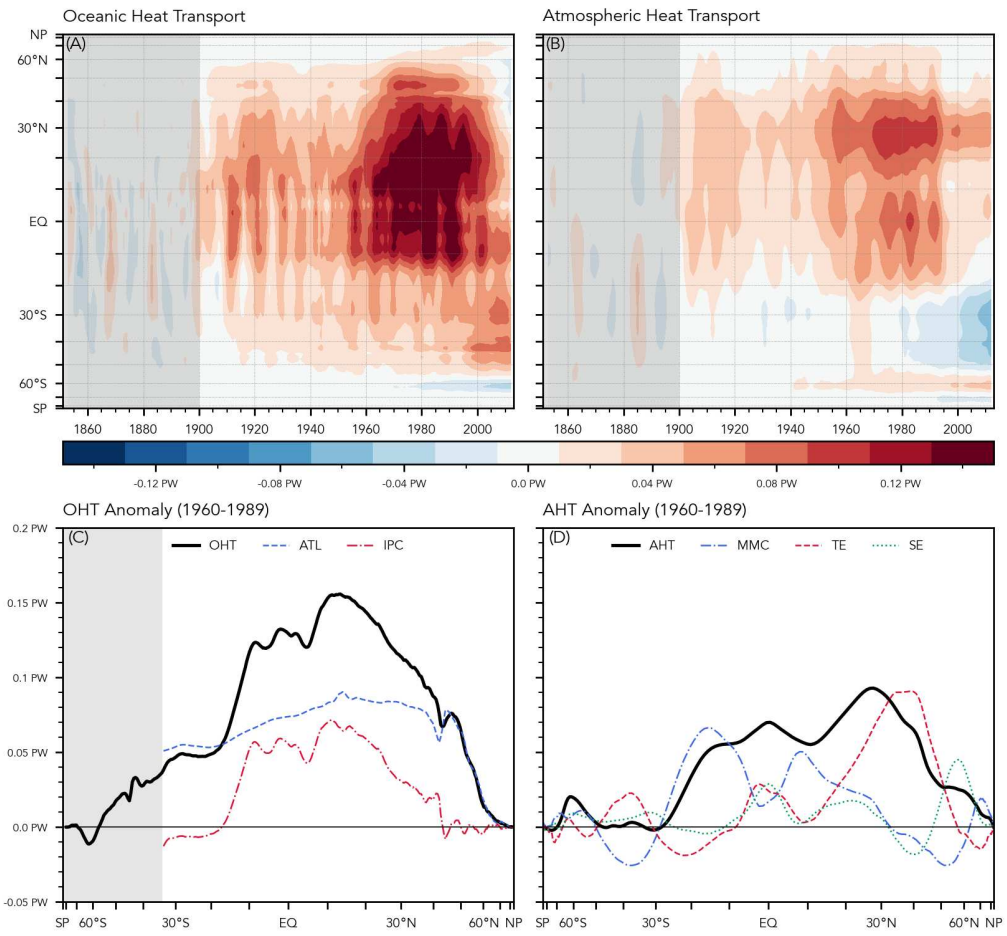

Figure 4.3: Top Row: Anomaly in poleward energy transport by the oceans **(A)** and by the atmosphere **(B)** relative to the 1851-1900 baseline. **Panel C:** Decomposition of total OHT (black) into contributions by the Atlantic (blue, dashed) and Indo-Pacific (red, dash-dotted) basins. **Panel D:** Decomposition of total AHT (black) into contributions from the mean meridional circulation (blue, dash-dotted), transient eddies (red, dashed), and stationary eddies (green, dotted).

4.4 Characterization of Atmospheric and Oceanic heat transport anomaly

Figure 4.3 shows the ensemble mean anomaly in the poleward energy transport (northward positive) relative to the 1851-1900 baseline. The top panels are similar to Fig. 9 of NR23, but with the color bar scaled to better show the change in the constituent transports rather than the total transport. Both the OHT and AHT anomalies show a characteristic peak in the latter half of the twentieth century that extends across a wide range of latitudes.

The bottom panels of Fig. 4.3 show the time average of this anomaly from 1960 to 1989, with the transports further decomposed into contributions from the Atlantic and Indo-Pacific ocean basins (for OHT), and contributions from the mean meridional circulation (hereafter MMC) and eddies (for AHT). The shading south of 35°S is included to emphasize that the boundary between the Atlantic and Indo-Pacific ocean basins becomes ambiguous south of the African continent. The bottom panels show that the maximum OHT anomaly is about twice as large as the maximum AHT anomaly (approximately 0.15 PW vs. 0.08 PW), with the largest OHT anomaly found from 15°S to 50°N.

The AHT anomaly is between 0.05-0.1 PW from 20°S to 50°N, with the largest values found in the northern midlatitudes. These northern midlatitude values are primarily due to the transient eddy component, while the MMC component dominates in the subtropical regions of both hemispheres. We note that the transient eddy contribution (red curve) is much larger than the contribution from stationary eddies (green curve) in the latitude range of interest. Accordingly, we will omit any further discussion of stationary eddies, and henceforth use the term “eddy" with the understanding that this is primarily due to contributions from sub-monthly transients.

The remainder of this study is devoted to understanding which processes control the anomaly in Atlantic and Indo-Pacific OHT (i.e., the bottom left panel), and the anomaly in MMC and eddy AHT (i.e., the bottom right panel). We begin by analyzing the AHT anomaly due to the MMC.

4.5 Decomposition of Atmospheric Heat Transport

4.5.1 AHT due to the MMC

The atmospheric MMC from about 30°S to 30°N is dominated by the overturning Hadley cells, which have a distinct seasonal cycle. Accordingly, we begin our decomposition by looking at the seasonal cycle in the AHT anomaly due to the MMC, which is shown in Fig. 4.4. We first observe that the DJF season has extremely large positive and negative anomalies from 30°S to

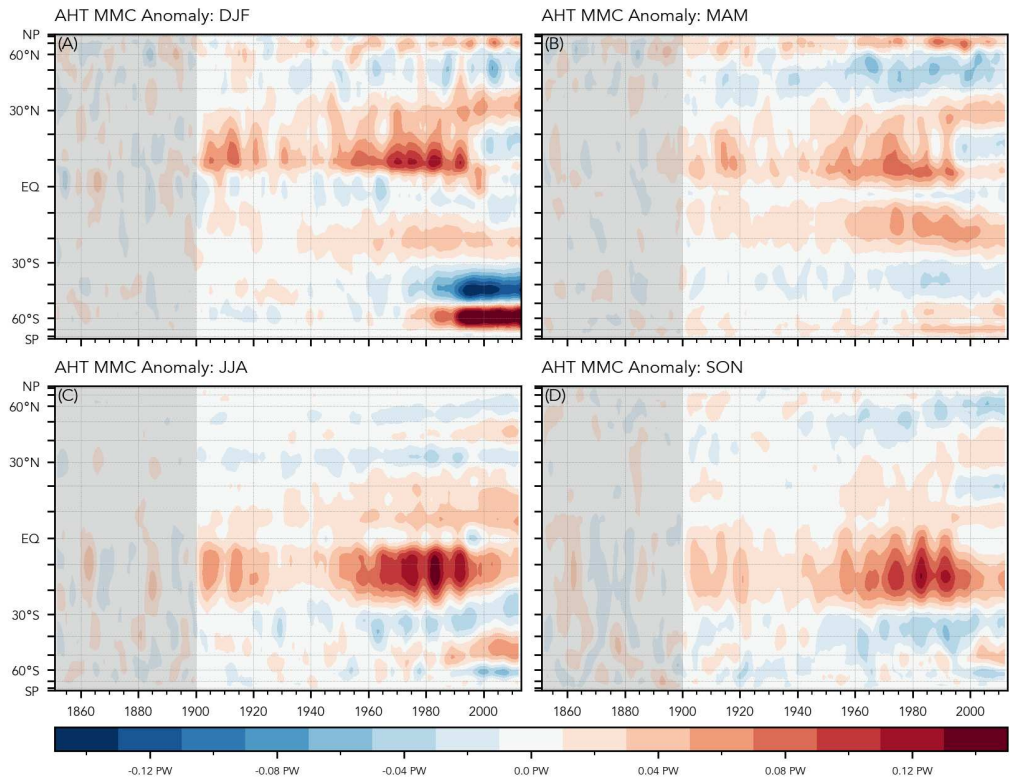

Figure 4.4: Ensemble mean anomaly in AHT due to the mean meridional circulation for each season.

70°S, but note that these have little impact on the total AHT anomaly because of corresponding and opposite changes in the eddy AHT (as seen in panel A of the forthcoming Fig. 4.6).

The MMC AHT anomaly has a clear if somewhat muted seasonality: During MAM and especially DJF there are large positive anomalies in the northern hemisphere from 10°N-30°N. In the southern hemisphere, positive anomalies occur during JJA and SON, with somewhat smaller values during MAM. This seasonality suggests a direct link with the Hadley cells. Essentially the anomalous AHT is accomplished by both cells, and the spatial structure (i.e., whether it occurs in the southern hemisphere, the northern hemisphere, or both) is determined by whether one or both cells is active during a given season.

When we look at the anomaly (1960-1989) in the zonal mean meridional streamfunction (Fig. 4.5) there is a distinct *lack* of seasonality. Instead, we see an anomalous clockwise circulation centered on the equator which changes only slightly with the seasons. This circulation indicates a *southward* cross-equatorial flux of latent energy, and a corresponding northward

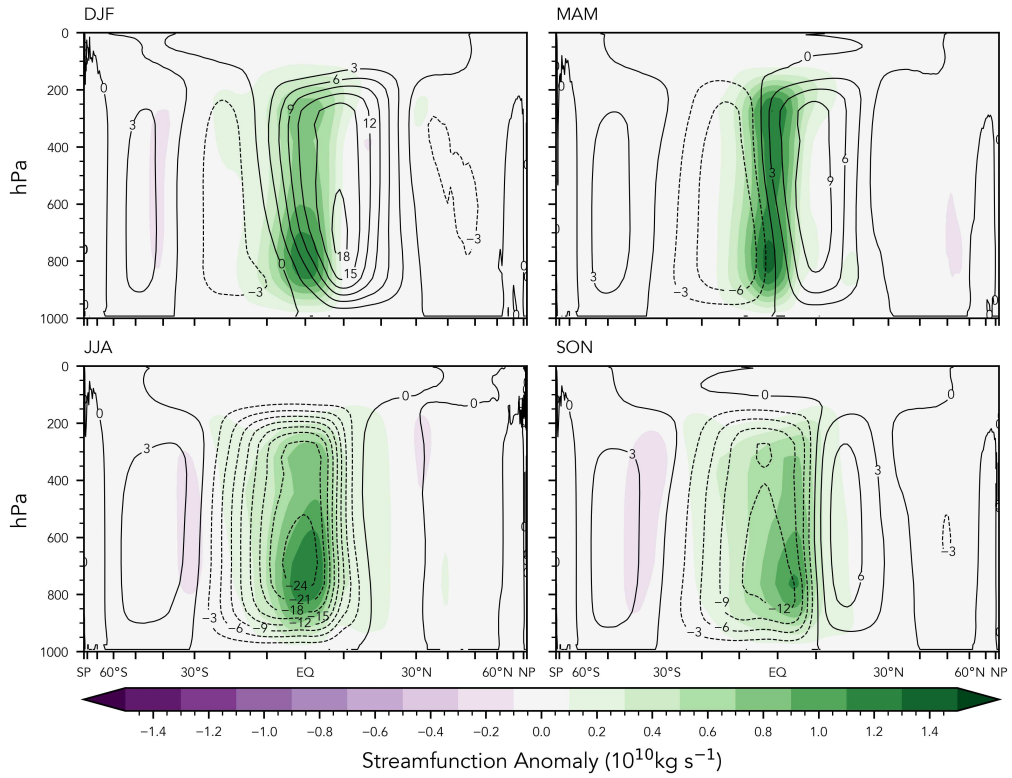

Figure 4.5: Ensemble mean streamfunction anomaly by season (shading) overlaid against ensemble mean streamfunction climatology (contours, 10^{10}kgs^{-1}).

cross-equatorial flux of dry static energy. As this energy transport by the upper-branch is known to be larger than that of the lower branch (Riehl and Malkus, 1958; Neelin and Held, 1987; Needham and Randall, 2021), the net effect is a *northward* cross-equatorial energy flux by the MMC, and a southward shift of the ITCZ, consistent with Fig. 4.2 and with previous studies (Ming and Ramaswamy, 2011; Hwang et al., 2013; Irving et al., 2019; Yukimoto et al., 2022).

4.5.2 Changes in Extratropical Cyclones

We move now to the contribution by eddies to the AHT anomaly (i.e., the red curve in the bottom right panel of Fig. 4.3). The eddy heat transport has a large peak in the northern mid-latitudes with a maximum value of about 0.1PW near 40°N. The seasonal decomposition of the AHT Eddy anomaly (Fig. 4.6) shows large anomalies during all seasons except for JJA, with the largest values in DJF and MAM.

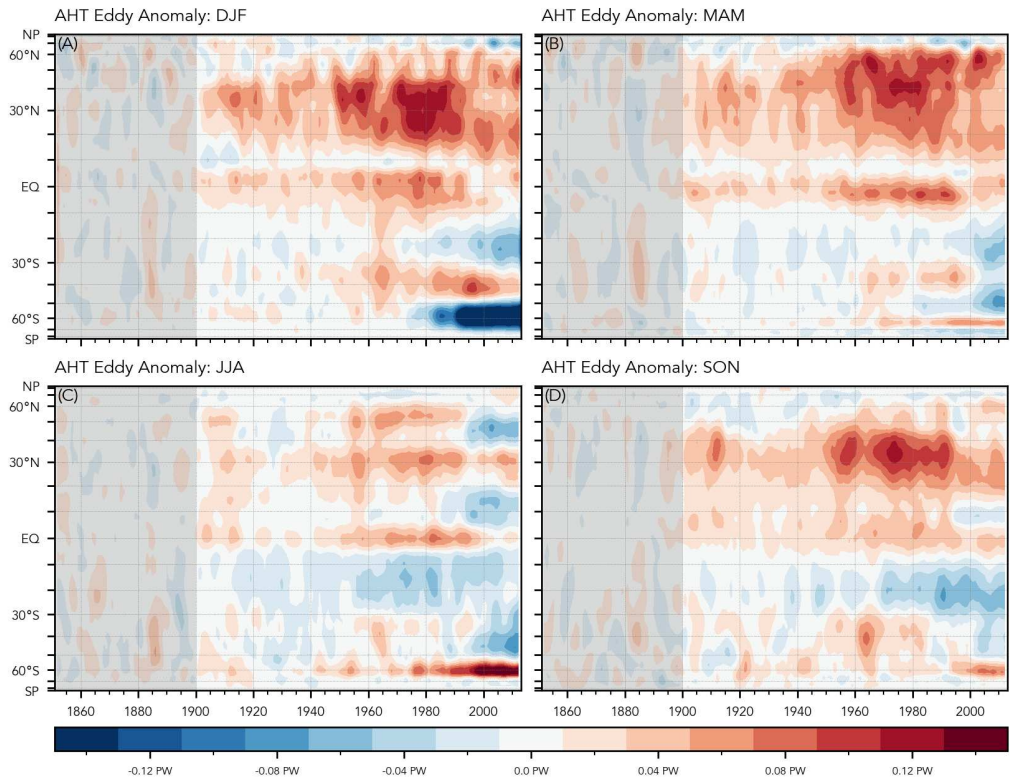

Figure 4.6: As in Fig. 4.4, but for the combination of stationary and transient eddies

The heat transport by eddies is largely accomplished by midlatitude storms in the Atlantic and Pacific storm tracks off the eastern coasts of North America and Japan. These extratropical cyclones (ETCs) grow as a result of atmospheric baroclinicty, and act to weaken that baroclinicty through the poleward transport of energy (Hoskins and Valdes, 1990; Walker et al., 2020). Then, changes in the frequency or intensity of ETCs could explain the change in eddy AHT seen in fig. 4.5.

ETC statistics can be considered from either an Eulerian perspective, in which frequency filtering is used to isolate synoptic-scale variability on roughly 2-6 day timescales; or from a Lagrangian one, in which an algorithm is used to identify each individual ETC within a simulation, from which population statistics may then be calculated. As discussed by Walker et al. (2020), the Eulerian method allows for rapid calculation of ETC statistics, but without any information about the number and/or intensity of storms. For this study we take a Lagrangian approach and consider the bulk effect of aerosol forcing on individual ETCs.

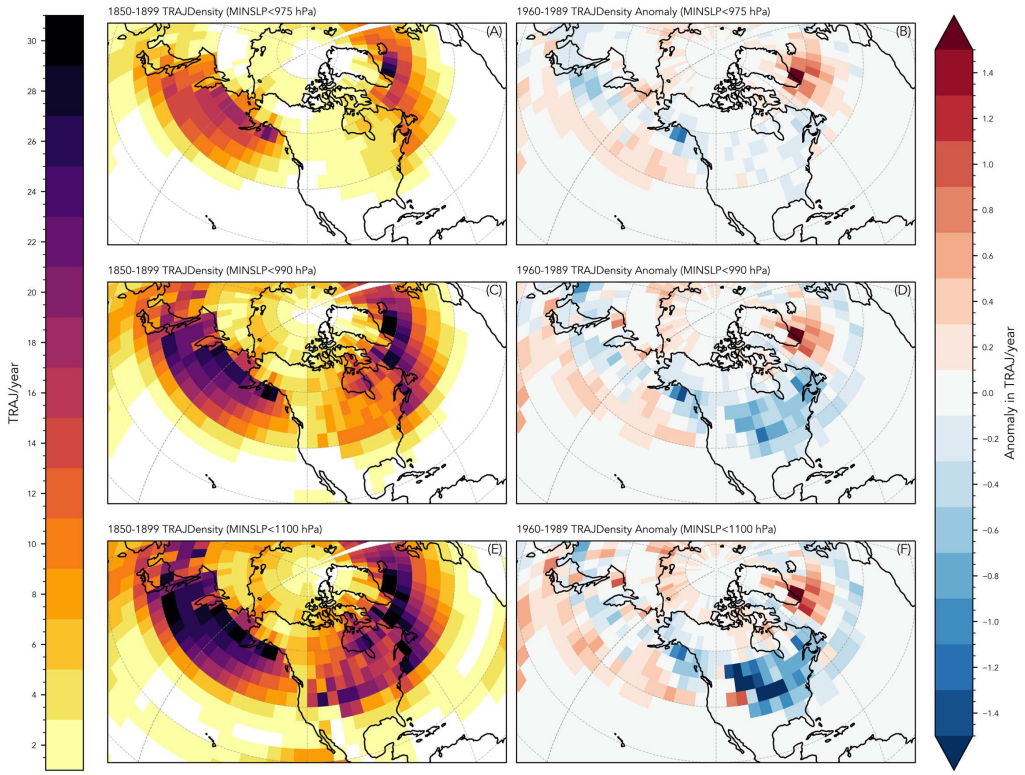

Figure 4.7: Left Column) Ensemble mean climatology (1850-1899) of the count of trajectories per year passing through a 5° grid cell. **Panel A** includes only the most intense storms (defined as the trajectories in which the minimum sea level pressure was below 975 hPa), **Panel C** includes additional strong storms (with a minimum sea level pressure below 990 hPa), while **Panel E** includes all identified ETCs. **Right Column)** as in the **Left Column**, but for the anomaly in the count of ETCs from 1960-1989, relative to the 1850-1899 climatology.

To accomplish this, we utilize the `DetectNodes` and `StitchNodes` algorithms contained within the `TempestExtremesv2.1` collection (Ullrich et al., 2021) to track ETCs in the 6-hourly sea level pressure field in the CESM2-LE simulations. These individual tracks were then mapped onto a 5° by 5° grid by counting the number of trajectories that passed through a particular gridcell during a given month. This process was applied to each of the 100 CESM2-LE simulations (although only the 50 members with smoothed BMB forcing were analyzed), and to each of the 75 CESM2-SF simulations. A full description of the method is included in the supporting information.

This method allows us to investigate the impact of aerosols on both the number and the intensity of ETCs. The left-hand column of Fig. 4.7 shows the ensemble mean climatology of

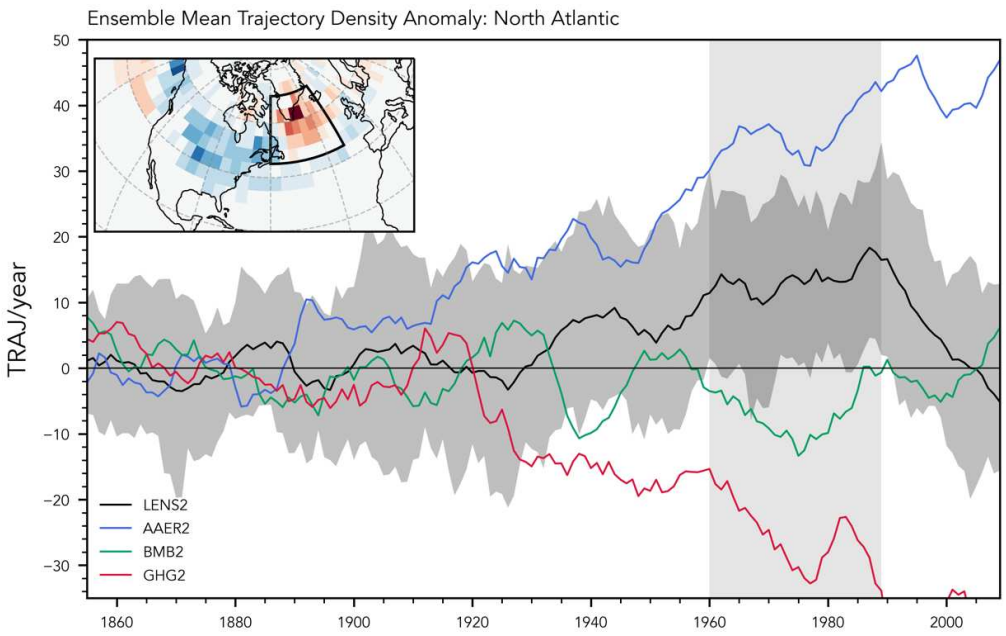

Figure 4.8: Timeseries of the ensemble mean number of storms passing through the north Atlantic (60°W-20°W, 45°N-70°N; see the inset). The black curve shows the LENS2 anomaly (along with the interquartile range in the shading), while the blue, green, and red curves indicate the AAER2, BMB2, and GHG2 sub-ensembles of CESM2-SF.

the number of storms per year which pass through a given gridcell: this demnstrates that this method correctly identifies the canonical (e.g., Hoskins and Valdes, 1990) Atlantic and Pacific storm tracks. Each row in the column excludes all storms above a particular sea level pressure threshold so that Panel A includes only the most intense storms (in which the minimum pressure along a trajectory is less than 975 hPa), while Panel F includes virtually all storms identified by the algorithm. In practice, we are more concerned with the *anomaly* in the count of trajectories during the crucial 1960-1989 period, which is shown in the right-hand column. Here the largest change is immediately seen off of the southern tip of Greenland, where there is a marked increase in the number of the most intense storms. This is accompanied by a decrease in weaker storms over continental north America (panel F). Taken together, these changes indicate a strengthening of the Atlantic storm track that is accompanied by a poleward (and eastward) shift. There also appears to be a somewhat smaller change in the Pacific storm track.

As in Fig. 4.1, we can utilize the ETC track density from the various CESM2-SF sub-ensembles to attribute the anomaly from Fig. 4.7 to the aerosol forcing. Fig. 4.8 shows the smoothed time-series in the number of ETCs that pass through the north Atlantic (here defined as 60°W-20°W, 45°N-70°N). The CESM2-LE anomaly shows the characteristic peak centered around 1975 that is indicative of the aerosol forcing (and is extensively discussed by NR23). In contrast, both the BMB2 and GHG2 ensembles show a negative deviation from climatology during this time period.

4.6 Decomposition of Oceanic Heat Transport

As discussed previously, the OHT anomaly in the bottom-left panel of Fig. 4.3 is decomposed into contributions from the Atlantic, and contributions from the Indo-Pacific. The Atlantic anomaly is larger than the Indo-Pacific anomaly at all latitudes, and is non-negligible from 35°S-60°N. However, the Indo-Pacific OHT anomaly is still large from about 10°S-30°N.

This particular decomposition (i.e., into Atlantic and Indo-Pacific contributions) is by necessity: the model output includes the northward heat transport by the global oceans, and the northward heat transport in the Atlantic basin, with no separate fields for heat transport in the Pacific or Indian ocean basins. This is partly a consequence of geography, as the boundary between the Pacific and Indian oceans is much more porous than the boundary between either of these ocean basins and the Atlantic: consequently, there is significant heat transport between the basins, especially through the Maritime Continent (Cheng et al., 2019; Trenberth and Zhang, 2019).

The canonical understanding of OHT is that it is primarily accomplished by the western boundary currents (e.g., the Gulf Stream or the Kuroshio). This can be seen in the top panel of Fig. 4.9 which shows the vertically integrated northward ocean heat transport calculated directly from the CESM2 ocean model output for the period from 1850-1899. It should be noted that Fig. 4.9 shows OHT data after it has been vertically integrated and then linearly interpolated from the irregular CESM ocean grid to a regular lat-lon grid for visualization purposes. The

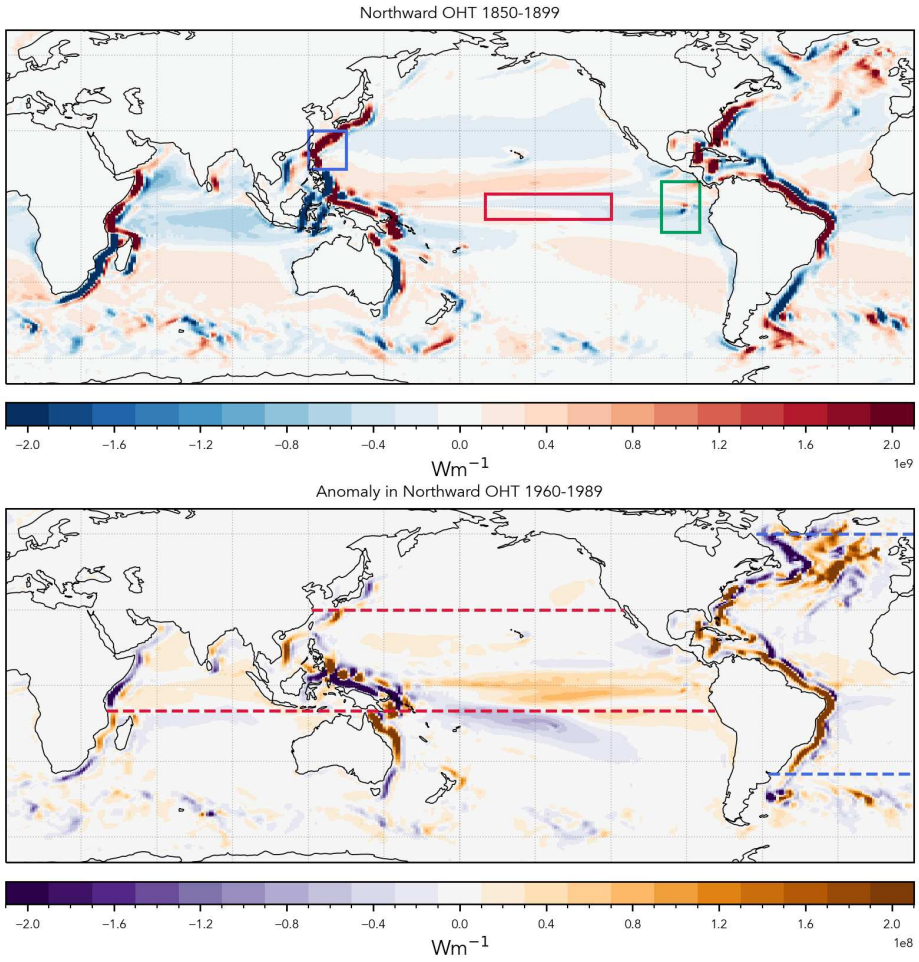

Figure 4.9: Vertical integral of northward energy transport, directly calculated from the CESM2 ocean model. Top: Climatological baseline of OHT from 1850-1899. Bottom: Anomaly from climatology for 1960-1989. Red, blue and green boxes in the top panel are included to illustrate the Niño3.4, Kuroshio, and eastern tropical Pacific regions that will be analyzed later in the text.

errors that accompany this interpolation are non-negligible, so a longitudinal integration of this field (not shown) will slightly deviate from the values shown in Fig. 4.3. Therefore, we use this figure as a tool to identify broad regions that are important for changes in OHT, but do not ascribe high confidence to the particular numerical value at any given point.

With these caveats addressed, the top panel of Fig. 4.9 illustrates that a large amount of energy transport is accomplished along the western boundaries of the major ocean basins - either northward (red colors) or southward (blue colors) - connected to the well-known western boundary currents. The bottom panel shows the anomaly in this ocean transport for 1960-1989

relative to the above baseline. Here, the colors are largest along the east coast of the Americas, in the North Atlantic, and near the Maritime Continent, with slightly smaller values in the interior of the ocean basins, especially the Pacific. The red and blue horizontal dashed lines are included for each basin to show which regions have a non-negligible OHT anomaly in the original heat transport from the CESM2 ocean model, as identified in Fig. 4.3.

4.6.1 OHT in the Atlantic

We begin our discussion of the OHT anomaly in the Atlantic basin. From Fig. 4.9, it is clear that the Atlantic OHT anomaly occurs in a narrow band off the east coast of the Americas, from Brazil to New England. The cross-equatorial nature of this heat transport anomaly immediately suggests a link with the Atlantic Meridional Overturning Circulation (AMOC; Rahmstorf, 2002; Rahmstorf et al., 2015; Thornalley et al., 2018; Caesar et al., 2018, 2021), which modeling studies have shown is particularly sensitive to anthropogenic aerosol forcing (Ma et al., 2020; Menary et al., 2020; Hassan et al., 2021; Robson et al., 2022; Li et al., 2023; Simpson et al., 2023; Needham et al., 2024b).

We probe this link with Fig. 4.10, which shows the time series of the OHT anomaly in different seasons in the Atlantic basin. The bottom left panel shows the seasonal- and annual-mean anomaly in the AMOC, defined as the maximum of the overturning streamfunction in the Atlantic basin below a depth of 500 meters. The seasonal cycle of the AMOC anomaly is primarily due to changes in magnitude, which is consistent with the Atlantic OHT. Indeed, the Atlantic OHT at a variety of latitudes shows a remarkable similarity to the time evolution of the AMOC anomaly (right panel of Fig. 4.10). Correlations between the AMOC anomaly and the Atlantic OHT are extremely high, with the square of the pearson correlation greater than 0.94 at the four latitudes shown in the panel. The interpretation here is simple: an increase in the AMOC in response to aerosol forcing is accompanied by a corresponding increase in the Atlantic OHT.

Analysis of the older CESM1 large ensemble (Kay et al., 2015) indicates that the older CESM1 ensemble does not have a large anomaly in the AMOC in response to historic forcing like that

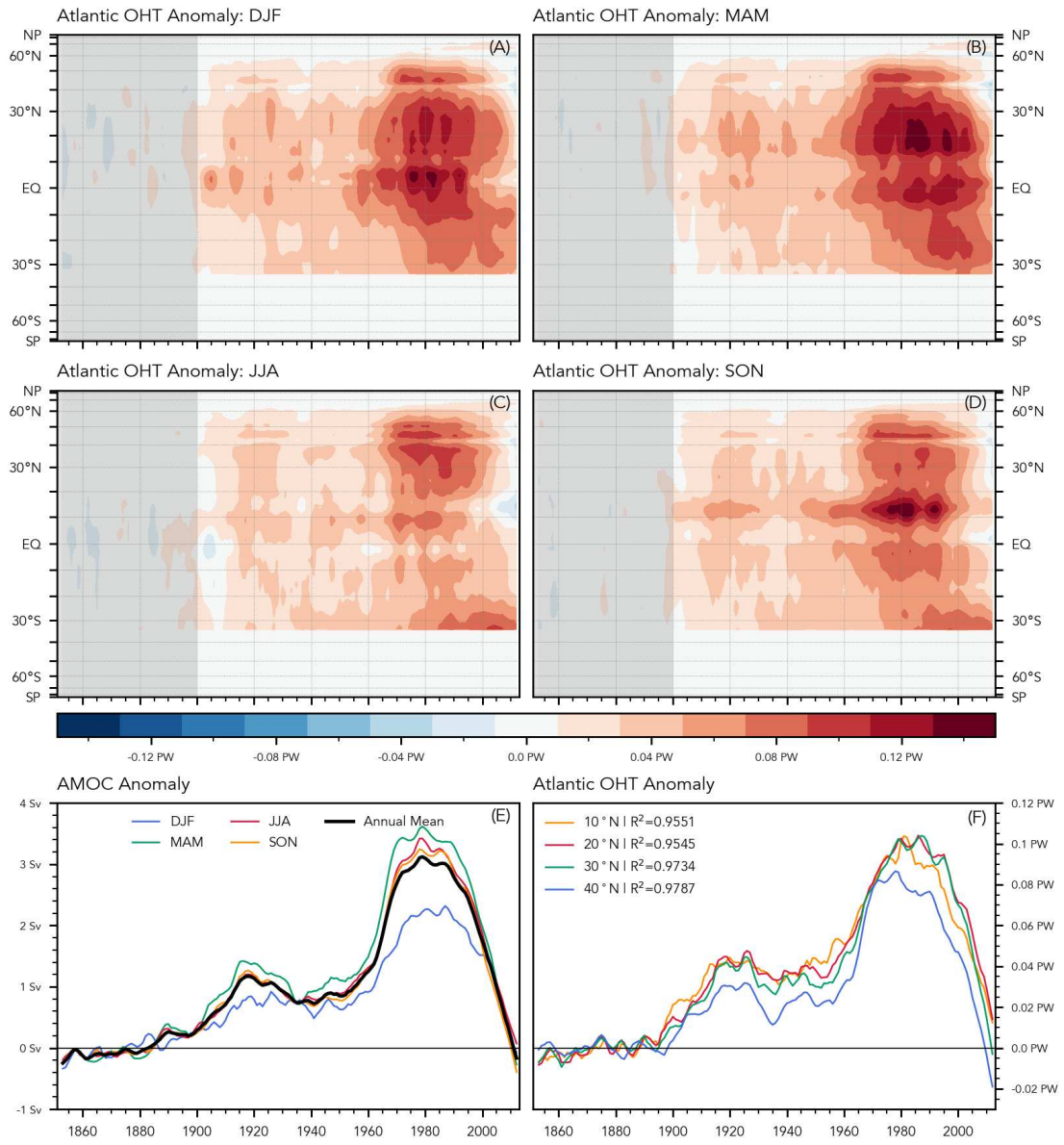

Figure 4.10: Panels A-D) As in Fig. 4.4 but for the heat transport anomaly in the Atlantic. **Panel E)** Ensemble mean anomaly in the Atlantic Meridional Overturning Circulation (AMOC), defined as the maximum of the overturning streamfunction in the Atlantic basin below a depth of 500 m. **Panel F)** Ensemble mean anomaly in Atlantic OHT at a range of latitudes. Correlations in the legend are between the given OHT anomaly and the AMOC anomaly.

seen in CESM2 (See Fig. 9 of Simpson et al., 2023). The older version also lacks the same large anomaly in the ocean heat transport, further supporting the conclusion that the large OHT anomaly in CESM2 is due to changes in the AMOC. This is consistent with recent studies (Menary et al., 2020; Hassan et al., 2021; Robson et al., 2022; Needham et al., 2024b), which

found that many CMIP6 generation models (including CESM2) have a much larger AMOC response than many CMIP5 models (including CESM1), and that the AMOC response in those CMIP6 models is likely inconsistent with observations.

4.6.2 OHT in the Indo-Pacific

The remainder of this section is devoted to addressing the OHT anomaly in the broadly-defined Indo-Pacific region. In contrast to the OHT anomaly in the Atlantic, which we singularly ascribe to changes in the AMOC, we find that the OHT anomaly in the Indo-Pacific is due to changes in several regions due to two distinct mechanisms.

As discussed previously, the top panel of Fig. 4.9 indicates that the primary OHT occurs along the western boundary of the ocean basins. However, the anomaly in the OHT from 1960-1989 (bottom panel of Fig. 4.9) occurs both along the western boundaries *and* in the interior of the ocean basins, with the largest of these “interior anomalies" occurring in the equatorial Pacific. This is a surprising result, as the shading in the top panel would suggest that changes in the ocean interior would likely be small compared to changes along the western boundaries. However, small changes spread over a wide area can lead to large changes in the *zonal integral* of the heat transport (i.e., Fig. 4.3), which is the quantity of interest in this study. Accordingly, we now look at the factors that could have altered the heat transport in the interior of the Pacific.

OHT in the Pacific Interior and Links to ENSO

The OHT anomaly in the central and eastern Pacific (i.e., the bottom panel of Fig. 4.9) is located across a wide range of longitudes but is within a narrow band of latitudes that are close to the equator. This spatial structure leads us to the hypothesis that this anomaly is in some way related to the El Niño-Southern Oscillation (ENSO; Trenberth, 1997). We investigate this guess in the top panel of Fig. 4.11, which shows the anomalous OHT in the Indo-Pacific region during different phases of ENSO. The ENSO phase was determined using the 5-month average SST anomaly in the Niño3.4 box (5°S-5°N, 120°W-170°W, shown as the red box in the top panel

of Fig. 4.9, equivalent to the observational Oceanic Niño Index, ONI) relative to the period of 1921-1970.

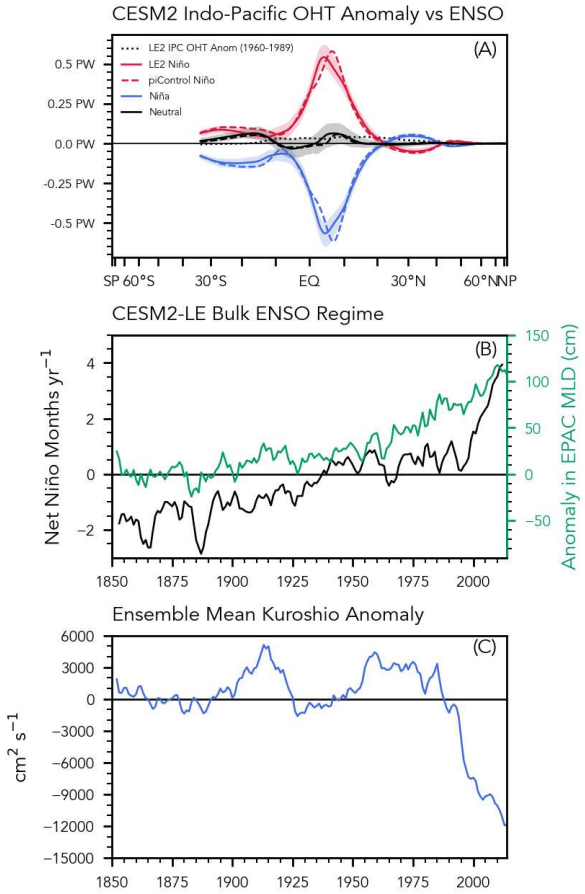

Figure 4.11: Panel A) Composite analysis showing the anomalous ocean heat transport in the Indo-Pacific region during different phases of ENSO for the CESM2 Large Ensemble (solid lines) and for the CESM2 pre-industrial control simulation (dashed lines). Shading shows the model spread, quantified as the 5^{th} to 95^{th} percentile among ensemble members. Also shown is the heat transport anomaly in the Indo-Pacific from 1960-1989, which is identical to the corresponding curve in the bottom-left panel of Fig. 4.3. **Panel B)** Time series of two metrics used to quantify changes in the ensemble mean ENSO regime in the CESM2 large ensemble. The black curve shows the ensemble average number of El Niño minus La Niña months for each year, while the green curve shows the anomaly in the depth of the mixed layer (positive indicating a deeper mixed layer) in the eastern tropical pacific. **Panel C)** Time series of the ensemble mean anomaly of the strength of the Kuroshio current (defined as the average vertically integrated ocean velocity from 120°E-135E, 15°N-30°N)

During El Niño months (SST anomaly ≥ 0.5K) the OHT is anomalously positive in the Indo-Pacific, reaching an ensemble mean value of greater than half a petawatt between 5°N-10°N.

During La Niña months (SST anomaly ≤ -0.5K) the OHT anomaly is nearly the perfect inverse of the El Niño anomaly, with large negative values in excess of -0.5 PW, and during neutral months (-0.5K ≤ SST anomaly ≤ 0.5) the OHT anomaly is much smaller. This relationship between the Indo-Pacific OHT anomaly and ENSO phase occurs both in the ensemble mean of the CESM2 large ensemble (solid lines) and in a 2000 year long pre-industrial control simulation (dashed lines) performed with CESM2 (Danabasoglu et al., 2020), which indicates that the relationship between OHT and ENSO holds in the absence of changes to external forcings.

Importantly, the magnitude of the OHT anomaly during El Niño and La Niña months is much larger than the 1960-1989 anomaly in the OHT (bottom left panel of Fig. 4.3 and dotted black line in the top panel of Fig. 4.11). As a primary characteristic of ENSO is a shift in the heat content of the eastern Pacific, this analysis suggests that a relatively small increase in the time-averaged depth of the eastern Pacific mixed layer (whether through an increase in El Niño-like conditions, or through a long-term warming trend due to GHGs) could lead to a large enough increase in the OHT to explain the anomaly seen in Fig. 4.3. Put another way, the increase in the depth of the time-averaged mixed layer could be much smaller than is seen during a typical El Niño event and still account for the anomaly in the OHT.

The middle panel of Fig. 4.11 shows two metrics that quantify the long-term behavior of the eastern Pacific; both of which show that the ensemble mean becomes more “Niño-like" over the course of the historical simulations. The first measure is the ensemble mean number of El Niño minus La Niña months per year. This was calculated by first calculating the ONI time series to define Niño and Niña months for each simulation. For a particular year in a given simulation, the number of months that qualified as La Niña were subtracted from the number of months that qualified as El Niño, and then this count was averaged across ensemble members for a given year. In the first decades of the historical period there tend to be more La Niña than El Niño months, but over the course of the historical period there is a general trend towards a regime that favors El Niño, especially by the end of the simulation, with a “cross-over" point near the middle of the twentieth century.

The second measure is the anomaly of the depth of the mixed layer in the far eastern equatorial pacific (averaged over the region bounded by 100°W, 85°W, 10°S, and 10°N, shown as the green box in the top panel of Fig. 4.9). The mixed layer becomes deeper by about a meter from 1850 to 2014 which is also consistent with a “Niño-like" regime as a deeper mixed layer indicates a larger heat content in the eastern tropical Pacific. For the analysis that follows we will use the mixed layer depth anomaly as our measure of the underlying ENSO regime because it has less high frequency variability than the Niño minus Niña metric, which appears to be more sensitive to short-term forcing from things like Volcanoes (e.g., the large negative spike which immediately follows the large eruption of Krakatau in 1883). The trend towards a more “Niño-like" regime can explain part of the increase in Indo-Pacific OHT over the historical simulations, but crucially it cannot explain the precipitous decline in the OHT anomaly near the end of the twentieth century (shown in Fig. 4.3 and in the black curves of Fig. 4.12). This suggests that the OHT anomaly in the Indo-Pacific is also driven by some process in addition to ENSO.

To investigate this further we return to the top panel of Fig. 4.9 and again note that a large fraction of the OHT occurs in the western boundary currents and make a second educated guess that changes in the Pacific western boundary current may be important in determining the OHT anomaly. In the Indo-Pacific, the heat transport poleward of about 15°N it is primarily in the westward flank of the Pacific subtropical gyre: that is, in what becomes the Kuroshio current.

OHT in the Pacific Driven by ENSO and Kuroshio Variability

The bottom panel of Fig. 4.11 shows the ensemble mean anomaly in the strength of the Kuroshio. This was calculated as the average of the vertically integrated meridional ocean velocity in the region bounded by 120°E, 135°E, 15°N, and 30°N, shown as the blue box in the top panel of Fig. 4.9. The ensemble mean Kuroshio strength shows sensitivity to the large aerosol pulses, first in the early 1900s and then in the latter half of the twentieth century (Hoesly et al., 2018). Crucially, the anomaly becomes strongly negative in the final decade of the twentieth century and into the twenty-first, which likely accounts for the reduction in the OHT anomaly in the Indo-Pacific.

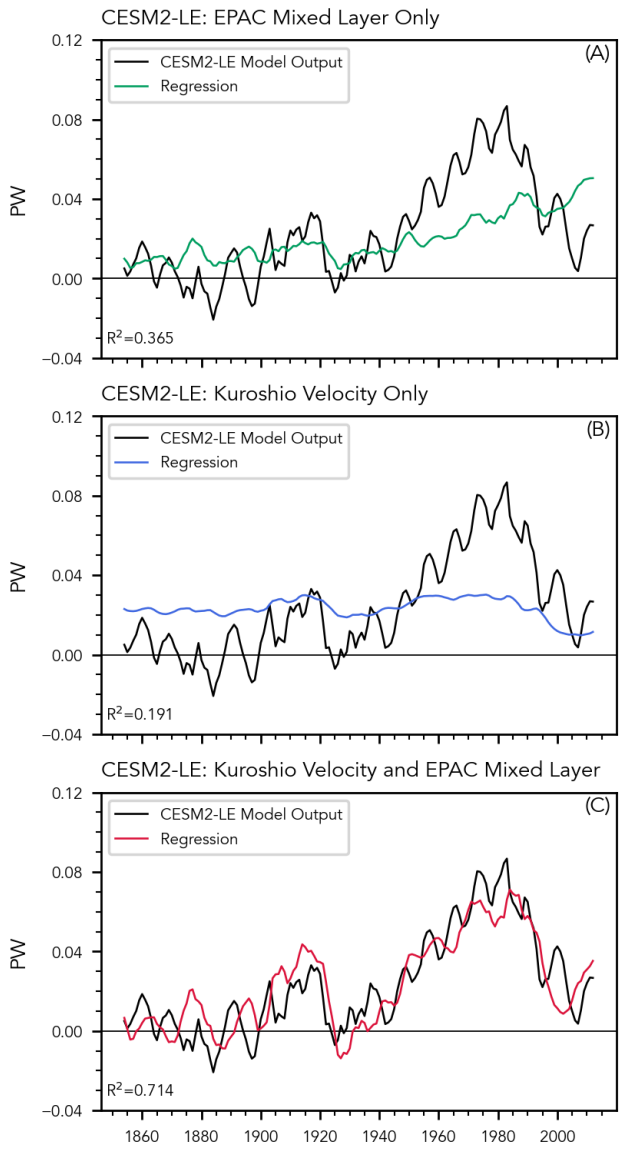

Figure 4.12: Comparison of the average heat transport anomaly from 10°S-30°N in the Indo-Pacific (black curve) and the value predicted by a linear regression against **(A)** the mixed layer depth anomaly in the eastern pacific; **(B)** the Kuroshio strength anomaly; and **(C)** against both the mixed layer depth and the Kuroshio anomalies.

As a test of our hypothesis that the underlying ENSO regime and the strength of the Kuroshio *together* explain the Indo-Pacific OHT, we perform a multiple linear regression of the form

$$Y_{OHT} = \beta_{MXL} X_{MXL} + \beta_{KUR} X_{KUR} + \alpha, \tag{4.1}$$

where the “prediction" Y_{OHT} is the area-weighted average OHT anomaly in the Indo-Pacific between 10°S and 30°N; the first predictor X_{MXL} is the anomaly in the depth of the mixed layer in the extreme eastern tropical Pacific (i.e., the green curve in the middle panel of Fig. 4.11); the second predictor X_{KUR} is the anomaly in the strength of the Kuroshio (i.e., the blue curve in the bottom panel of Fig. 4.11); β_{MXL} and β_{KUR} are regression coefficients (i.e., slope), and α is the intercept.

In contrast to earlier analysis, this multiple linear regression was performed using all 100 ensemble members. When only the 50 members with smoothed BMB forcing were used, a 40/10 split of ensemble members into training and testing groups led to too much noise in the ensemble mean of only 10 members. We performed this analysis using only the 50 members with smoothed BMB forcing as well as with only the 50 members with the original CMIP6 forcing and found no discernible difference between the sets. This allows us to be confident that the results of the multiple linear regression are not due to a difference in the response to BMB forcing, but simply require a sample size larger than 50 members to isolate the forced response from internal variability.

To prevent over-fitting, which is an important consideration even for a linear model, we randomly divided our 100 ensemble members into two groups, with 80 members (the training set) used to generate regression coefficients and the final 20 members (the testing set) used for evaluation of the model fit. Given our training and testing sets, we then took a bootstrapping approach where 5000 random subsets of 20 training set ensemble members were used to generate a set of regression coefficients and an intercept. Finally, the average regression coefficients and intercept were used with the testing set to “predict" the ocean heat transport anomaly from the anomalies in the eastern Pacific mixed layer depth and the Kuroshio strength.

This “prediction" using the testing set mixed layer depth and Kuroshio strength is shown as the red curve in the bottom panel of Fig. 4.12 against the testing set ensemble mean OHT anomaly. The linear model largely recreates the low-frequency behavior of the OHT anomaly (R^2=0.714) with a first peak in the early 1900s and a second, larger peak that reaches its maxi-

mum deviation from climatology in the 1980s. When this process was repeated using only the mixed layer depth or only the Kuroshio strength as predictors, the prediction fails to adequately recreate the OHT anomaly (top and middle panels of Fig. 4.12, R^2 of 0.365 and 0.191, respectively). This emphasizes that both the underlying ENSO state *and* the variability of the Kuroshio are necessary to explain the heat transport anomaly simulated by the large ensemble.

4.7 Discussion

We have taken a distributed approach in this study and systematically worked through the various components that contribute to the PET separately. This was useful for gaining a better understanding of the processes that drive the different contributors to PET, but ignores the fact that none of these processes truly act in isolation. Therefore we briefly discuss some of the interactions between these processes.

4.7.1 The Thermally-Direct Hadley Cells and The Wind-Driven Kuroshio

The change in the ENSO regime towards more “Niño-like" months can be easily understood as a direct consequence of the warming associated with increasing greenhouse gas forcing. The change in the Kuroshio requires a longer - but still brief - explanation.

The Kuroshio is one of the western boundary currents required to balance the equatorward mass transport in the Pacific interior, as predicted by Sverdrup theory (e.g., Hartmann, 2016). This mass transport is driven by the latitudinal shear of the horizontal wind, with westward surface winds near the equator and eastward surface winds in the midlatitudes across the span of the Pacific. The strength of the equatorial winds (i.e., the trades) is driven in turn by the lower branch of the Hadley cell, which curves from primarily meridional to primarily zonal due to the influence of the Coriolis effect.

We have shown previously (Fig. 4.5) that an anomalous Hadley circulation develops centered over the equator in response to northern hemisphere aerosol forcing. Through angular momentum conservation, the stronger meridional surface flow associated with this anomalous

Hadley cell implies an increase in the magnitude of the zonal trade winds over the equatorial pacific. This increase in the latitudinal wind shear then implies an increase in the southward mass transport in the Pacific interior and, by extension, an increase in the northward mass transport by the western boundary current.

Taken together, our results suggest that aerosol forcing in the northern mid-latitudes led to an anomalous Hadley cell centered over the equator, which increased the magnitude of the trade winds over the Pacific. These stronger trades increased the wind stress on the Pacific subtropical gyre which implies (by Sverdrup theory) a strengthening of the western boundary current and a corresponding increase in northward oceanic heat transport in the Pacific.

4.7.2 Ocean Currents and Extratropical Cyclones

The increase in the frequency of ETCs (Fig. 4.7) is primarily located off the southern tip of Greenland (with a somewhat smaller change in the Pacific). This indicates a straightforward relationship between changes in the AMOC (Fig. 4.10) and the changes in the frequency of intense ETCs. The logic here is essentially the inverse of the so-called North Atlantic Warming Hole (Chemke et al., 2020; Keil et al., 2020, e.g.,) in which a *decrease* in the strength of the AMOC is associated with an isolated region of decadal-scale cooling. In these simulations the AMOC *increase* in response to aerosol forcing suggests a region of enhanced SSTs, which would support the formation and growth of ETCs.

A recent study by Needham et al. (2024b) demonstrated that the large AMOC anomaly observed in the CESM2-LE compared to the earlier CESM1 large ensemble (CESM1-LE Kay et al., 2015) was largely explained by a change in the temporal variability of turbulent heat fluxes in the North Atlantic. They further proposed the hypothesis that this variability may result from an increase in the temporal variability of CMIP6-generation forcings (including aerosols) compared to the older CMIP5-generation forcings. Additionally, they showed that the AMOC response to aerosols lags the response of the surface heat fluxes by 2-4 years.

In the context of this work, the results of that study suggest a positive feedback loop where increased cyclonic activity increases the turbulent heat fluxes from the ocean to the atmosphere, which in turn increases the strength of the AMOC, leading to warmer waters that support the growth of additional extratropical cyclones. It is possible that the increase in the frequency of intense extratropical cyclones shown in this study may explain the enhanced surface heat flux variability described by Needham et al. (2024b). If so, this would suggest that ETC changes are in some way linked to the increased inter-annual variability of the CMIP6 aerosol forcing. Another possibility (which is not mutually exclusive) is that this mechanism is somehow related to changes in the North Atlantic Oscillation (Hurrell et al., 2003) which is known to play an important role in the characteristics of Atlantic storms, but this has not been explored.

4.7.3 Conclusions

The goal of this study was to continue the work of Needham and Randall (2023) and identify which physical processes led to the positive anomaly in the integrated poleward energy transport, which that study attributed to a change in anthropogenic aerosol forcing. From this study, it should be clear that heat transport by the atmosphere and oceans is accomplished by a collection of interdependent physical processes, which combine to yield a PET which is a smooth, almost sinusoidal function of latitude constrained only by the top of atmosphere radiative balance (Stone, 1978; Trenberth and Stepaniak, 2003). To analyze this complex web of interactions, and to understand how they respond to historical forcings, we found it useful to systematically work through these various components. This led us to separate the heat transport anomaly into atmospheric heat transport by the MMC and by transient eddies (i.e. extratropical cyclones), and oceanic transport in the Atlantic and Indo-Pacific basins. The decomposition into these various anomalies provided clues about which aspects of the climate system were responsible for the change in the total poleward energy transport.

In the atmosphere, we found that both the MMC and transient eddies changed to accomplish the required heat transport. Strong extratropical cyclones became more common in the

North Atlantic, and an anomalous Hadley circulation developed on the equator which shifted the ITCZ southward while at the same time exporting additional energy northward.

In the oceans, the more complicated contribution occurred in the broadly-defined Indo-Pacific basin. Here, we found that the heat transport anomaly occurred both in the interior of the Pacific (primarily due to a change in the ENSO regime), and along the western boundary (attributed to changes in the Kuroshio current / the wind-driven ocean gyre). In the Atlantic, we ascribed changes in the OHT anomaly to a strengthening of the Atlantic Meridional Overturning Circulation.

Previous studies have shown that the AMOC response is overly sensitive to aerosol forcing in many members of the CMIP6 class of models (Menary et al., 2020; Hassan et al., 2021; Robson et al., 2022), which likely includes CESM2 (Simpson et al., 2023). This suggests that CESM2 likely overestimates the Atlantic heat transport anomaly, and by extension the total oceanic plus atmospheric heat transport anomaly, as well as the increase in ETC activity.

We do not believe that this overactive AMOC would indicate that the total PET anomaly (i.e., the OHT plus AHT) described here and in NR23 is entirely fictitious; indeed, comparison of the CESM2 large ensemble with the earlier CESM1 large ensemble (Kay et al., 2015) shows that both versions of CESM produce a heat transport anomaly in response to historic aerosol forcing, although the heat transport and AMOC responses are smaller in CESM1. Additionally, NR23 found that the ERA5 atmospheric reanalysis showed a decrease in the total PET from the 1980s to the near-present. Finally, observational studies have shown a historic southward shift of the tropical rainband which has been attributed to anomalous cross-equatorial heat transport by the atmospheric MMC in response to anthropogenic aerosol forcing (Hwang et al., 2013; Allen et al., 2015; Irving et al., 2019; Lembo et al., 2019; Yukimoto et al., 2022).

However we do conclude that the large AMOC response and corresponding large OHT anomaly in the Atlantic - alongside the related atmospheric eddy heat transport in the Atlantic storm track - indicate that the historic PET anomaly predicted by the ensemble mean of the CESM2 large ensemble is likely too large, although it is difficult to quantify the magnitude of this over-

prediction. Satellite measurement of the Earth's energy balance are the only direct way to accurately measure this total transport, and continuous observations only exist for the twenty-first century (Loeb et al., 2018). In the absence of a continuous observational record covering the twentieth century, we must instead rely on observations and reconstructions of varied phenomena (e.g., historical observations of the AMOC change Rahmstorf et al., 2015; Caesar et al., 2018; Menary et al., 2020; Caesar et al., 2021) to constrain the past changes in poleward energy transport.

References

Adam, O., Bischoff, T., and Schneider, T. (2016). Seasonal and interannual variations of the energy flux equator and ITCZ. part i: Zonally averaged ITCZ position. *J. Clim.*, 29(9):3219–3230.

Allen, R. J., Evan, A. T., and Booth, B. B. B. (2015). Interhemispheric aerosol radiative forcing and tropical precipitation shifts during the late twentieth century. *J. Clim.*, 28(20):8219–8246.

Armour, K. C., Siler, N., Donohoe, A., and Roe, G. H. (2019). Meridional atmospheric heat transport constrained by energetics and mediated by Large-Scale diffusion. *J. Clim.*, 32(12):3655–3680.

Bjerknes, J. (1964). Atlantic Air-Sea interaction. *Adv. Geophys.*, 10:1–82.

Caesar, L., McCarthy, G. D., Thornalley, D. J. R., Cahill, N., and Rahmstorf, S. (2021). Current atlantic meridional overturning circulation weakest in last millennium. *Nat. Geosci.*, 14(3):118–120.

Caesar, L., Rahmstorf, S., Robinson, A., Feulner, G., and Saba, V. (2018). Observed fingerprint of a weakening atlantic ocean overturning circulation. *Nature*, 556(7700):191–196.

Chemke, R., Zanna, L., and Polvani, L. M. (2020). Identifying a human signal in the north atlantic warming hole. *Nat. Commun.*, 11(1):1540.

Cheng, L., Trenberth, K. E., Fasullo, J. T., Mayer, M., Balmaseda, M., and Zhu, J. (2019). Evolution of ocean heat content related to ENSO. *J. Clim.*, 32(12):3529–3556.

Chiang, J. C. H. and Bitz, C. M. (2005). Influence of high latitude ice cover on the marine intertropical convergence zone. *Clim. Dyn.*, 25(5):477–496.

Cox, T., Donohoe, A., Roe, G. H., Armour, K. C., and Frierson, D. M. W. (2022). Near invariance of poleward atmospheric heat transport in response to midlatitude orography. *J. Clim.*, 35(13):4099–4113.

Czaja, A. and Marshall, J. (2006). The partitioning of poleward heat transport between the atmosphere and ocean. *J. Atmos. Sci.*, 63(5):1498–1511.

Danabasoglu, G., Lamarque, J.-F., Bacmeister, J., Bailey, D. A., DuVivier, A. K., Edwards, J., Emmons, L. K., Fasullo, J., Garcia, R., Gettelman, A., Hannay, C., Holland, M. M., Large, W. G., Lauritzen, P. H., Lawrence, D. M., Lenaerts, J. T. M., Lindsay, K., Lipscomb, W. H., Mills, M. J., Neale, R., Oleson, K. W., Otto-Bliesner, B., Phillips, A. S., Sacks, W., Tilmes, S., Kampenhout, L., Vertenstein, M., Bertini, A., Dennis, J., Deser, C., Fischer, C., Fox-Kemper, B., Kay, J. E., Kinnison, D., Kushner, P. J., Larson, V. E., Long, M. C., Mickelson, S., Moore, J. K., Nienhouse, E., Polvani, L., Rasch, P. J., and Strand, W. G. (2020). The community earth system model version 2 (CESM2). *J. Adv. Model. Earth Syst.*, 12(2).

Deser, C., Phillips, A. S., Simpson, I. R., Rosenbloom, N., Coleman, D., Lehner, F., Pendergrass, A. G., DiNezio, P., and Stevenson, S. (2020). Isolating the evolving contributions of anthropogenic aerosols and greenhouse gases: A new CESM1 large ensemble community resource. *J. Clim.*, 33(18):7835–7858.

Donohoe, A. and Voigt, A. (2017). Why future shifts in tropical precipitation will likely be small: The location of the tropical rain belt and the hemispheric contrast of energy input to the atmosphere. In Wang, S.-Y. S., Yoon, J.-H., Funk, C. C., and Gillies, R. R., editors, *Climate Extremes*, volume 6 of *Geophysical Monograph Series*, pages 115–137. John Wiley & Sons, Inc., Hoboken, NJ, USA.

Enderton, D. and Marshall, J. (2009). Explorations of Atmosphere–Ocean–Ice climates on an aquaplanet and their meridional energy transports. *J. Atmos. Sci.*, 66(6):1593–1611.

Eyring, V., Bony, S., Meehl, G. A., Senior, C. A., Stevens, B., Stouffer, R. J., and Taylor, K. E. (2016). Overview of the coupled model intercomparison project phase 6 (CMIP6) experimental design and organization. *Geosci. Model Dev.*, 9(5):1937–1958.

Fasullo, J. T., Lamarque, J.-F., Hannay, C., Rosenbloom, N., Tilmes, S., DeRepentigny, P., Jahn, A., and Deser, C. (2022). Spurious late historical-era warming in CESM2 driven by prescribed biomass burning emissions. *Geophys. Res. Lett.*, 49(2).

Frierson, D. M. W., Hwang, Y.-T., Fučkar, N. S., Seager, R., Kang, S. M., Donohoe, A., Maroon, E. A., Liu, X., and Battisti, D. S. (2013). Contribution of ocean overturning circulation to tropical rainfall peak in the northern hemisphere. *Nat. Geosci.*, 6(11):940–944.

Hartmann, D. L. (2016). *Global Physical Climatology*. Elsevier.

Hassan, T., Allen, R. J., Liu, W., and Randles, C. A. (2021). Anthropogenic aerosol forcing of the atlantic meridional overturning circulation and the associated mechanisms in CMIP6 models. *Atmos. Chem. Phys.*, 21(8):5821–5846.

Held, I. M. (2001). The partitioning of the poleward energy transport between the tropical ocean and atmosphere. *J. Atmos. Sci.*, 58(8):943–948.

Hersbach, H., Bell, B., Berrisford, P., Hirahara, S., Horányi, A., Muñoz-Sabater, J., Nicolas, J., Peubey, C., Radu, R., Schepers, D., Simmons, A., Soci, C., Abdalla, S., Abellan, X., Balsamo, G., Bechtold, P., Biavati, G., Bidlot, J., Bonavita, M., Chiara, G., Dahlgren, P., Dee, D., Diamantakis, M., Dragani, R., Flemming, J., Forbes, R., Fuentes, M., Geer, A., Haimberger, L., Healy, S., Hogan, R. J., Hólm, E., Janisková, M., Keeley, S., Laloyaux, P., Lopez, P., Lupu, C., Radnoti, G., Rosnay, P., Rozum, I., Vamborg, F., Villaume, S., and Thépaut, J. (2020). The ERA5 global reanalysis. *Q.J.R. Meteorol. Soc.*, 146(730):1999–2049.

Hoesly, R. M., Smith, S. J., Feng, L., Klimont, Z., Janssens-Maenhout, G., Pitkanen, T., Seibert, J. J., Vu, L., Andres, R. J., Bolt, R. M., Bond, T. C., Dawidowski, L., Kholod, N., Kurokawa, J.-I., Li, M., Liu, L., Lu, Z., Moura, M. C. P., O'Rourke, P. R., and Zhang, Q. (2018). Historical (1750–2014) anthropogenic emissions of reactive gases and aerosols from the community emissions data system (CEDS). *Geosci. Model Dev.*, 11(1):369–408.

Hoskins, B. J. and Valdes, P. J. (1990). On the existence of Storm-Tracks. *J. Atmos. Sci.*, 47(15):1854–1864.

Hoyer, S. and Hamman, J. (2017). xarray: N-D labeled arrays and datasets in Python. *Journal of Open Research Software*, 5(1).

Hurrell, J. W., Kushnir, Y., Ottersen, G., and Visbeck, M. (2003). An overview of the north atlantic oscillation. In Hurrell, J. W., Kushnir, Y., Ottersen, G., and Visbeck, M., editors, *The North Atlantic Oscillation: Climatic Significance and Environmental Impact*, volume 134 of *Geophysical Monograph Series*, pages 1–35. American Geophysical Union, 2000 Florida Avenue, N. W. Washington, DC 20009.

Hwang, Y.-T., Frierson, D. M. W., and Kang, S. M. (2013). Anthropogenic sulfate aerosol and the southward shift of tropical precipitation in the late 20th century. *Geophys. Res. Lett.*, 40(11):2845–2850.

Irving, D. B., Wijffels, S., and Church, J. A. (2019). Anthropogenic aerosols, greenhouse gases, and the uptake, transport, and storage of excess heat in the climate system. *Geophys. Res. Lett.*, 46(9):4894–4903.

Kang, S. M. (2020). Extratropical influence on the tropical rainfall distribution. *Current Climate Change Reports*, 6(1):24–36.

Kang, S. M., Held, I. M., Frierson, D. M. W., and Zhao, M. (2008). The response of the ITCZ to extratropical thermal forcing: Idealized slab-ocean experiments with a GCM. *J. Clim.*, 21(14):3521–3532.

Kay, J. E., Deser, C., Phillips, A., Mai, A., Hannay, C., Strand, G., Arblaster, J. M., Bates, S. C., Danabasoglu, G., Edwards, J., Holland, M., Kushner, P., Lamarque, J.-F., Lawrence, D., Lindsay, K., Middleton, A., Munoz, E., Neale, R., Oleson, K., Polvani, L., and Vertenstein, M. (2015). The community earth system model (CESM) large ensemble project: A community resource for studying climate change in the presence of internal climate variability. *Bull. Am. Meteorol. Soc.*, 96(8):1333–1349.

Keil, P., Mauritsen, T., Jungclaus, J., Hedemann, C., Olonscheck, D., and Ghosh, R. (2020). Multiple drivers of the north atlantic warming hole. *Nat. Clim. Chang.*, 10(7):667–671.

Kiehl, J. T. and Trenberth, K. E. (1997). Earth's annual global mean energy budget. *Bull. Am. Meteorol. Soc.*, 78(2):197–208.

Knietzsch, M.-A., Schröder, A., Lucarini, V., and Lunkeit, F. (2015). The impact of oceanic heat transport on the atmospheric circulation. *Earth Syst. Dyn.*, 6(2):591–615.

Lembo, V., Folini, D., Wild, M., and Lionello, P. (2019). Inter-hemispheric differences in energy budgets and cross-equatorial transport anomalies during the 20th century. *Clim. Dyn.*, 53(1):115–135.

Li, S., Liu, W., Allen, R. J., Shi, J.-R., and Li, L. (2023). Ocean heat uptake and interbasin redistribution driven by anthropogenic aerosols and greenhouse gases. *Nat. Geosci.*, 16(8):695–703.

Loeb, N. G., Doelling, D. R., Wang, H., Su, W., Nguyen, C., Corbett, J. G., Liang, L., Mitrescu, C., Rose, F. G., and Kato, S. (2018). Clouds and the earth's radiant energy system (CERES) energy balanced and filled (EBAF) Top-of-Atmosphere (TOA) edition-4.0 data product. *J. Clim.*, 31(2):895–918.

Ma, X., Liu, W., Allen, R. J., Huang, G., and Li, X. (2020). Dependence of regional ocean heat uptake on anthropogenic warming scenarios. *Sci Adv*, 6(45).

Marshall, J., Donohoe, A., Ferreira, D., and McGee, D. (2013). The ocean's role in setting the mean position of the Inter-Tropical convergence zone. *Clim. Dyn.*, 42(7):1967–1979.

Menary, M. B., Robson, J., Allan, R. P., Booth, B. B. B., Cassou, C., Gastineau, G., Gregory, J., Hodson, D., Jones, C., Mignot, J., Ringer, M., Sutton, R., Wilcox, L., and Zhang, R. (2020). Aerosol-forced AMOC changes in CMIP6 historical simulations. *Geophys. Res. Lett.*, 47(14).

Ming, Y. and Ramaswamy, V. (2011). A model investigation of Aerosol-Induced changes in tropical circulation. *J. Clim.*, 24(19):5125–5133.

Needham, M. R., Cox, T., and Randall, D. A. (2024a). Aerosol-Induced changes in atmospheric and oceanic heat transports in the CESM2 large ensemble. *J. Clim.*, -1(aop).

Needham, M. R., Falter, D. D., and Randall, D. A. (2024b). Changes in external forcings drive divergent AMOC responses across CESM generations. *Geophys. Res. Lett.*, 51(5).

Needham, M. R. and Randall, D. A. (2021). Riehl and malkus revisited: The role of cloud radiative effects. *J. Geophys. Res.*, 126(16).

Needham, M. R. and Randall, D. A. (2023). Anomalous northward energy transport due to anthropogenic aerosols during the twentieth century. *J. Clim.*, 36(19):6713–6728.

Neelin, J. D. and Held, I. M. (1987). Modeling tropical convergence based on the moist static energy budget. *Mon. Weather Rev.*, 115(1):3–12.

Oort, A. H. (1971). The observed annual cycle in the meridional transport of atmospheric energy. *J. Atmos. Sci.*, 28(3):325–339.

Pearce, F. A. and Bodas-Salcedo, A. (2023). Implied heat transport from CERES data: Direct radiative effect of clouds on regional patterns and hemispheric symmetry. *J. Clim.*, 36(12):4019–4030.

Rahmstorf, S. (2002). Ocean circulation and climate during the past 120,000 years. *Nature*, 419(6903):207–214.

Rahmstorf, S., Box, J. E., Feulner, G., Mann, M. E., Robinson, A., Rutherford, S., and Schaffernicht, E. J. (2015). Exceptional twentieth-century slowdown in atlantic ocean overturning circulation. *Nat. Clim. Chang.*, 5(5):475–480.

Ramanathan, V. (1987). The role of earth radiation budget studies in climate and general circulation research. *J. Geophys. Res.*, 92(D4):4075.

Ramanathan, V., Cess, R. D., Harrison, E. F., Minnis, P., Barkstrom, B. R., Ahmad, E., and Hartmann, D. L. (1989). Cloud-Radiative forcing and climate: Results from the earth radiation budget experiment. *Science*, 243(4887):57–63.

Riehl, H. and Malkus, J. S. (1958). On the heat balance in the equatorial trough zone. *Geophysica*, 6:503–537.

Robson, J., Menary, M. B., Sutton, R. T., Mecking, J., Gregory, J. M., Jones, C., Sinha, B., Stevens, D. P., and Wilcox, L. J. (2022). The role of anthropogenic aerosol forcing in the 1850–1985 strengthening of the AMOC in CMIP6 historical simulations. *J. Clim.*, 35(20):3243–3263.

Rodgers, K. B., Lee, S.-S., Rosenbloom, N., Timmermann, A., Danabasoglu, G., Deser, C., Edwards, J., Kim, J.-E., Simpson, I. R., Stein, K., Stuecker, M. F., Yamaguchi, R., Bódai, T., Chung, E.-S., Huang, L., Kim, W. M., Lamarque, J.-F., Lombardozzi, D. L., Wieder, W. R., and Yeager, S. G. (2021). Ubiquity of human-induced changes in climate variability. *Earth Syst. Dyn.*, 12(4):1393–1411.

Rose, B. E. J. and Ferreira, D. (2012). Ocean heat transport and water vapor greenhouse in a warm equable climate: A new look at the low gradient paradox. *J. Clim.*, 26(6):2117–2136.

Schneider, T., Bischoff, T., and Haug, G. H. (2014). Migrations and dynamics of the intertropical convergence zone. *Nature*, 513(7516):45–53.

Shaw, T. A. and Smith, Z. (2022). The midlatitude response to polar sea ice loss: Idealized Slab-Ocean aquaplanet experiments with thermodynamic sea ice. *J. Clim.*, 35(8):2633–2649.

Simpson, I. R., Rosenbloom, N., Danabasoglu, G., Deser, C., Yeager, S. G., McCluskey, C. S., Yamaguchi, R., Lamarque, J.-F., Tilmes, S., Mills, M. J., and Rodgers, K. B. (2023). The CESM2 Single-Forcing large ensemble and comparison to CESM1: Implications for experimental design. *J. Clim.*, 36(17):5687–5711.

Stone, P. H. (1978). Constraints on dynamical transports of energy on a spherical planet. *Dyn. Atmos. Oceans*, 2(2):123–139.

Sverdrup, H. U. (1942). *The Oceans Their Physics, Chemistry, and General Biology*. Prentive-Hall, INC.

Thornalley, D. J. R., Oppo, D. W., Ortega, P., Robson, J. I., Brierley, C. M., Davis, R., Hall, I. R., Moffa-Sanchez, P., Rose, N. L., Spooner, P. T., Yashayaev, I., and Keigwin, L. D. (2018). Anomalously weak labrador sea convection and atlantic overturning during the past 150 years. *Nature*, 556(7700):227–230.

Trenberth, K. E. (1979). Mean annual poleward energy transports by the oceans in the southern hemisphere. *Dyn. Atmos. Oceans*, 4(1):57–64.

Trenberth, K. E. (1997). The definition of el niño. *Bull. Am. Meteorol. Soc.*, 78(12):2771–2778.

Trenberth, K. E., Fasullo, J. T., and Kiehl, J. (2009). Earth's global energy budget. *Bull. Am. Meteorol. Soc.*, 90(3):311–324.

Trenberth, K. E. and Stepaniak, D. P. (2003). Seamless poleward atmospheric energy transports and implications for the hadley circulation. *J. Clim.*, 16(22):3706–3722.

Trenberth, K. E. and Stepaniak, D. P. (2004). The flow of energy through the earth's climate system. *Q. J. R. Meteorol. Soc.*, 130(603):2677–2701.

Trenberth, K. E. and Zhang, Y. (2019). Observed interhemispheric meridional heat transports and the role of the indonesian throughflow in the pacific ocean. *J. Clim.*, 32(24):8523–8536.

Ullrich, P. A., Zarzycki, C. M., McClenny, E. E., Pinheiro, M. C., Stansfield, A. M., and Reed, K. A. (2021). TempestExtremes v2.1: a community framework for feature detection, tracking, and analysis in large datasets. *Geosci. Model Dev.*, 14(8):5023–5048.

von Schuckmann, K., Palmer, M. D., Trenberth, K. E., Cazenave, A., Chambers, D., Champollion, N., Hansen, J., Josey, S. A., Loeb, N., Mathieu, P.-P., Meyssignac, B., and Wild, M. (2016). An imperative to monitor earth's energy imbalance. *Nat. Clim. Chang.*, 6(2):138–144.

Vonder Haar, T. H. and Oort, A. H. (1973). New estimate of annual poleward energy transport by northern hemisphere oceans. *J. Phys. Oceanogr.*, 3(2):169–172.

Walker, E., Mitchell, D., and Seviour, W. (2020). The numerous approaches to tracking extratropical cyclones and the challenges they present. *Weather*, 75(11):336–341.

Yukimoto, S., Oshima, N., Kawai, H., Deushi, M., and Aizawa, T. (2022). Role of interhemispheric heat transport and global atmospheric cooling in multidecadal trends of northern hemisphere precipitation. *Geophys. Res. Lett.*, 49(18).

Chapter 5

Changes in External Forcings Drive Divergent AMOC Responses Across CESM Generations

This chapter is an exact republication of the text and figures (with the exception of section numbering, which has been modified to align with the larger numbering of this dissertation) from the article of the same name (Needham et al., 2024) originally published in *Geophysical Research Letters* in March, 2024, under the DOI: **https://doi.org/10.1029/2023GL106410**

Overview

It has been suggested that the Atlantic meridional overturning circulation (AMOC) in many CMIP6 models is overly-sensitive to anthropogenic aerosol forcing, and it has been proposed that this is due to the inclusion of aerosol indirect effects for the first time in many CMIP6 models. We analyze the AMOC response in a newly-released ensemble of simulations performed with CESM2 forced by the CMIP5 input datasets (CESM2-CMIP5). This AMOC response is then compared to the CMIP5-generation CESM1 large ensemble (CESM1-LE) and the CMIP6-generation CESM2 large ensemble (CESM2-LE). A key conclusion, only made possible by this experimental setup, is that changes in aerosol-indirect effects cannot explain differences in AMOC response between CESM1-LE and CESM2-LE. Instead, we hypothesize that the difference is due to increased interannual variability of anthropogenic emissions. This forcing variability may act through a nonlinear relationship between the surface heat budget of the North Atlantic and the AMOC.

Plain Language Summary

The Atlantic meridional overturning circulation (AMOC) is important for the wider climate because it transports a large amount of warm water northward away from the equator. The most recent generation of climate models disagree with the observed behavior of the AMOC over the twentieth century, and it has been suggested that this is due to the inclusion of aerosol-cloud interactions in many of the newest models. Here we look at model simulations of the AMOC in several configurations to show that the disagreement in the past AMOC behavior is instead primarily due to changes in the inputs given to the models, rather than to changes in the models themselves.

5.1 Introduction

The Atlantic meridional overturning circulation (AMOC; Rahmstorf, 2002; Buckley and Marshall, 2015; Lozier et al., 2019; Srokosz et al., 2021) is crucial in determining the local climate of the regions bordering the North Atlantic. It also plays a key role in the wider climate by accomplishing a significant portion of the necessary poleward energy transport determined by the TOA radiation balance (Trenberth and Caron, 2001; Chiang et al., 2008; Frierson et al., 2013; Marshall et al., 2013; Trenberth and Fasullo, 2017; Needham and Randall, 2023). The future behavior of the AMOC is of great interest because of its important role in the climate system: it has been identified as a potential climate “tipping point," (Broecker, 1987; Lenton et al., 2019; Brovkin et al., 2021; Ditlevsen and Ditlevsen, 2023), with the potential for a slowdown or collapse of the AMOC due to greenhouse gas-induced changes in the heat and salinity budgets of the north Atlantic.

Indirect observational and proxy-based estimates suggest that the AMOC has entered a period of decline, with a general slowdown relative to the pre-industrial era, particularly over the course of the twentieth century (Rahmstorf et al., 2015; Thornalley et al., 2018; Caesar et al., 2018, 2021), although this conclusion is not universally accepted (Worthington et al., 2021). In contrast, many models that participated in the most recent phase of the coupled model inter-

comparison project (CMIP6; Eyring et al., 2016) predicted an *increase* in the strength of the AMOC over much of the twentieth century, likely due to the models' overly-sensitive response to anthropogenic aerosol forcing (Menary et al., 2020; Hassan et al., 2021; Robson et al., 2022). These CMIP6 models also disagree with the older models of the CMIP5 generation, which more closely match observational AMOC estimates (Cheng et al., 2013; Menary et al., 2020).

The importance of the AMOC to the climate, and this significant model-observation disagreement motivate us to understand why models that participated in CMIP6 tend to overestimate the AMOC response to historic aerosol forcing. One hypothesis is that the first-time inclusion of aerosol-cloud interactions in many CMIP6 models (Wang et al., 2021) led to excessive cooling of the northern relative to the southern hemisphere, which induced an increase in the strength of the AMOC (Menary et al., 2020). In this study we analyze a different hypothesis that has not yet been investigated to our knowledge: our goal is to quantify to what extent the change in external forcings from CMIP5 to CMIP6 contributes to the divergent AMOC responses of the CMIP5 and CMIP6 models. This hypothesis does not contradict the aerosol-cloud interaction hypothesis: both can contribute.

5.2 Data

We utilize three ensembles of coupled historical (1850- or 1920-present) simulations performed with the first (CESM1; Hurrell et al., 2013) or the second (CESM2; Danabasoglu et al., 2020) version of the Community Earth System Model at a nominal 1° horizontal atmospheric resolution. The first is a set of 35 simulations from the CESM1 large ensemble project using CMIP5 forcings (hereafter CESM1-LE; Kay et al., 2015); the second is 50 of the 100 simulations from the CESM2 large ensemble project using CMIP6 forcings (hereafter CESM2-LE; Rodgers et al., 2021); the third is 10 of the 15 simulations (only 10 simulations included all necessary fields at the time of analysis) performed using CESM2 but forced by the older CMIP5 inputs (hereafter CESM2-CMIP5; Holland et al., 2023). We use only the 50 members of the CESM2-LE which utilize smoothed biomass burning rather than the native CMIP6 biomass burning, be-

cause the later has been shown to lead to anomalous northern hemisphere warming towards the end of the historical period (Fasullo et al., 2022).

These three experimental configurations allow us to separate the different AMOC response to historic forcing into two components: the difference between CESM1-LE and CESM2-CMIP5 gives the impact of changing model versions with the external inputs held constant, while the difference between CESM2-CMIP5 an CESM2-LE gives the impact of changing the emissions from CMIP5 to CMIP6 in the same version of the model. Crucially, the CESM1 large ensemble employed the community atmosphere model version 5, which *does* include a representation of aerosol-cloud interactions (Hurrell et al., 2013; Kay et al., 2015), although the treatment of these interactions is different between CESM1 and CESM2 (Danabasoglu et al., 2020). Specifically, the atmospheric component of CESM2 utilizes an updated cloud microphysics scheme (MG2; Gettelman and Morrison, 2015) and an updated, four-mode aerosol model (MAM4; Liu et al., 2016).

All fields are ensemble means calculated from monthly mean model output. Annual mean timeseries anomalies are first computed by calculating monthly anomalies from the 20-year climatology defined as 1921-1940 - the earliest period that is common to all simulations - and then calculating the average anomaly for each year. Yearly time series are then smoothed with an 11 year gaussian filter with a standard deviation of 5 years.

5.3 AMOC Response to Historical Forcings

Panel a of Fig. 5.1 shows the time series of the ensemble mean AMOC index anomaly for each of the three sets of simulations. The AMOC index is calculated as the maximum value of the overturning streamfunction in the Atlantic basin below a depth of 500 meters (Liu et al., 2020). Shading shows the interquartile range among ensemble members. We use only the Eulerian component of the MOC, which is explicitly resolved by the model, although results are similar when the total (i.e., resolved plus parameterized) AMOC is analyzed (not shown).

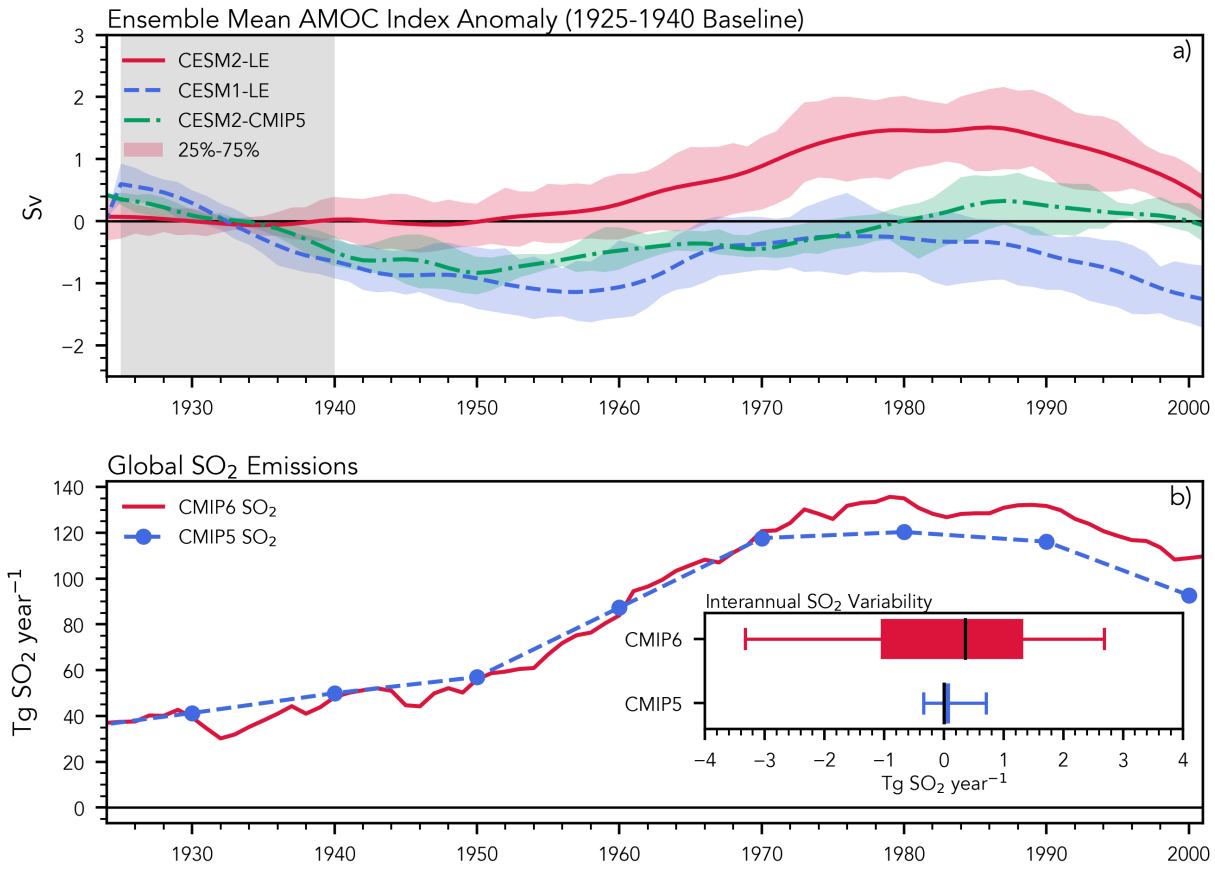

Figure 5.1: a) Time series of the ensemble mean AMOC anomaly for three ensembles of climate simulations performed using the CESM (see text for details of model configurations and forcings) **b)** Global SO_2 emissions for CMIP5 and CMIP6. **Inset)** Box plots of interannual SO_2 variability, defined as SO_2 minus smoothed SO_2 where the smoothing has been perforemd with the 11 year Gaussian filter. Whiskers show the 5^{th} and 95^{th} percentiles.

The AMOC anomaly from the CESM2-LE (red curve) peaks in the later quarter of the twentieth century, which is consistent with other CMIP6 generation models (Menary et al., 2020; Robson et al., 2022). The AMOC anomaly from the CESM1-LE (blue curve) is typically negative over the historical period relative to 1921-1940, which in turn is consistent with other CMIP5 models. This establishes that CESM1 under CMIP5 and CESM2 under CMIP6 forcings are at least nominally representative of the wider CMIP5 and CMIP6 population of models discussed by Menary et al. (2020).

The AMOC anomaly from the CESM2-CMIP5 simulations (green curve) much more closely follows the CESM1-LE rather than the CESM2-LE curve from the beginning of the simulations in 1920 through to the 1980s. After about 1985 the CESM2-CMIP5 anomaly is essentially flat while both the CESM1-LE and CESM2-LE anomalies decrease at essentially the same rate. This result is the key finding of this study; it shows that the AMOC response in CESM2 is strongly dependent on the particular historical inputs (i.e., CMIP5 vs. CMIP6 emissions) to that model. It also establishes that the difference in AMOC response in CESM2-LE vs CESM1-LE cannot be explained solely by changes to the model.

Previous studies have attributed the divergent AMOC responses of the CMIP5 and CMIP6 models to enhanced northern hemispheric cooling in CMIP6 models associated with the inclusion of aerosol indirect effects. However, as mentioned in the previous section, all three ensembles analyzed here employ atmospheric models (either CAM5 or CAM6) which include representations of aerosol-cloud interactions, yet we still observe a large difference in the AMOC response between the two ensembles forced with CMIP5 inputs and the CESM2-LE, which is forced by CMIP6 inputs. This result suggests that some property of the aerosol emissions is driving the divergent AMOC responses, and not the models' treatment of aerosol indirect effects.

The emissions of SO_2 are shown in panel b of Fig. 5.1 and are analyzed as a bellwether for the wider group of aerosol precursors. On decadal time-scales the CMIP5 and CMIP6 emissions are largely similar, with a gradual increase throughout the twentieth century that accelerates af-

ter about 1950, peaks around 1980 and then begins to decline towards the end of the century. The magnitude of the emission rates is similar especially before 1970. The primary difference is that the CMIP5 emissions are given once a decade (blue points) and then interpolated to yearly timescales (blue dashed line), while the CMIP6 emissions are given once a year. Consequently, there is a higher degree of interannual variability in the CMIP6 SO2 emissions. This is shown in the inset of Fig. 5.1b, where the interannual variability is illustrated by showing the distribution of SO_2 emissions after the decadal-scale behavior has been removed (by subtracting the timeseries of the emissions after smoothing with the Gaussian filter). It is conceivable, then, that the higher temporal variability of these emissions in some way leads to the different AMOC response seen in the CESM2-LE and CESM2-CMIP5 ensembles. We return to this point in the discussion section.

5.4 Energy Budget of the North Atlantic

The AMOC is generally understood to be driven by a meridional pressure gradient between the tropics and higher latitudes. This pressure gradient is maintained by North Atlantic surface water which sinks when it becomes anomalously cold and salty (i.e., through thermodynamic and haline effects). As discussed in the supporting information, we find that thermal fluxes are much more important in driving the AMOC than salinity-changing processes. Therefore, we next investigate the surface energy balance of the north Atlantic.

The top row of Fig. 5.2 shows the average anomaly (1960-1989, relative to the 1921-1940 climatology) of the net surface energy flux over the subpolar north Atlantic (SPNA). It is immediately obvious that CESM2-LE has a much larger energy flux anomaly than either the CESM1-LE or the CESM2-CMIP5. The spatial pattern is also different, with CESM2-LE producing negative anomalies across the entire north Atlantic, while CESM1-LE and CESM2-CMIP5 have a similar spatial structure with varying positive and negative anomalies. The middle row of the same figure shows the ensemble mean sensible plus latent turbulent heat flux. It is clear that the

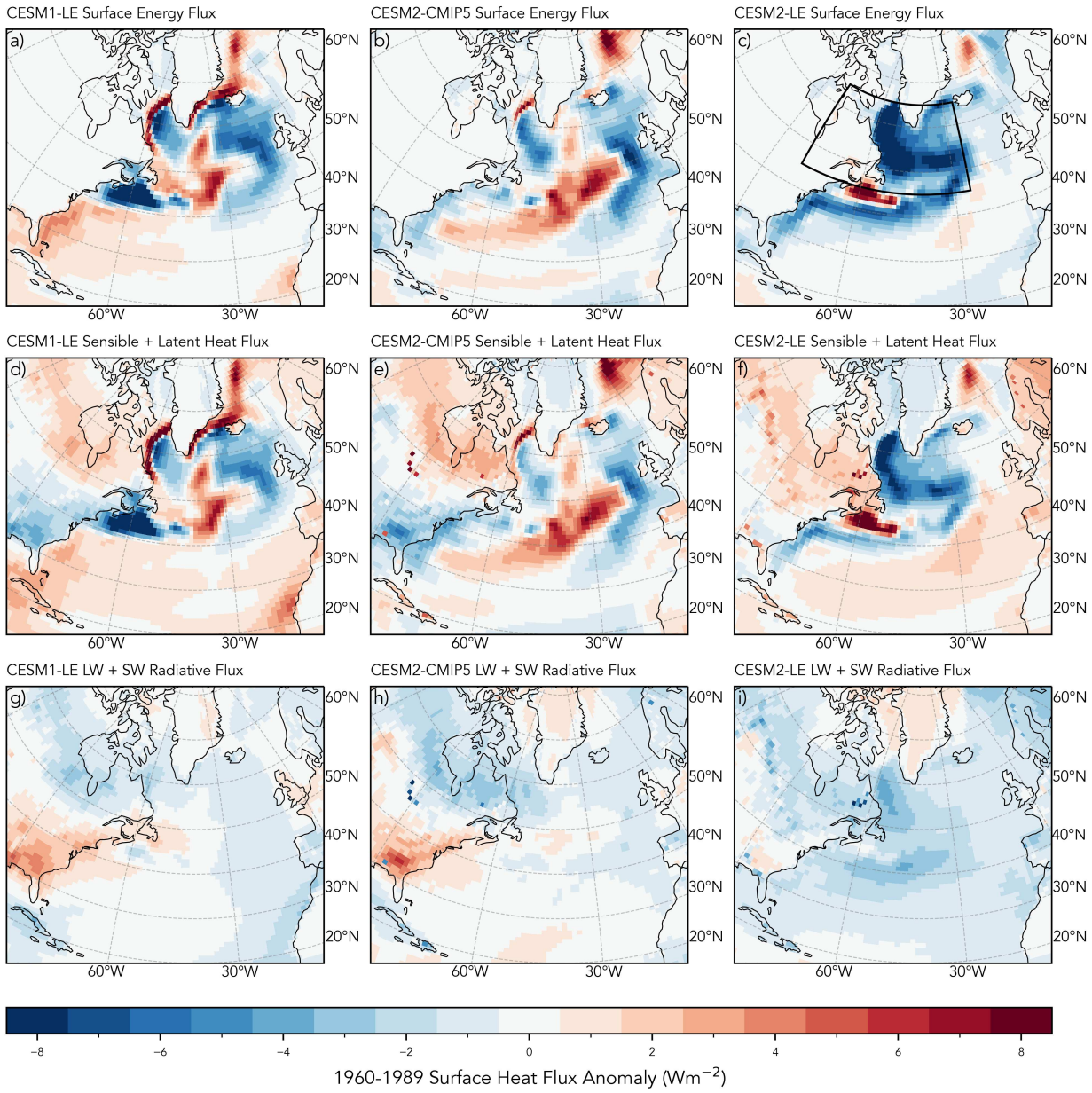

Figure 5.2: Top Row) Ensemble mean anomaly (1960-1989) in the net energy balance in the north Atlantic for the CESM1-LE, CESM2-CMIP5, and CESM2-LE ensembles, (left, center, and right columns, respectively). **Middle Row)** as in **Top Row** but for the anomaly in the net sensible plus latent turbulent heat flux. **Bottom Row)** as in **Top Row** but for the anomaly in the net longwave plus shortwave radiative flux at the surface. Negative (blue) values indicate an anomalous *heat loss* out of the ocean. The black boxed region in **panel c** indicates the region used for spatial averages in Fig. 5.4, and is bounded by 80°W-25°W and 45°N-65°N.

spatial structure of the surface heat flux anomaly (i.e., the top row) is primarily determined by turbulent surface fluxes, and not by surface radiation fluxes (i.e., the bottom row).

Similar to the SO_2 emissions in Fig. 5.1, we find a greater degree of interannual variability in the CESM2-LE net surface energy flux than in either of the other ensembles, which is shown in Fig. 5.3. Panel a shows the result of a bootstrapping approach to compare the ensemble mean of the 10 member CESM2-CMIP5 ensemble with that of the CESM1 and CESM2 ensembles for the standard deviation of the surface energy flux terms averaged over the subpolar North Atlantic (SPNA; shown as the outlined region in panel c of Fig. 5.2). The distributions were calculated by randomly selecting 10 ensemble members out of the 50 (35) ensemble members from the CESM2 (CESM1) large ensemble, calculating the temporal standard deviation of the area-weighted annual mean timeseries, then calculating the average for the 10 ensemble members, and repeating this process 500 times. The standard deviations were calculated after removing the decadal scale behavior by calculating a smoothed timeseries using the same 11 year Gaussian filter and subtracting this from the full timeseries.

The SPNA energy flux in the CESM2-LE (red boxes) shows greater interannual variability than the other two ensembles. This is primarily due to the turbulent fluxes of latent and sensible heat with very little contribution from the radiative fluxes. From this experimental setup, the difference in interannual variability must be due to both changes in the model between CESM 1 and CESM2, and to the different CMIP5 vs. CMIP6 forcings. As the difference between the CESM2-CMIP5 and CESM2-LE ensembles is by definition due to changes in the forcings, this suggests the possibility that increased interannual variability in emissions may contribute to the increased interannual variability in the SPNA energy flux.

Even if this is shown to be the case, it must then be demonstrated that the SPNA energy flux in turn drives the AMOC response in the CESM2-LE, and not that the energy flux is in some way driven by the anomalous AMOC. One piece of evidence supporting this interpretation is shown in the bottom panel of Fig. 5.3. Here, we have performed a time-lagged correlation analysis between these two variables. For a given offset (in years), we performed a similar boot-

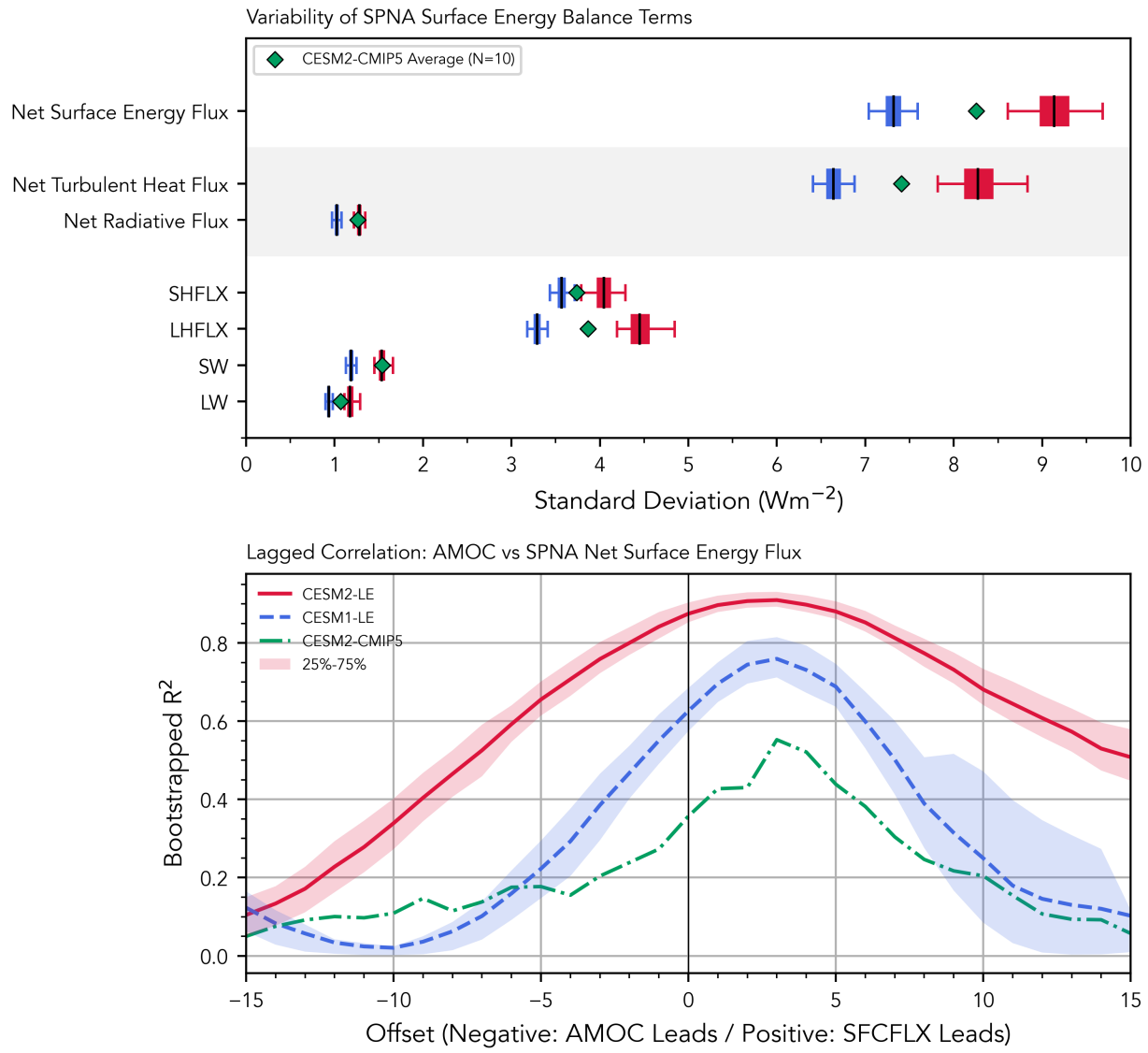

Figure 5.3: Top) Boxplots show the interannual variability (calculated using a bootstrapping method based on the mean of the yearly standard deviation; see text) of the terms of the SPNA heat budget between the CESM1-LE and CESM2-LE ensembles (blue and red, respectively), alongside the average standard deviation of the 10 CESM2-CMIP5 ensemble. Edges of boxes show the inter-quartile range, and whiskers indicate the 5th and 95th percentiles. Note the logarithmic scaling of the horizontal axis. **Bottom Panel** Time-lag correlation between AMOC anomaly and SPNA net surface heat flux computed using a bootstrapping method (again, see text for details). When the offset is positive (negative) AMOC lags (leads) SFCFLX.

strapping method to that used in the top panel of the figure to generate the distribution of the 10-member sub-ensemble mean R^2 correlation for each of the large ensembles. We find the highest correlation when the surface energy flux anomaly leads the AMOC anomaly by about 2-3 years. This temporal relationship, combined with the canonical understanding of the AMOC as being driven by surface water that sinks in the north Atlantic after experiencing changes to its thermodynamic (i.e., through surface energy fluxes) and haline (i.e., through surface freshwater exchanges, which we show in the supporting information to be much less important) properties suggests that the arrow of causality points from the SPNA heat fluxes to the AMOC and not the other way around.

5.5 Discussion

As stated above, the primary result of this study is to show that the divergent AMOC responses to historical forcings between CESM1 and CESM2 is largely due to the changes in emissions between CMIP5 and CMIP6. It is beyond the scope of this study to definitively answer why the AMOC response in CESM2 is more sensitive to CMIP6 than CMIP5 forcings, however we briefly discuss one intriguing possibility here. As illustrated in panel b of Fig. 5.1, the CMIP5 emissions estimates compiled by Lamarque et al. (2010) provided data at 10-year intervals: in contrast, the CMIP6 estimates compiled by Hoesly et al. (2018) are provided on an annual basis. We propose the hypothesis that the greater interannual variability of the CMIP6 forcings led to the stronger AMOC response in CESM2 purely because of the model's sensitivity to forcing variability. Our subsequent analysis (i.e., Figs. 5.2-5.3) suggests that the interannual variability of emissions may be imprinted upon the surface energy flux, which appears to then drive the AMOC with a lag time of 2-4 years.

If confirmed, this hypothesis would be in line with a recent study by Fasullo et al. (2022). They showed that a discontinuity in the variability of biomass burning forcing - which arose from the inclusion of satellite observations of wildfire emissions from 1997-2014 but not before or after - led to “spurious warming" near the end of historical simulations performed with

CESM2. In other words, the model was found to be noticeably sensitive to the temporal variability of biomass burning emissions. Similar results have been found in other studies (e.g., Yamaguchi et al. (2023) and references therein).

Does this principle of the influence of interannual forcing variability on coupled earth system models extend from the biomass burning emissions to other forcings such as anthropogenic emissions of SO_2? The top panels of Fig. 5.4 show scatter plots of the AMOC anomly against the SPNA heat flux anomaly with no offset (panel a) and with an offset of 2 years (i.e., when the two timeseries displayed the highest degree of correlation in Fig. 5.3). As with previous plots, these scatter plots were generated with a bootstrapping method where many sub-ensemble mean AMOC and SPNA heat flux anomalies are compared to one another.

There is a clear relationship between these two variables, but it does not appear to be a simple linear relationship. Specifically, when the surface heat flux anomaly is positive the AMOC response is also positive, while when the surface heat flux anomaly is negative the AMOC response remains near zero. Put another way, the slope of the best fit line between AMOC and SPNA heat flux is much steeper (1.225 Sv/Wm^{-2} vs 0.025 Sv/Wm^{-2}) when the heat flux is positive than when it is negative. A piecewise regression using these two best fit lines against the full ensemble mean SPNA heat flux anomaly largely recreates the observed AMOC anomaly (panel c of Fig. 5.4).

This indicates the possibility of a nonlinear “rectifier" effect (e.g., Denning et al., 1999) in which positive deviations of the SPNA heat flux have a much larger influence on the AMOC than negative deviations of the same magnitude. From the boxplots in Fig. 5.3, CESM2-LE would tend to experience larger positive (as well as negative) deviations in the SPNA surface energy flux than either of the other ensembles, which may then be *rectified* onto the large positive AMOC anomaly seen in the top panel of Fig. 5.1. We propose that the larger interannual variability in CMIP6 compared to CMIP5 forcings may be the root cause of this observed effect.

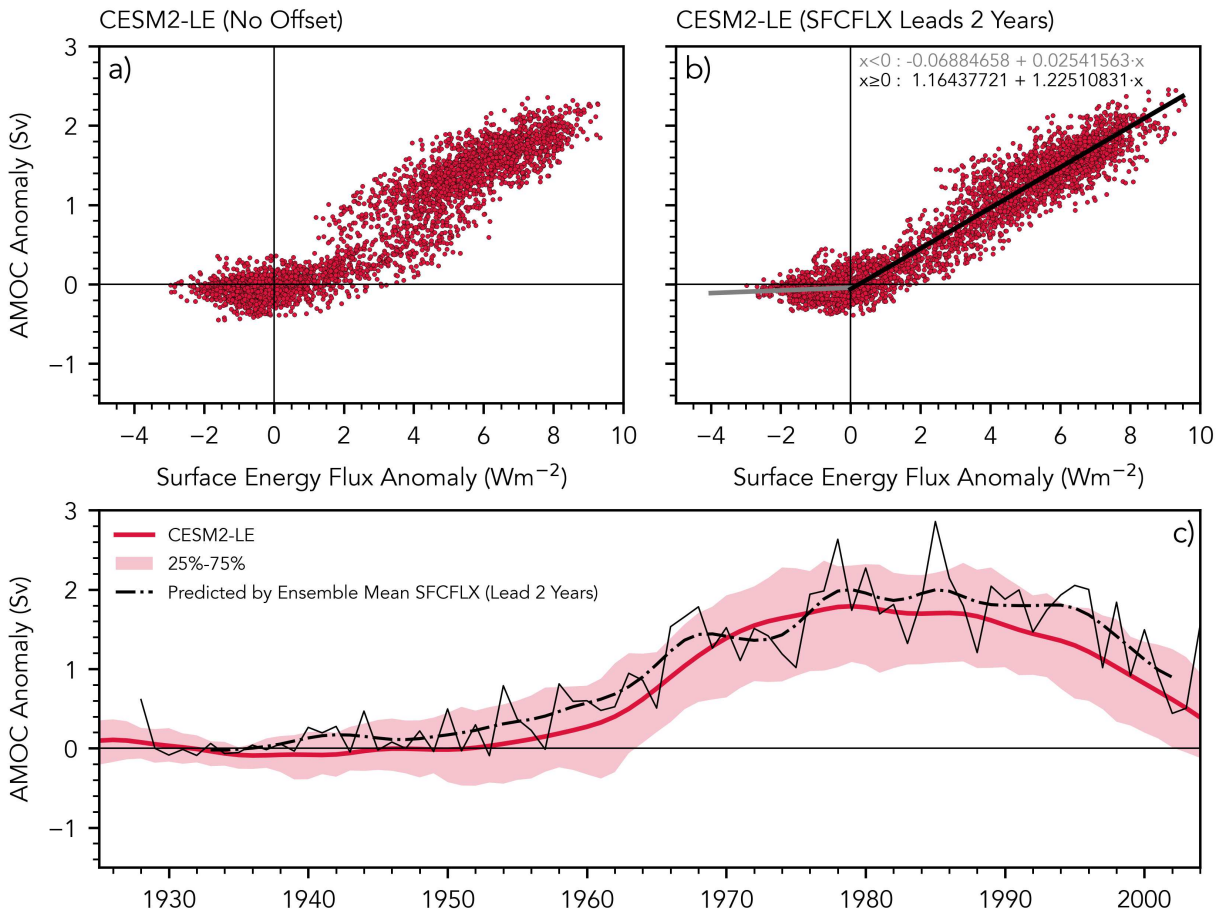

Figure 5.4: Top Row Scatter plots of the CESM2-LE AMOC and SFCFLX anomalies with no offset (**panel a**) and with a 2 year negative offset (e.g., AMOC lags SFCFLX by 3 years, **panel b**). Regression lines in **panel b** illustrate the non-linear "Rectifier" effect discussed in the text, where a positive anomaly in the SFCFLX leads to a larger anomaly in the AMOC compared to a negative anomaly of the same magnitude. **c)** Comparison of the AMOC anomaly "predicted" by the non-linear regression shown in the top right panel (thin solid line; thick dash-dotted line smoothed with the same 11-year gaussian filter) compared to the CESM2-LE ensemble mean AMOC anomaly.

5.6 Conclusion

We have shown that the AMOC response in CESM2 is highly sensitive to the interannual-variability of external forcings. When run with CMIP6 forcings, CESM2 exhibits an increase in the strength of the AMOC from 1940-1985, consistent with many other CMIP6 models (Menary et al., 2020) and *inconsistent* with proxy reconstructions (Rahmstorf et al., 2015; Thornalley et al., 2018; Caesar et al., 2018, 2021). The fact that this AMOC anomaly is absent in both the CESM1-LE and when CESM2 is forced by the older CMIP5 inputs establishes that this difference cannot be explained by differences in the model but must be due in large part to a change in forcings from CMIP5 to CMIP6.

Combined with the time-lagged correlation analysis (Fig. 5.3b), the fact that the spatially coherent heat flux anomaly seen in CESM2-LE (i.e., panel c of Fig. 5.2) is largely absent in CESM1-LE indicates that the turbulent heat flux anomaly is a strong contributor to the different AMOC response between CESM1-LE and CESM2-LE, as in Hassan et al. (2021) and Robson et al. (2022); the fact that it is also absent in CESM2-CMIP5 indicates that the appearance of the heat flux anomaly is primarily due to a change in external forcings. Thus we conclude that the change in forcings between CMIP5 and CMIP6 played a key role in the divergent AMOC response between CESM1-LE and CESM2-LE. We then proposed the hypothesis that increased interannual variability of CMIP6 emissions may be the root cause of the AMOC disagreement. This hypothesis is in line with recent work highlighting the impact of interannual variability of biomass burning emissions on CESM2 (e.g., Fasullo et al., 2022; Yamaguchi et al., 2023) although this may be the first evidence of a similar effect in a different forcing (i.e., anthropogenic emissions vs. biomass burning). We also suggested that a nonlinear relationship between the SPNA heat flux and the AMOC (a “rectifier effect") may be the mechanism that connects the interannual variability of emissions to the AMOC.

A key limitation of this work is that we have analyzed only a single model. This particular experimental setup (in which each ensemble utilized an atmospheric model which includes aerosol indirect effects, although with different representations) makes it impossible to com-

ment on the role of aerosol-cloud interactions on the AMOC across CMIP6 models except to say that those interactions did not play a role in the divergent AMOC response across CESM generations. However, we have no reason to believe that similar results would not be found if other models of the CMIP6 generation were forced by CMIP5 inputs. The stark differences between the AMOC response (Fig. 5.1) and the heat flux anomaly over the north Atlantic (Fig. 5.2 and panel a of Fig. 5.3) in CESM2-CMIP5 and CESM2-LE would indicate that similar experiments comparing the response of CMIP6-generation models under CMIP5 inputs should be performed to better understand the impact of changing forcings. Such experiments could also help to better understand the role of the representation of aerosol-cloud interactions for those models that included those processes for the first time in CMIP6.

References

Broecker, W. S. (1987). Unpleasant surprises in the greenhouse? http://dx.doi.org/10.1038/328123a0. Accessed: 2023-7-27.

Brovkin, V., Brook, E., Williams, J. W., Bathiany, S., Lenton, T. M., Barton, M., DeConto, R. M., Donges, J. F., Ganopolski, A., McManus, J., Praetorius, S., de Vernal, A., Abe-Ouchi, A., Cheng, H., Claussen, M., Crucifix, M., Gallopín, G., Iglesias, V., Kaufman, D. S., Kleinen, T., Lambert, F., van der Leeuw, S., Liddy, H., Loutre, M.-F., McGee, D., Rehfeld, K., Rhodes, R., Seddon, A. W. R., Trauth, M. H., Vanderveken, L., and Yu, Z. (2021). Past abrupt changes, tipping points and cascading impacts in the earth system. *Nat. Geosci.*, 14(8):550–558.

Buckley, M. W. and Marshall, J. (2015). Observations, inferences, and mechanisms of the atlantic meridional overturning circulation: A review. *Reviews of Geophysics*.

Caesar, L., McCarthy, G. D., Thornalley, D. J. R., Cahill, N., and Rahmstorf, S. (2021). Current atlantic meridional overturning circulation weakest in last millennium. *Nat. Geosci.*, 14(3):118–120.

Caesar, L., Rahmstorf, S., Robinson, A., Feulner, G., and Saba, V. (2018). Observed fingerprint of a weakening atlantic ocean overturning circulation. *Nature*, 556(7700):191–196.

Cheng, W., Chiang, J. C. H., and Zhang, D. (2013). Atlantic meridional overturning circulation (AMOC) in CMIP5 models: RCP and historical simulations. *J. Clim.*, 26(18):7187–7197.

Chiang, J. C. H., Cheng, W., and Bitz, C. M. (2008). Fast teleconnections to the tropical atlantic sector from atlantic thermohaline adjustment. *Geophys. Res. Lett.*, 35(7).

Danabasoglu, G., Lamarque, J.-F., Bacmeister, J., Bailey, D. A., DuVivier, A. K., Edwards, J., Emmons, L. K., Fasullo, J., Garcia, R., Gettelman, A., Hannay, C., Holland, M. M., Large, W. G., Lauritzen, P. H., Lawrence, D. M., Lenaerts, J. T. M., Lindsay, K., Lipscomb, W. H., Mills, M. J., Neale, R., Oleson, K. W., Otto-Bliesner, B., Phillips, A. S., Sacks, W., Tilmes, S., Kampenhout, L., Vertenstein, M., Bertini, A., Dennis, J., Deser, C., Fischer, C., Fox-Kemper, B., Kay, J. E., Kinnison, D., Kushner, P. J., Larson, V. E., Long, M. C., Mickelson, S., Moore, J. K., Nienhouse, E., Polvani, L., Rasch, P. J., and Strand, W. G. (2020). The community earth system model version 2 (CESM2). *J. Adv. Model. Earth Syst.*, 12(2).

Denning, A. S., Takahashi, T., and Friedlingstein, P. (1999). Can a strong atmospheric CO2 rectifier effect be reconciled with a "reasonable" carbon budget? *Tellus B Chem. Phys. Meteorol.*, 51(2):249–253.

Ditlevsen, P. and Ditlevsen, S. (2023). Warning of a forthcoming collapse of the atlantic meridional overturning circulation. *Nat. Commun.*, 14(1):4254.

Eyring, V., Bony, S., Meehl, G. A., Senior, C. A., Stevens, B., Stouffer, R. J., and Taylor, K. E. (2016). Overview of the coupled model intercomparison project phase 6 (CMIP6) experimental design and organization. *Geosci. Model Dev.*, 9(5):1937–1958.

Fasullo, J. T., Lamarque, J.-F., Hannay, C., Rosenbloom, N., Tilmes, S., DeRepentigny, P., Jahn, A., and Deser, C. (2022). Spurious late historical-era warming in CESM2 driven by prescribed biomass burning emissions. *Geophys. Res. Lett.*, 49(2).

Frierson, D. M. W., Hwang, Y.-T., Fučkar, N. S., Seager, R., Kang, S. M., Donohoe, A., Maroon, E. A., Liu, X., and Battisti, D. S. (2013). Contribution of ocean overturning circulation to tropical rainfall peak in the northern hemisphere. *Nat. Geosci.*, 6(11):940–944.

Gettelman, A. and Morrison, H. (2015). Advanced Two-Moment bulk microphysics for global models. part i: Off-Line tests and comparison with other schemes. *J. Clim.*, 28(3):1268–1287.

Hassan, T., Allen, R. J., Liu, W., and Randles, C. A. (2021). Anthropogenic aerosol forcing of the atlantic meridional overturning circulation and the associated mechanisms in CMIP6 models. *Atmos. Chem. Phys.*, 21(8):5821–5846.

Hoesly, R. M., Smith, S. J., Feng, L., Klimont, Z., Janssens-Maenhout, G., Pitkanen, T., Seibert, J. J., Vu, L., Andres, R. J., Bolt, R. M., Bond, T. C., Dawidowski, L., Kholod, N., Kurokawa, J.-I., Li, M., Liu, L., Lu, Z., Moura, M. C. P., O'Rourke, P. R., and Zhang, Q. (2018). Historical (1750–2014) anthropogenic emissions of reactive gases and aerosols from the community emissions data system (CEDS). *Geosci. Model Dev.*, 11(1):369–408.

Holland, M. M., Hannay, C., Fasullo, J., Jahn, A., Kay, J. E., Mills, M., Simpson, I. R., Wieder, W., Lawrence, P., Kluzek, E., and Bailey, D. (2023). New model ensemble reveals how forcing uncertainty and model structure alter climate simulated across CMIP generations of the community earth system model [Dataset].

Hoyer, S. and Hamman, J. J. (2017). xarray: N-D labeled arrays and datasets in python [Software]. *Journal of Open Research Software*, 5:304.

Hunter, J. D. (2007). Matplotlib: A 2d graphics environment [Software]. *Computing in Science & Engineering*, 9(3):90–95.

Hurrell, J. W., Holland, M. M., Gent, P. R., Ghan, S., Kay, J. E., Kushner, P. J., Lamarque, J.-F., Large, W. G., Lawrence, D., Lindsay, K., Lipscomb, W. H., Long, M. C., Mahowald, N., Marsh, D. R., Neale, R. B., Rasch, P., Vavrus, S., Vertenstein, M., Bader, D., Collins, W. D., Hack, J. J., Kiehl, J., and Marshall, S. (2013). The community earth system model: A framework for collaborative research. *Bull. Am. Meteorol. Soc.*, 94(9):1339–1360.

Kay, J. E., Deser, C., Phillips, A., Mai, A., Hannay, C., Strand, G., Arblaster, J. M., Bates, S. C., Danabasoglu, G., Edwards, J., Holland, M., Kushner, P., Lamarque, J.-F., Lawrence, D., Lindsay, K., Middleton, A., Munoz, E., Neale, R., Oleson, K., Polvani, L., and Vertenstein, M. (2015). The community earth system model (CESM) large ensemble project: A community resource for studying climate change in the presence of internal climate variability [Dataset]. *Bull. Am. Meteorol. Soc.*, 96(8):1333–1349.

Lamarque, J.-F., Bond, T. C., Eyring, V., Granier, C., Heil, A., Klimont, Z., Lee, D., Liousse, C., Mieville, A., Owen, B., Schultz, M. G., Shindell, D., Smith, S. J., Stehfest, E., Van Aardenne, J., Cooper, O. R., Kainuma, M., Mahowald, N., McConnell, J. R., Naik, V., Riahi, K., and van

Vuuren, D. P. (2010). Historical (1850–2000) gridded anthropogenic and biomass burning emissions of reactive gases and aerosols: methodology and application. *Atmos. Chem. Phys.*, 10(15):7017–7039.

Lenton, T. M., Rockström, J., Gaffney, O., Rahmstorf, S., Richardson, K., Steffen, W., and Schellnhuber, H. J. (2019). Climate tipping points - too risky to bet against. *Nature*, 575(7784):592–595.

Liu, W., Fedorov, A. V., Xie, S.-P., and Hu, S. (2020). Climate impacts of a weakened atlantic meridional overturning circulation in a warming climate. *Sci Adv*, 6(26):eaaz4876.

Liu, X., Ma, P.-L., Wang, H., Tilmes, S., Singh, B., Easter, R. C., Ghan, S. J., and Rasch, P. J. (2016). Description and evaluation of a new four-mode version of the modal aerosol module (MAM4) within version 5.3 of the community atmosphere model. *Geosci. Model Dev.*, 9(2):505–522.

Lozier, M. S., Li, F., Bacon, S., Bahr, F., Bower, A. S., Cunningham, S. A., de Jong, M. F., de Steur, L., deYoung, B., Fischer, J., Gary, S. F., Greenan, B. J. W., Holliday, N. P., Houk, A., Houpert, L., Inall, M. E., Johns, W. E., Johnson, H. L., Johnson, C., Karstensen, J., Koman, G., Le Bras, I. A., Lin, X., Mackay, N., Marshall, D. P., Mercier, H., Oltmanns, M., Pickart, R. S., Ramsey, A. L., Rayner, D., Straneo, F., Thierry, V., Torres, D. J., Williams, R. G., Wilson, C., Yang, J., Yashayaev, I., and Zhao, J. (2019). A sea change in our view of overturning in the subpolar north atlantic. *Science*, 363(6426):516–521.

Marshall, J., Donohoe, A., Ferreira, D., and McGee, D. (2013). The ocean's role in setting the mean position of the Inter-Tropical convergence zone. *Clim. Dyn.*, 42(7):1967–1979.

Menary, M. B., Robson, J., Allan, R. P., Booth, B. B. B., Cassou, C., Gastineau, G., Gregory, J., Hodson, D., Jones, C., Mignot, J., Ringer, M., Sutton, R., Wilcox, L., and Zhang, R. (2020). Aerosol-forced AMOC changes in CMIP6 historical simulations. *Geophys. Res. Lett.*, 47(14).

National Center for Atmospheric Research (2019). Computational and information systems laboratory. Title of the publication associated with this dataset: Cheyenne: HPE/SGI ICE XA System (Climate Simulation Laboratory).

Needham, M. R., Falter, D. D., and Randall, D. A. (2024). Changes in external forcings drive divergent AMOC responses across CESM generations. *Geophys. Res. Lett.*, 51(5).

Needham, M. R. and Randall, D. A. (2023). Anomalous northward energy transport due to anthropogenic aerosols during the 20th century. *J. Clim.*, -1(aop):1–37.

Rahmstorf, S. (2002). Ocean circulation and climate during the past 120,000 years. *Nature*, 419(6903):207–214.

Rahmstorf, S., Box, J. E., Feulner, G., Mann, M. E., Robinson, A., Rutherford, S., and Schaffernicht, E. J. (2015). Exceptional twentieth-century slowdown in atlantic ocean overturning circulation. *Nat. Clim. Chang.*, 5(5):475–480.

Robson, J., Menary, M. B., Sutton, R. T., Mecking, J., Gregory, J. M., Jones, C., Sinha, B., Stevens, D. P., and Wilcox, L. J. (2022). The role of anthropogenic aerosol forcing in the 1850–1985 strengthening of the AMOC in CMIP6 historical simulations. *J. Clim.*, 35(20):3243–3263.

Rodgers, K. B., Lee, S.-S., Rosenbloom, N., Timmermann, A., Danabasoglu, G., Deser, C., Edwards, J., Kim, J.-E., Simpson, I. R., Stein, K., Stuecker, M. F., Yamaguchi, R., Bódai, T., Chung, E.-S., Huang, L., Kim, W. M., Lamarque, J.-F., Lombardozzi, D. L., Wieder, W. R., and Yeager, S. G. (2021). Ubiquity of human-induced changes in climate variability [Dataset]. *Earth Syst. Dyn.*, 12(4):1393–1411.

Srokosz, M., Danabasoglu, G., and Patterson, M. (2021). Atlantic meridional overturning circulation: Reviews of observational and modeling advances—an introduction. *J. Geophys. Res. C: Oceans*, 126(1).

Thornalley, D. J. R., Oppo, D. W., Ortega, P., Robson, J. I., Brierley, C. M., Davis, R., Hall, I. R., Moffa-Sanchez, P., Rose, N. L., Spooner, P. T., Yashayaev, I., and Keigwin, L. D. (2018). Anomalously weak labrador sea convection and atlantic overturning during the past 150 years. *Nature*, 556(7700):227–230.

Trenberth, K. E. and Caron, J. M. (2001). Estimates of meridional atmosphere and ocean heat transports. *J. Clim.*, 14(16):3433–3443.

Trenberth, K. E. and Fasullo, J. T. (2017). Atlantc meridional heat transports computed from balancing earth's energy locally. *Geophys. Res. Lett.*, 44(4):1919–1927.

Wang, C., Soden, B. J., Yang, W., and Vecchi, G. A. (2021). Compensation between cloud feedback and aerosol-cloud interaction in CMIP6 models. *Geophys. Res. Lett.*, 48(4).

Worthington, E. L., Moat, B. I., Smeed, D. A., Mecking, J. V., Marsh, R., and McCarthy, G. D. (2021). A 30-year reconstruction of the atlantic meridional overturning circulation shows no decline. *Ocean Sci.*, 17(1):285–299.

Yamaguchi, R., Kim, J.-E., Rodgers, K. B., Stein, K., Timmermann, A., Lee, S.-S., Huang, L., Stuecker, M. F., Fasullo, J. T., Danabasoglu, G., Deser, C., Lamarque, J.-F., Rosenbloom, N. A., and Edwards, J. (2023). Persistent ocean anomalies as a response to northern hemisphere heating induced by biomass burning variability. *J. Clim.*, 36(23):8225–8241.

Chapter 6

Horizons

The tendency of contemporary scientific writing is to publish polished, self-contained studies of the type shown in the previous chapters. This suggests a neat, linear path of inquiry which follows the idealized five- to seven-step scientific method[6] that is taught to schoolchildren. In practice, the actual line of inquiry is winding, with numerous abandoned paths, double-backs, and dead-ends on the way to the eventual positive result - to say nothing of the difficulty around publishing bona fide null results (Kozlov, 2024).

My hope in this brief and admittedly speculative chapter is to illustrate some of the interesting results, thoughts, and observations over the course of the years spent on this project which - either due to time constraints, focus elsewhere, or simply because they did not fit with the story told by the primary chapters - were not developed into fully-fledged studies. These provide starting points for future work.

6.1 Nonlinear impacts of greenhouse gas forcing

This first topic stems from the second *Journal of Climate* article published out of this project (Ch. 4; i.e., Needham et al., 2024a). As part of that study, analysis of the CESM2 single-forcing large ensemble (CESM2-SF; Simpson et al., 2023) showed anomalous cross-equatorial energy transport by the atmosphere in the GHG-only and AAER-only simulations. When combined, the linear sum of the cross-equatorial energy transport across all of the CESM2-SF sub-ensembles was well outside of the ensemble spread from the main CESM2 large ensemble simulations (CESM2-LE; Rodgers et al., 2021). This discrepancy indicates a nonlinear response of the cross-equatorial atmospheric heat transport to CMIP6 aerosol and greenhouse-gas forcings in CESM2.

[6]For example, https://www.amnh.org/explore/videos/the-scientific-process

This observation immediately suggested a corresponding nonlinear response of the position of the Inter-tropical convergence zone (ITCZ) to greenhouse gas forcing, which is theorized to be closely coupled to the cross-equatorial atmospheric heat transport (Chiang and Bitz, 2005; Kang et al., 2008; Marshall et al., 2013; Frierson et al., 2013; Schneider et al., 2014; Adam et al., 2016; Donohoe and Voigt, 2017; Kang, 2020; Yukimoto et al., 2022). Further analysis identified such a shift (Fig. 4.2). However this interesting result could not be developed further because it was largely tangential to the primary focus of that study.

There are two key points here. First, the result itself raises a number of obvious questions which could likely be answered in a straightforward way as part of an independent study. The most glaring question, of course, is how does the isolated greenhouse gas forcing lead to a shift in the ITCZ: Does greenhouse gas-induced heating reduce high-latitude ice cover leading to a slowdown of the thermohaline circulation (e.g., Jackson et al., 2023) which requires a shift of the ITCZ to accomplish the necessary heat transport out of the tropics? Perhaps, or perhaps it is some other mechanism.

And there are a number of additional questions beyond the immediate question of how this process unfolds in the CESM2-SF and CESM2-LE simulations. Is this non-linearity is unique to the CESM2-SF, or are similar results are found in the older CESM1 single forcing large ensemble (Deser et al., 2020)? Similarly, is this non-linearity unique to the Community Earth System Model (either version 1 or 2), or are similar results found in any other climate models - for example, from the simulations submitted as part of the Detection and Attribution Model Intercomparion Project (DAMIP Gillett et al., 2016)? Can answering these “uniqueness" questions help to determine whether this effect stems from some intrinsic aspect of CESM (either version 1 or 2), or is it related to the greenhouse gas or other CMIP6 forcings?

Regardless of the answers to these questions, this example is the clearest instance I have come across to illustrate the utility of analyzing changes in the poleward energy transport and/or its constituent atmospheric and oceanic transports as a method to generate testable hypotheses on how an individual forcing or set of forcings impacts an earth system model.

6.2 Scalar Potentials

Another orphaned line of inquiry is that of the scalar potential of the heat transport vector field. The meridional heat transport discussed so extensively in this work can be understood as the zonal integral of the meridional component of the heat transport vector field (i.e., $\hat{e}_\varphi \cdot \mathbf{F}$). As with all vector fields, it can be decomposed[7] into the sum two other fields; one of which is divergent ($\mathbf{F}_\nabla$), and one of which is rotational ($\mathbf{F}_R$):

$$\mathbf{F} = \mathbf{F}_\nabla + \mathbf{F}_R = -\nabla\chi + \nabla \times \mathbf{A}. \tag{6.1}$$

Here, χ and $\mathbf{A}$ are then the *scalar* and the *vector* potential, respectively.

Although the divergent component is our primary interest here, it should be noted that there can be some reasons to investigate the rotational component. For example, Forget and Ferreira (2019) used the rotational component of the oceanic heat transport to visualize and ultimately subtract what they called closed "...ocean heat loops that do not immediately affect Earth's energy budget..." from the full ocean heat transport vector. This allowed for a better interpretation of direct measurements of oceanic heat transport as compared to gridded estimates.

Regardless, our primary reason to perform this decomposition is to investigate the divergent component, so we will ignore the rotational component and focus on the portion of F which can be defined as the gradient of some scalar potential χ:

$$\mathbf{F} \rightarrow \mathbf{F}_\nabla = -\nabla\chi. \tag{6.2}$$

Scalar potentials arise in many branches of mathematical physics including most famously in the classical theories of electrostatics and gravity (e.g., Griffiths, 2023). In electrostatics, the gradient of the electric potential q yields the electric field $\mathbf{E}$, and the divergence of $\mathbf{E}$ is proportional to the charge density. Then, given some arbitrary charge density ρ, a second order partial differential equation arises which can be solved to yield the electric potential, from which the

[7] this would be the vector field's Helmholtz decomposition

electric field is then calculated. This equation[8] takes the form of Poisson's equation for electrostatics:

$$\nabla \cdot \mathbf{E} = \nabla \cdot \big(-\nabla q \big) = \frac{1}{\varepsilon} \rho \rightarrow \nabla \cdot \nabla q = -\frac{\rho}{\epsilon}. \tag{6.3}$$

After deriving this equation, students of electrostatics then practice various methods of analytically solving Poisson's equation for a range of idealized charge density configurations.

All of the ingredients are present to follow this same recipe to calculate the divergent component of the heat transport vector field $\mathbf{F}_\nabla$ except that the corresponding Poisson's equation[9]:

$$\nabla^2 \chi = \nabla \cdot \mathbf{F}_\nabla = F_{toa} - F_{sfc} \tag{6.4}$$

cannot be solved analytically. However an approximate solution to this equation can be found with a numerical method known as Gauss-Seidel relaxation. The derivation of this method for spherical coordinates is not trivial (but is included in Appendix A), but the details are unimportant for our immediate purposes here. It is enough to know that it is *possible* to derive a numerical method to calculate the energy flux potential on the sphere based on the net energy flux across the top of atmosphere and the surface. And that this method can be implemented in a Python program[10]. The results of this method based on surface and TOA energy fluxes from ERA5 is shown in Fig. 6.1.

Caveats abound in these preliminary plots generated all the way back in 2021. The most obvious caveat is that taking the gradient of χ_{sfc} would indicate non-zero horizontal heat flux under the earth's surface over land (e.g., over north America). However, it is possible to see the broad-scale features of the meridional heat transport from these figures including maxima in the atmospheric heat transport in the mid-latitudes (i.e., where the gradient is sharpest),

[8] One of Maxwell's Equations

[9] here using $\nabla^2 \equiv \nabla \cdot \nabla$ for the Laplace operator

[10] which may require with an extensive amount of de-bugging and colorful language.

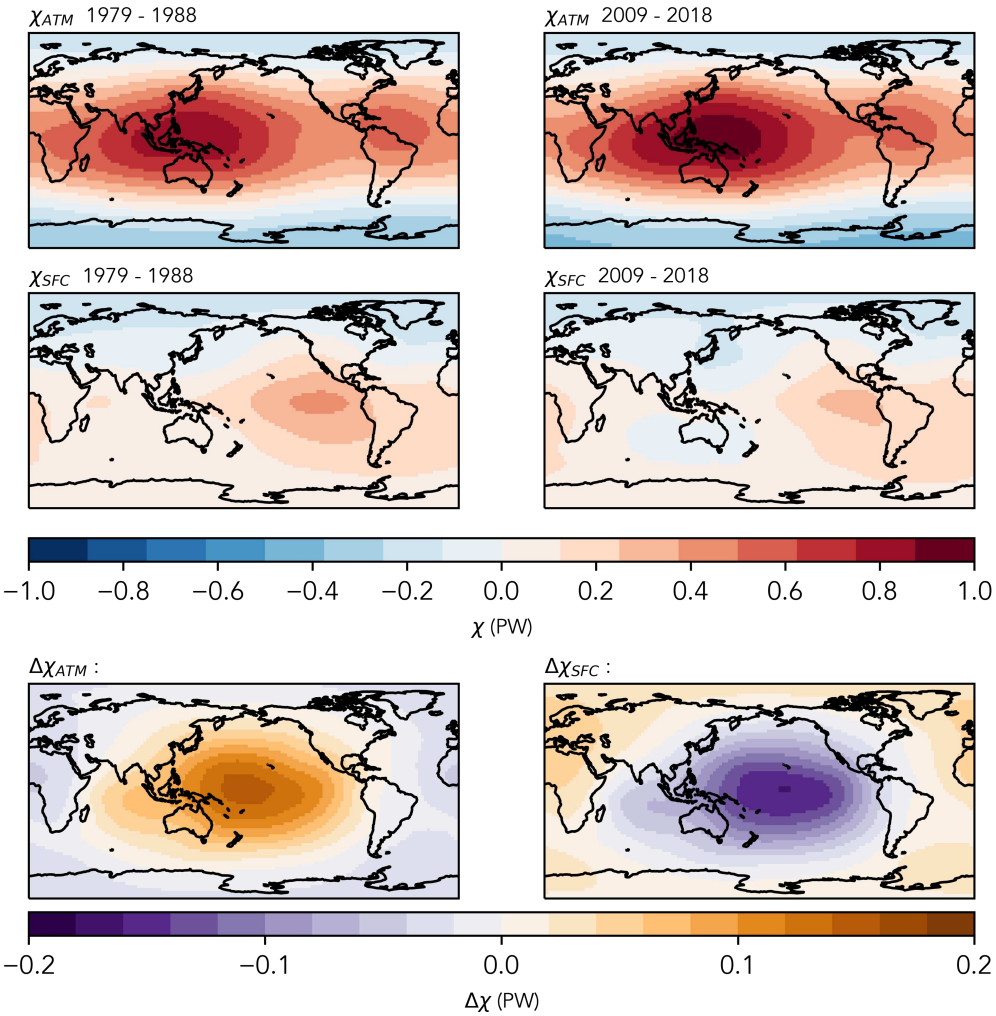

Figure 6.1: Top four panels show the heat flux potential χ calculated from ERA5 renalyses for the Atmosphere (top) and the surface (bottom). The left two plots are for the ten-year period from 1979-1988, while the right two plots were calculated from data from 2009-2018. The two plots in the bottom row show the *difference* in χ between the two time periods.

oceanic heat transport away from the equator in the Pacific, and a northward heat transport in the Atlantic which is not symmetric about the equator.

Before this line of inquary was supplanted by others, the goal was to calculate χ for each member of the CESM2 large ensemble, take the difference between χ at different times and from that difference investigate the ways in which energy moved throughout the climate system - resolved in both latitude and longitude instead of zonally integrated. Then, similar to the analysis in Ch. 4, differences in these heat transports would be matched to corresponding differences in various physical phenomena such as the AMOC, the Hadley cells, or extratropical

cyclones. In the plots in the bottom row of Fig. 6.1 (which again are from ERA5 and *not* from the CESM2-LE), changes in χ indicate compensating changes in Atmospheric and Oceanic heat transports across these two time periods, with an interesting spatial structure centered on the equatorial Pacific, which is reminiscent of the results of Forget and Ferreira (2019).

6.3 Temporal Variability of Emission Estimates

The final topic to be discussed here follows directly from the study published in *Geophysical Research Letters* and included in this dissertation as Ch. 5 (Needham et al., 2024b). The hypothesis raised by that study proposes that the change from decadal-scale emissions during CMIP5 (Lamarque et al., 2010) to annual-scale emissions during CMIP6 (Hoesly et al., 2018) may explain the enhanced model sensitivity to anthropogenic aerosol emissions seen in CESM2 compared to CESM1.

Fasullo et al. (2024) has found a similar (in fact, a *larger*) response to anthropogenic aerosols in a recent large ensemble performed with the U.S. Department of Energy's Energy Exascale Earth System Model (E3SM) version 2 (E3SM2). They found that anomalous heat transport in response to anthropogenic aerosols is not limited to CESM2 but is a characteristic of two additional large ensembles (i.e., E3SM1 and E3SM2). Crucially, both the E3SM1 and E3SM2 large ensembles were forced by CMIP6 inputs as was the CESM2 large ensemble. In contrast, the CESM1 large ensemble was forced by CMIP5 inputs, and *does not* shows a qualitatively different pattern in the heat transport anomaly, as shown in panel b of Fig. 6.2.

These pieces of evidence support the hypothesis that the overly-sensitive response of CESM2 (and E3SM1 and E3SM2) to historic anthropogenic aerosol forcing is due in large part to the changes in emissions between CMIP5 and CMIP6. One way to further test this hypothesis would be to perform an ensemble of simulations using CESM2 forced by CMIP6 emissions that have had anthropogenic aerosol emissions temporally smoothed with a gaussian filter which preserved the total mass of emissions on timescales longer than a year. This would fit with past precedent, as indeed half of the CESM2 large ensemble simulations were performed

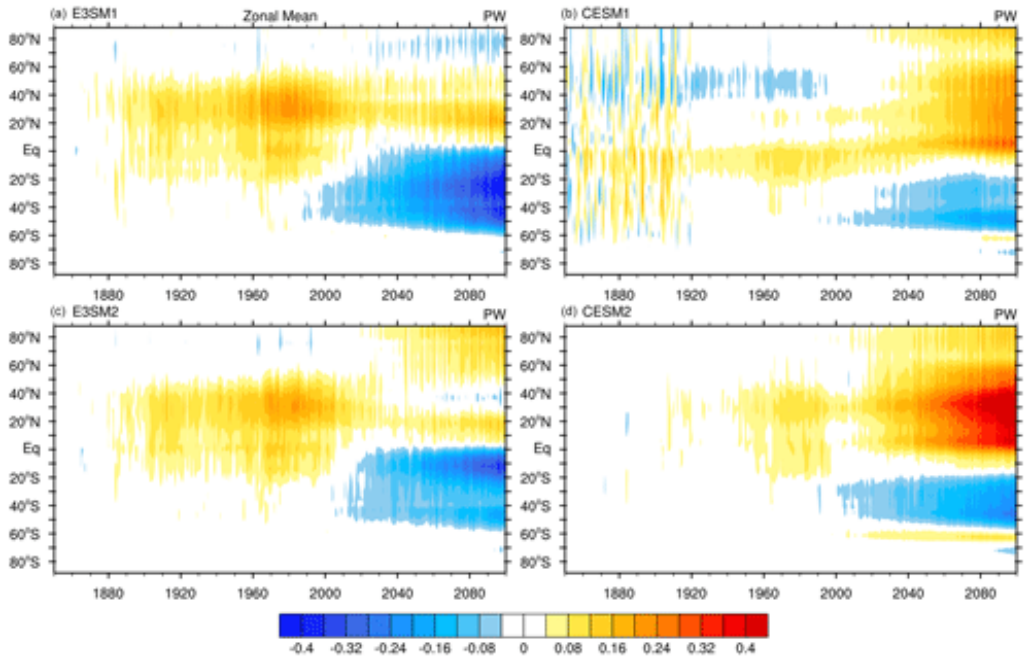

Figure 6.2: Anomaly in ensemble-mean total heat transport (PW) from four large ensembles. E3SM1 (panel a), E3SM2 (panel c) and CESM2 (panel d) all use the CMIP6 historical and SSP370 emission pathways, while CESM1 (panel b) uses the older CMIP5 historical and RCP8.5 scenario. Compare to Fig. 3.2. Originally published as Fig. 9 from Fasullo et al. (2024)

with smoothed *biomass burning* emissions. This change was made after it was found that the enhanced interannual variability of biomass burning emissions following the inclusion of satellite-derived estimates after 1997 led to spurious results (Fasullo et al., 2022). If these proposed simulations did not show the characteristic heat transport anomaly peak in the 1980s, then it would suggest that CESM2 (and perhaps E3SM1/2 as well).

A similar possibility would be to perform a small ensemble of simulations with CESM1 forced by CMIP6 emissions. This would essentially be the inverse of the CESM2-CMIP5 ensemble presented by Holland et al. (2024), and could be used to further probe the role of interannual emissions variability in the determination of the heat transport anomaly during the late twentieth century.

References

Adam, O., Bischoff, T., and Schneider, T. (2016). Seasonal and interannual variations of the energy flux equator and ITCZ. part i: Zonally averaged ITCZ position. *J. Clim.*, 29(9):3219–3230.

Chiang, J. C. H. and Bitz, C. M. (2005). Influence of high latitude ice cover on the marine intertropical convergence zone. *Clim. Dyn.*, 25(5):477–496.

Deser, C., Phillips, A. S., Simpson, I. R., Rosenbloom, N., Coleman, D., Lehner, F., Pendergrass, A. G., DiNezio, P., and Stevenson, S. (2020). Isolating the evolving contributions of anthropogenic aerosols and greenhouse gases: A new CESM1 large ensemble community resource. *J. Clim.*, 33(18):7835–7858.

Donohoe, A. and Voigt, A. (2017). Why future shifts in tropical precipitation will likely be small: The location of the tropical rain belt and the hemispheric contrast of energy input to the atmosphere. In Wang, S.-Y. S., Yoon, J.-H., Funk, C. C., and Gillies, R. R., editors, *Climate Extremes*, volume 6 of *Geophysical Monograph Series*, pages 115–137. John Wiley & Sons, Inc., Hoboken, NJ, USA.

Fasullo, J. T., Golaz, J.-C., Caron, J. M., Rosenbloom, N., Meehl, G. A., Strand, W., Glanville, S., Stevenson, S., Molina, M., Shields, C. A., Zhang, C., Benedict, J., Wang, H., and Bartoletti, T. (2024). An overview of the E3SM version 2 large ensemble and comparison to other E3SM and CESM large ensembles. *Earth Syst. Dyn.*, 15(2):367–386.

Fasullo, J. T., Lamarque, J.-F., Hannay, C., Rosenbloom, N., Tilmes, S., DeRepentigny, P., Jahn, A., and Deser, C. (2022). Spurious late historical-era warming in CESM2 driven by prescribed biomass burning emissions. *Geophys. Res. Lett.*, 49(2).

Forget, G. and Ferreira, D. (2019). Global ocean heat transport dominated by heat export from the tropical pacific. *Nat. Geosci.*, 12(5):351–354.

Frierson, D. M. W., Hwang, Y.-T., Fučkar, N. S., Seager, R., Kang, S. M., Donohoe, A., Maroon, E. A., Liu, X., and Battisti, D. S. (2013). Contribution of ocean overturning circulation to tropical rainfall peak in the northern hemisphere. *Nat. Geosci.*, 6(11):940–944.

Gillett, N. P., Shiogama, H., Funke, B., Hegerl, G., Knutti, R., Matthes, K., Santer, B. D., Stone, D., and Tebaldi, C. (2016). The detection and attribution model intercomparison project (DAMIP v1.0) contribution to CMIP6. *Geosci. Model Dev.*, 9(10):3685–3697.

Griffiths, D. J. (2023). *Introduction to Electrodynamics*. Cambridge University Press.

Hoesly, R. M., Smith, S. J., Feng, L., Klimont, Z., Janssens-Maenhout, G., Pitkanen, T., Seibert, J. J., Vu, L., Andres, R. J., Bolt, R. M., Bond, T. C., Dawidowski, L., Kholod, N., Kurokawa, J.-I., Li, M., Liu, L., Lu, Z., Moura, M. C. P., O'Rourke, P. R., and Zhang, Q. (2018). Historical (1750–2014) anthropogenic emissions of reactive gases and aerosols from the community emissions data system (CEDS). *Geosci. Model Dev.*, 11(1):369–408.

Holland, M. M., Hannay, C., Fasullo, J., Jahn, A., Kay, J. E., Mills, M., Simpson, I. R., Wieder, W., Lawrence, P., Kluzek, E., and Bailey, D. (2024). New model ensemble reveals how forcing uncertainty and model structure alter climate simulated across CMIP generations of the community earth system model. *Geosci. Model Dev.*, 17(4):1585–1602.

Jackson, L. C., Alastrué de Asenjo, E., Bellomo, K., Danabasoglu, G., Haak, H., Hu, A., Jungclaus, J., Lee, W., Meccia, V. L., Saenko, O., Shao, A., and Swingedouw, D. (2023). Understanding AMOC stability: the north atlantic hosing model intercomparison project. *Geoscientific Model Development*, 16(7):1975–1995.

Kang, S. M. (2020). Extratropical influence on the tropical rainfall distribution. *Current Climate Change Reports*, 6(1):24–36.

Kang, S. M., Held, I. M., Frierson, D. M. W., and Zhao, M. (2008). The response of the ITCZ to extratropical thermal forcing: Idealized slab-ocean experiments with a GCM. *J. Clim.*, 21(14):3521–3532.

Kozlov, M. (2024). So you got a null result. will anyone publish it? *Nature*, pages 728–730.

Lamarque, J.-F., Bond, T. C., Eyring, V., Granier, C., Heil, A., Klimont, Z., Lee, D., Liousse, C., Mieville, A., Owen, B., Schultz, M. G., Shindell, D., Smith, S. J., Stehfest, E., Van Aardenne, J., Cooper, O. R., Kainuma, M., Mahowald, N., McConnell, J. R., Naik, V., Riahi, K., and van Vuuren, D. P. (2010). Historical (1850–2000) gridded anthropogenic and biomass burning emissions of reactive gases and aerosols: methodology and application. *Atmos. Chem. Phys.*, 10(15):7017–7039.

Marshall, J., Donohoe, A., Ferreira, D., and McGee, D. (2013). The ocean's role in setting the mean position of the Inter-Tropical convergence zone. *Clim. Dyn.*, 42(7):1967–1979.

Needham, M. R., Cox, T., and Randall, D. A. (2024a). Aerosol-Induced changes in atmospheric and oceanic heat transports in the CESM2 large ensemble. *J. Clim.*, -1(aop).

Needham, M. R., Falter, D. D., and Randall, D. A. (2024b). Changes in external forcings drive divergent AMOC responses across CESM generations. *Geophys. Res. Lett.*, 51(5).

Rodgers, K. B., Lee, S.-S., Rosenbloom, N., Timmermann, A., Danabasoglu, G., Deser, C., Edwards, J., Kim, J.-E., Simpson, I. R., Stein, K., Stuecker, M. F., Yamaguchi, R., Bódai, T., Chung, E.-S., Huang, L., Kim, W. M., Lamarque, J.-F., Lombardozzi, D. L., Wieder, W. R., and Yeager, S. G. (2021). Ubiquity of human-induced changes in climate variability. *Earth Syst. Dyn.*, 12(4):1393–1411.

Schneider, T., Bischoff, T., and Haug, G. H. (2014). Migrations and dynamics of the intertropical convergence zone. *Nature*, 513(7516):45–53.

Simpson, I. R., Rosenbloom, N., Danabasoglu, G., Deser, C., Yeager, S. G., McCluskey, C. S., Yamaguchi, R., Lamarque, J.-F., Tilmes, S., Mills, M. J., and Rodgers, K. B. (2023). The CESM2 Single-Forcing large ensemble and comparison to CESM1: Implications for experimental design. *J. Clim.*, 36(17):5687–5711.

Yukimoto, S., Oshima, N., Kawai, H., Deushi, M., and Aizawa, T. (2022). Role of interhemispheric heat transport and global atmospheric cooling in multidecadal trends of northern hemisphere precipitation. *Geophys. Res. Lett.*, 49(18).

Chapter 7

Summary, Discussion, and Conclusions

7.1 Summary

The primary results of this dissertation can be simply stated. First, the simulations which comprise the CESM2 large ensemble (Rodgers et al., 2021) exhibit a large (roughly 0.25 PW) anomaly in the total poleward energy transport (PET) in historic simulations. This PET anomaly occurs across a range of latitudes from 30°S to 60°N, with a peak in the latter half of the twentieth century.

Second, the PET anomaly occurs due to the model's response to historic estimates of anthropogenic aerosol emissions. These emissions (Hoesly et al., 2018) are the same emissions used in the modeling protocol for the Coupled Model Intercomparison Project, phase 6 (Eyring et al., 2016).

Third, the PET anomaly was accomplished by changes in both atmospheric and oceanic processes. In the atmosphere, the mean meridional circulation exported additional energy northward (and less energy southward) out of the tropics; extratropical cyclones were found to be more frequent in the north Atlantic, which explains the observed increase in the eddy component of the atmospheric heat transport in the northern mid-latitudes. The major contribution to the ocean heat transport anomaly occurred in the Atlantic basin. Here, it was found that the Atlantic meridional overturning circulation (AMOC) strengthened in response to aerosol forcing, consistent with previous studies. The Kuroshio current off the coast of Japan was found to strengthen as well, and contributed to the (smaller) oceanic heat transport anomaly in the Pacific. The other factor in the Pacific was the the increase in basin-wide heat transport due to the Sverdrup transport associated with the subtropical ocean gyre. This contribution increased simply due to an increase in ocean heat uptake in the equatorial Pacific.

Fourth, it appears that the PET response to aerosols in the CESM2 large ensemble is too sensitive. This conclusion was reached because the AMOC response was found to be a major contributor to the PET anomaly, and because previous studies of CMIP6 models (Menary et al., 2020; Hassan et al., 2021; Robson et al., 2022) have indicated that similar large AMOC responses are inconsistent with proxy-derived estimates. The warmer sea surface temperature associated with the stronger AMOC also likely fueled the increase in the frequency of strong extratropical cyclones in the north Atlantic. This suggests that the change in extratropical cyclone statistics found in CESM2 may also be overestimated.

Fifth, the different AMOC response to anthropogenic aerosols across CESM generations was demonstrated to be driven primarily by changes in the estimates of historic anthropogenic aerosol emissions. This was shown through analysis of the CESM2 large ensemble, the CESM1 large ensemble (Kay et al., 2015), and the CESM2-CMIP5 ensemble (Holland et al., 2024). Specifically, when CESM2 was forced by the CMIP5 emissions, the model *did not* exhibit the characteristic peak in the latter half of the twentieth century that occurred when CESM2 was forced by CMIP6 emissions. Instead, the AMOC response in CESM2-CMIP5 much more closely followed the CESM1 large ensemble. This analysis also led to the hypothesis that CESM2 responds more strongly to the CMIP6 emissions because of the larger interannual variability that is the inevitable result of providing emission estimates on annual rather than decadal timescales (as with the CMIP5 emissions).

Finally, due to the strong link between AMOC and PET, this latter result suggests that the overly-sensitive PET anomaly in the CESM2 large ensemble is due to the change in anthropogenic aerosol emission forcing between CMIP5 (Lamarque et al., 2010) and CMIP6 (Hoesly et al., 2018).

7.2 Discussion

When considered as a whole, the analysis in this dissertation has shown that an extensively-used state-of-the-science earth system model (i.e., CESM version 2) appears to be overly-sensitive

to historic anthropogenic aerosol forcing. Overly-sensitive, that is, in response to the most recent annual estimates of anthropogenic pollutants which were used as inputs to historic simulations submitted as part CMIP6.

These studies raise additional questions concerning the response of CESM2 (and other state-of-the-science earth system models, such as E3SM2; see Fasullo et al. (2024)) to CMIP6 emissions, two of which were discussed in Ch. 6. To understand the first of these questions, it should be first noted that recent work by Simpson et al. (2023) has indicated a nonlinear response of the AMOC to anthropogenic aerosols in CESM2. The second study in this dissertation (i.e., Ch. 3; Needham and Randall, 2023) demonstrated for the first time that CESM2 also responds nonlinearly to greenhouse gases. This raises the question of whether and to what extent analysis of the greenhouse-gas only simulations from the CESM2 single-forcing large ensemble should be understood to truly represent the isolated impact of greenhouse gases in the wider context of the full CESM2 large ensemble simulations. In other words, analysis of those GHG-only simulations should interpreted with caution because they may not translate seamlessly to the all-forcing simulations.

The second question is to what degree does the interannual variability of emissions (i.e., comparing the temporal resolution of CMIP5 and CMIP6 emissions) explain the divergent response of the AMOC to anthropogenic aerosol forcing between CMIP5 and CMIP6 models; and what other physical phenomena (e.g., the ITCZ?) may be impacted by this change in emission timescales. Additionally, to what degree are these sensitivities unique to CESM2 compared to other earth system models? And lastly, to what extent these results are relevant to the so-called "hot-model" problem among some CMIP6 models (Hausfather et al., 2022). Could higher interannual variability of emissions (including, but not necessarily limited to aerosol emissions) play some role?

The answers to these questions must be left to future work.

7.3 Conclusions

Of the myriad topics available for study in the broadly-defined fields of atmospheric science and climatology, what can be gained through the investigation of poleward energy transport? The heat transport cannot be measured directly from observations[11], and yet it manages to touch some of the most important processes in the atmosphere and oceans. In a field which is governed by notoriously complicated equations[12] there is a certain appeal to this relatively simple argument derived from the Divergence theorem (Eq. 2.1) which ultimately relates many aspects of the earth system back to the basics of orbital geometry and albedo (Stone, 1978).

A sub-theme of these studies has been to demonstrate that analysis of the poleward energy transport can efficiently suggest lines of inquiry which may not otherwise be immediately obvious. Take the change in extratropical cyclones discussed in (Ch. 4; Needham et al., 2024) as an example. Given a new set of simulations (i.e., the CESM2 large ensemble), analysis of the eddy atmospheric heat transport indicated a large signal in the northern mid-latitudes (see panel D of Fig. 4.3), which was attributed to a change in the frequency of extratropical cyclones. This path from "new set of simulations" to "change in atmospheric eddy heat transport" to "change in extratropical cyclones" is *extremely short*, all things considered; and yet, without the analysis of the atmospheric eddy heat transport there may not have been any reason to look at extratropical cyclones in the first place. In other words, the interesting result that extratropical cyclone statistics changed meaningfully in CESM2 in response to CMIP6 anthropogenic aerosol forcing may not have been found if not for the analysis of the heat transport.

Lastly, it is important to acknowledge that all of the results contained within this dissertation *without exception* came from analysis of large ensembles of climate model simulations. Each of the more than 250 simulations analyzed as part of these studies contained terabytes of model output which needed to be queried, filtered, analyzed, summarized, used as the basis of further calculations, and ultimately visualized to arrive at final results. This dissertation

[11] it must instead be *inferred* through the polar cap or vertical integration methods discussed in previous chapters

[12] See the millennium prize related to the Navier-Stokes equations

was an exercise in data analysis and high performance computing *at least* as much as it was an exercise in physical climatology. This highlights that our field is currently at an inflection point which represents both a major challenge *and* a major opportunity. The vast quantities of data generated *every day* from model output, reanalyses, and observations must somehow be systematized, analyzed, and interpreted in order to arrive at meaningful conclusions about the past, present, and future of our climate. This necessity to leverage our ever-increasing computational resources to manage our ever-increasing quantities of data will only become more important as time progresses.

References

Eyring, V., Bony, S., Meehl, G. A., Senior, C. A., Stevens, B., Stouffer, R. J., and Taylor, K. E. (2016). Overview of the coupled model intercomparison project phase 6 (CMIP6) experimental design and organization. *Geosci. Model Dev.*, 9(5):1937–1958.

Fasullo, J. T., Golaz, J.-C., Caron, J. M., Rosenbloom, N., Meehl, G. A., Strand, W., Glanville, S., Stevenson, S., Molina, M., Shields, C. A., Zhang, C., Benedict, J., Wang, H., and Bartoletti, T. (2024). An overview of the E3SM version 2 large ensemble and comparison to other E3SM and CESM large ensembles. *Earth Syst. Dyn.*, 15(2):367–386.

Hassan, T., Allen, R. J., Liu, W., and Randles, C. A. (2021). Anthropogenic aerosol forcing of the atlantic meridional overturning circulation and the associated mechanisms in CMIP6 models. *Atmos. Chem. Phys.*, 21(8):5821–5846.

Hausfather, Z., Marvel, K., Schmidt, G. A., Nielsen-Gammon, J. W., and Zelinka, M. (2022). Climate simulations: recognize the 'hot model' problem. `http://dx.doi.org/10.1038/d41586-022-01192-2`. Accessed: 2024-8-7.

Hoesly, R. M., Smith, S. J., Feng, L., Klimont, Z., Janssens-Maenhout, G., Pitkanen, T., Seibert, J. J., Vu, L., Andres, R. J., Bolt, R. M., Bond, T. C., Dawidowski, L., Kholod, N., Kurokawa, J.-I., Li, M., Liu, L., Lu, Z., Moura, M. C. P., O'Rourke, P. R., and Zhang, Q. (2018). Historical (1750–2014) anthropogenic emissions of reactive gases and aerosols from the community emissions data system (CEDS). *Geosci. Model Dev.*, 11(1):369–408.

Holland, M. M., Hannay, C., Fasullo, J., Jahn, A., Kay, J. E., Mills, M., Simpson, I. R., Wieder, W., Lawrence, P., Kluzek, E., and Bailey, D. (2024). New model ensemble reveals how forcing uncertainty and model structure alter climate simulated across CMIP generations of the community earth system model. *Geosci. Model Dev.*, 17(4):1585–1602.

Kay, J. E., Deser, C., Phillips, A., Mai, A., Hannay, C., Strand, G., Arblaster, J. M., Bates, S. C., Danabasoglu, G., Edwards, J., Holland, M., Kushner, P., Lamarque, J.-F., Lawrence, D., Lindsay, K., Middleton, A., Munoz, E., Neale, R., Oleson, K., Polvani, L., and Vertenstein, M. (2015). The community earth system model (CESM) large ensemble project: A community resource for studying climate change in the presence of internal climate variability. *Bull. Am. Meteorol. Soc.*, 96(8):1333–1349.

Lamarque, J.-F., Bond, T. C., Eyring, V., Granier, C., Heil, A., Klimont, Z., Lee, D., Liousse, C., Mieville, A., Owen, B., Schultz, M. G., Shindell, D., Smith, S. J., Stehfest, E., Van Aardenne, J., Cooper, O. R., Kainuma, M., Mahowald, N., McConnell, J. R., Naik, V., Riahi, K., and van Vuuren, D. P. (2010). Historical (1850–2000) gridded anthropogenic and biomass burning emissions of reactive gases and aerosols: methodology and application. *Atmos. Chem. Phys.*, 10(15):7017–7039.

Menary, M. B., Robson, J., Allan, R. P., Booth, B. B. B., Cassou, C., Gastineau, G., Gregory, J., Hodson, D., Jones, C., Mignot, J., Ringer, M., Sutton, R., Wilcox, L., and Zhang, R. (2020). Aerosol-forced AMOC changes in CMIP6 historical simulations. *Geophys. Res. Lett.*, 47(14).

Needham, M. R., Cox, T., and Randall, D. A. (2024). Aerosol-Induced changes in atmospheric and oceanic heat transports in the CESM2 large ensemble. *J. Clim.*, -1(aop).

Needham, M. R. and Randall, D. A. (2023). Anomalous northward energy transport due to anthropogenic aerosols during the twentieth century. *J. Clim.*, 36(19):6713–6728.

Robson, J., Menary, M. B., Sutton, R. T., Mecking, J., Gregory, J. M., Jones, C., Sinha, B., Stevens, D. P., and Wilcox, L. J. (2022). The role of anthropogenic aerosol forcing in the 1850–1985 strengthening of the AMOC in CMIP6 historical simulations. *J. Clim.*, 35(20):3243–3263.

Rodgers, K. B., Lee, S.-S., Rosenbloom, N., Timmermann, A., Danabasoglu, G., Deser, C., Edwards, J., Kim, J.-E., Simpson, I. R., Stein, K., Stuecker, M. F., Yamaguchi, R., Bódai, T., Chung, E.-S., Huang, L., Kim, W. M., Lamarque, J.-F., Lombardozzi, D. L., Wieder, W. R., and Yeager, S. G. (2021). Ubiquity of human-induced changes in climate variability. *Earth Syst. Dyn.*, 12(4):1393–1411.

Simpson, I. R., Rosenbloom, N., Danabasoglu, G., Deser, C., Yeager, S. G., McCluskey, C. S., Yamaguchi, R., Lamarque, J.-F., Tilmes, S., Mills, M. J., and Rodgers, K. B. (2023). The CESM2 Single-Forcing large ensemble and comparison to CESM1: Implications for experimental design. *J. Clim.*, 36(17):5687–5711.

Stone, P. H. (1978). Constraints on dynamical transports of energy on a spherical planet. *Dyn. Atmos. Oceans*, 2(2):123–139.

Gauss-Seidel Relaxation with Latitude-Longitude Spherical Coordinates

Introduction

Poisson's Equation

The difference between the energy flux across the TOA and the Surface is equal to the divergence of energy within the atmosphere. We can represent this with a scalar potential q that satisfies

$$\nabla^2 q = \nabla \cdot \mathbf{F_E} = F_{toa} - F_{sfc}.$$

The above is an example of Poisson's Equation,

$$\nabla^2 q = -f, \tag{1}$$

which is a more general form of Laplace's Equation[13],

$$\nabla^2 q = 0 \tag{2}$$

Poisson's and Laplace's equations are examples of second-order partial differential equations. Analytic solutions exist for a select number of problems in mathematics and physics, but for a system like the atmosphere we will solve this equation using an iterative relaxation method known as Gauss-Seidel under-relaxation.

[13] The symbol ∇^2 is known as the Laplacian or the Laplace operator, and is defined as the divergence of the gradient, $\nabla^2 = \nabla \cdot \nabla$

Relaxation Methods

Under specific conditions, Eqs. 1 and 2 may be solved to find an analytic expression for q. As we are looking for the solution given an arbitrary scalar field $F_{toa} - F_{sfc}$, we must instead rely on numerical methods. As an example, we will consider Eq. 1 on a one-dimensional Cartesian grid, and then generalize to our spherical grid.

Relaxation on a one-dimensional grid

In one (Cartesian) dimension, Eq. 1 reduces to

$$\frac{d^2q}{dx^2} = -f. \tag{3}$$

This differential equation[14] can be solved using the methods of a college differential equations course. It will serve to illustrate the concept of building a numeric method to find an (approximate) solution.

First, we must discretize Eq. 3 onto our one-dimensional grid with uniform grid spacing d. Our strategy will be to take the derivative of q on our grid, and then take the derivative of that result. This leads to

$$\left(\frac{d^2q}{dx^2}\right)_i \approx \frac{q_{i-1} + q_{i+1} - 2q_i}{d^2}. \tag{4}$$

Here, q_i refers to the value of q at grid cell i, with equivalent definitions for q_{i-1} and q_{i+1}. Plugging this into Eq. 3 yields

$$\frac{q_{i-1} + q_{i+1} - 2q_i}{d^2} = -f_i. \tag{5}$$

Our strategy will be to start with a guess[15] of the value of q at each grid cell. Then we will repeatedly update our guess at a grid cell based on the value of f at that grid cell (which does

[14] now an *ordinary* differential equation, in constrast to the *partial* differential equations of the first section.

[15] It doesn't have to be a *good* guess, a uniform field of zeros will do!

not change) and the value of guess on nearby grid cells. It may not be *a priori* obvious that this strategy will work, but in practice it does a pretty good job. For notation, we will define $\hat{q}_i$ to refer to our guess of a solution to Eq. 3 at grid cell i; ${\hat{q}_i}^{new}$ and ${\hat{q}_i}^{old}$ will refer to the most recent and second-most recent guess of our solution at i, respectively. Let's algebraically solve Eq. 5 for q_i, and replace all q with $\hat{q}$, to show our iterative method.

$$ {\hat{q}_i}^{new} = \frac{1}{2}\left(d^2 f_i + \hat{q}_{i-1}^{old} + \hat{q}_{i+1}^{old}\right) \tag{6} $$

Successive iteration of Eq. 6 will lead to a solution that *converges* to the exact solution to Eq. 5, given appropriate boundary conditions. Essentially, we will sweep over the grid to calculate a new field $\hat{q}^{new}$, replace $\hat{q}^{old}$ with the values of $\hat{q}^{new}$, and repeat until the approximate solution does not change[16] between iterations. The accuracy of the solution can be tested by taking the second derivative of the solution and comparing it to the input, f. If our method were perfect then these two fields would agree exactly, but in practice we should see very good but imperfect agreement.

It can be shown[17] that a single change to Eq. 6 can greatly increase the speed of convergence. Essentially, we can use a hybrid of new and old values in our guess for $\hat{q}_i$. If we assume that our sweep begins at $i = 0$ and ends at $i = n$, then we change $\hat{q}_{i+1}^{old}$ to $\hat{q}_{i+1}^{new}$, which yields

$$ {\hat{q}_i}^{new} = \frac{1}{2}\left(d^2 f_i + \hat{q}_{i-1}^{new} + \hat{q}_{i+1}^{old}\right) \tag{7} $$

Eq. 7 is an example of *Gauss-Seidel* relaxation, in contrast to Eq. 6, which is an example of *Jacobi* relaxation.

[16] Does not change *much*, whatever that means in practice...

[17] But will be glossed-over here

Under-Relaxation

From Eqs. 6 and 7 we notice that the guess for $\hat{q}_i$ incorporates values at grid cells $i-1$ and $i+1$, but not the value at i. This can lead to a checkerboard error where our solution fails to converge and instead flips between two states. This can be avoided with a technique known as *under*-relaxing. To begin, we add and subtract $\hat{q}^{old}$ to the right hand side of Eq. 7:

$$\hat{q}_i{}^{new} = \hat{q}_i{}^{old} + \left[\frac{1}{2}\left(d^2 f_i + \hat{q}_{i-1}^{new} + \hat{q}_{i+1}^{old}\right) - \hat{q}_i{}^{old}\right] \tag{8}$$

which simply states that our new guess is equal to our old guess plus some small change. The checkerboard issue occurs because our solution changes too much between iterations and flips between two states. This can be overcome by reducing the size of our increment by a factor $0 < \omega < 1$

$$\hat{q}_i{}^{new} = \hat{q}_i{}^{old} + \omega\left[\frac{1}{2}\left(d^2 f_i + \hat{q}_{i-1}^{new} + \hat{q}_{i+1}^{old}\right) - \hat{q}_i{}^{old}\right] \tag{9}$$

which simplifies to

$$\hat{q}_i{}^{new} = (1-\omega)\,\hat{q}_i{}^{old} + \omega\left[\frac{1}{2}\left(d^2 f_i + \hat{q}_{i-1}^{new} + \hat{q}_{i+1}^{old}\right)\right]. \tag{10}$$

On the spherical grid

An arbitrary grid cell

We now want to derive an equivalent expression to Eq. 10 on our longitude (λ) and latitude (φ) spherical coordinate system. A general grid cell in this system is a trapezoid bound by lines of longitude and latitude, as shown in Fig. A1. The values of q are defined at the center of each cell, and the cell is bounded by lines of longitude and latitude, with angular spaing $\Delta\lambda$ and $\Delta\varphi$.

We begin by deriving an expression for the Laplacian $\nabla^2 q$ using the finite volume method whereby the divergence theorem allows us to write the divergence in terms of a surface integral. Specifically,

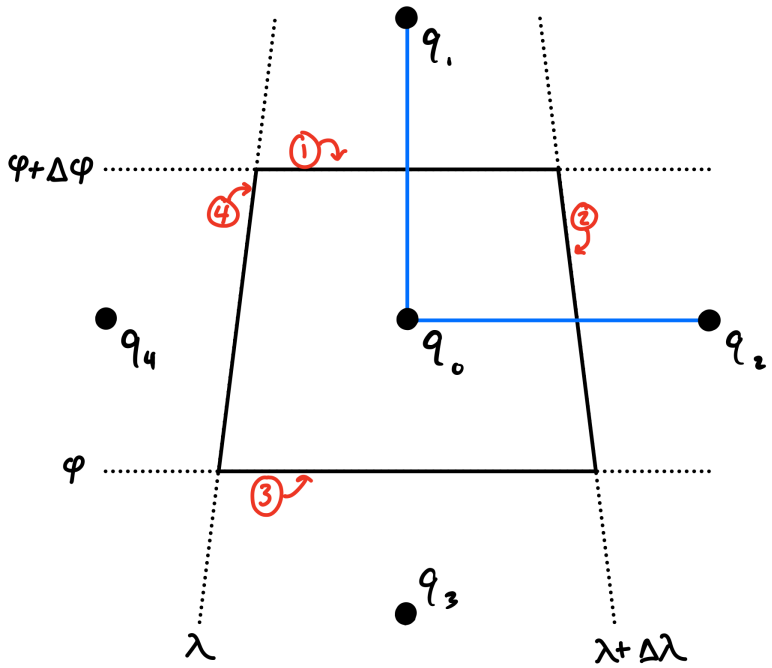

Figure A1: Schematic for an arbitrary (non-polar) grid cell.

$$\nabla^2 q \approx \frac{1}{A} \oint_{\mathscr{C}} (\hat{\mathbf{n}} \cdot \nabla q) dl \tag{11}$$

Here, A refers to the area bounded by curve $\mathscr{C}$, and $\hat{\mathbf{n}} \cdot \nabla q$ is the component of ∇q that is normal to $\mathscr{C}$. For our coordinate system, A is the area of the trapezoid in Fig. A1 and $\mathscr{C}$ is simply the boundary of the trapezoid.

Briefly, let's define some shorthand to simplify our derivation. First, we define

$$m_i = \cos(\varphi_i). \tag{12}$$

Note that φ_i refers to the latitude of the *center* of the grid cell (this will be important later). With this in mind we can define the values of m needed for our derivation:

$$
\begin{aligned}
m_1 &\equiv \cos(\varphi + \Delta\varphi) \\
m_0 &\equiv \cos(\varphi + \frac{\Delta\varphi}{2}) \\
m_3 &\equiv \cos(\varphi)
\end{aligned}
\tag{13}
$$

The numbers 1 and 3 above refer to the value on cell edge 1 and 3. We also simplify our indexing method as

$$
\begin{aligned}
q_0 &\equiv q_{i,j} \\
q_1 &\equiv q_{i,j+1} \\
q_2 &\equiv q_{i+1,j} \\
q_3 &\equiv q_{i,j-1} \\
q_4 &\equiv q_{i-1,j}
\end{aligned}
\tag{14}
$$

Lastly, the area A of the trapezoid is given by

$$
A = \frac{b1 + b2}{2} h = \frac{m_1 + m3}{2} r_e^2 \Delta\lambda\Delta\varphi \approx m_0 r_e^2 \Delta\lambda\Delta\varphi \tag{15}
$$

The approximation here is an assumption that

$$
\cos(\varphi + \frac{\Delta\varphi}{2}) \approx \frac{\cos(\varphi + \Delta\varphi) + \cos(\varphi)}{2} \tag{16}
$$

which is fine as long as the grid spacing isn't too large.

Back to the main event. We now will work through evaluating the integral in Eq. 11 on the trapezoid.

$$
\begin{aligned}
\nabla^2 q &= \frac{1}{A}\oint_{\mathscr{C}} (\hat{\mathbf{n}}\cdot\nabla q)\,dl \\
&= \frac{1}{m_0 r^2 \Delta\lambda\Delta\varphi}\left[\frac{q_1-q_0}{r\Delta\varphi} r\, m_1 \Delta\lambda + \frac{q_4-q_0}{r\, m_0\Delta\lambda} r\Delta\varphi - \frac{q_0-q_3}{r\Delta\varphi} r\, m_3\Delta\lambda - \frac{q_0-q_2}{r\, m_0\Delta\lambda} r\Delta\varphi\right] \\
&= \frac{1}{m_0 r^2}\left[\frac{q_1-q_0}{(\Delta\varphi)^2} m_1 + \frac{q_4-q_0}{m_0(\Delta\lambda)^2} - \frac{q_0-q_3}{(\Delta\varphi)^2} m_3 - \frac{q_0-q_2}{m_0(\Delta\lambda)^2}\right]
\end{aligned}
\tag{17}
$$

This is our discretization of the Laplacian. Now, following the method above we insert this into Eq. 1 and solve for q_0

$$
\begin{aligned}
\frac{q_1-q_0}{(\Delta\varphi)^2} m_1 + \frac{q_4-q_0}{m_0(\Delta\lambda)^2} - \frac{q_0-q_3}{(\Delta\varphi)^2} m_3 - \frac{q_0-q_2}{m_0(\Delta\lambda)^2} &= -m_0 r_e^2 f_0 \\
\frac{q_1 m_1 + q_3 m_3}{(\Delta\varphi)^2} + \frac{q_2+q_4}{m_0(\Delta\lambda)^2} - \left(\frac{m_1+m_3}{(\Delta\varphi)^2} + \frac{2}{m_0(\Delta\lambda)^2}\right) q_0 &= -m_0 r_e^2 f_0 \\
q_0 &= \frac{-m_0 r_e^2 f_0 - \frac{q_1 m_1 + q_3 m_3}{(\Delta\varphi)^2} - \frac{q_2+q_4}{m_0(\Delta\lambda)^2}}{-\left(\frac{m_1+m_3}{(\Delta\varphi)^2} + \frac{2}{m_0(\Delta\lambda)^2}\right)}
\end{aligned}
\tag{18}
$$

Simplifying, and using the relaxation notation as in Eq. 6,

$$
\hat{q}_0^{new} = \left(m_0 r_e^2 f_0 + \frac{m_1 \hat{q}_1^{old} + m_3 \hat{q}_3^{old}}{(\Delta\varphi)^2} + \frac{\hat{q}_2^{old} + \hat{q}_4^{old}}{m_0(\Delta\lambda)^2}\right)\left(\frac{m_1+m_3}{(\Delta\varphi)^2} + \frac{2}{m_0(\Delta\lambda)^2}\right)^{-1} \tag{19}
$$

If we choose to use Gauss-Seidel relaxation then two of the $\hat{q}_i^{old}$ terms will flip to $\hat{q}_i^{new}$, but exactly *which* terms will depend on the order of the sweep. Lastly, we can convert this into an *under-relaxation* algorithm by adding and subtracting by $\hat{q}_0^{old}$ on the right side, and multiplying the increment by our factor $0.5 \le \omega < 1$.

$$
\boxed{\hat{q}_0^{new} = (1-\omega)\,\hat{q}_0^{new} + \omega\left(m_0 r_e^2 f_0 + \frac{m_1 \hat{q}_1^{old} + m_3 \hat{q}_3^{old}}{(\Delta\varphi)^2} + \frac{\hat{q}_2^{old} + \hat{q}_4^{old}}{m_0(\Delta\lambda)^2}\right)\left(\frac{m_1+m_3}{(\Delta\varphi)^2} + \frac{2}{m_0(\Delta\lambda)^2}\right)^{-1}} \tag{20}
$$

This will work everywhere on our grid... except at the poles.

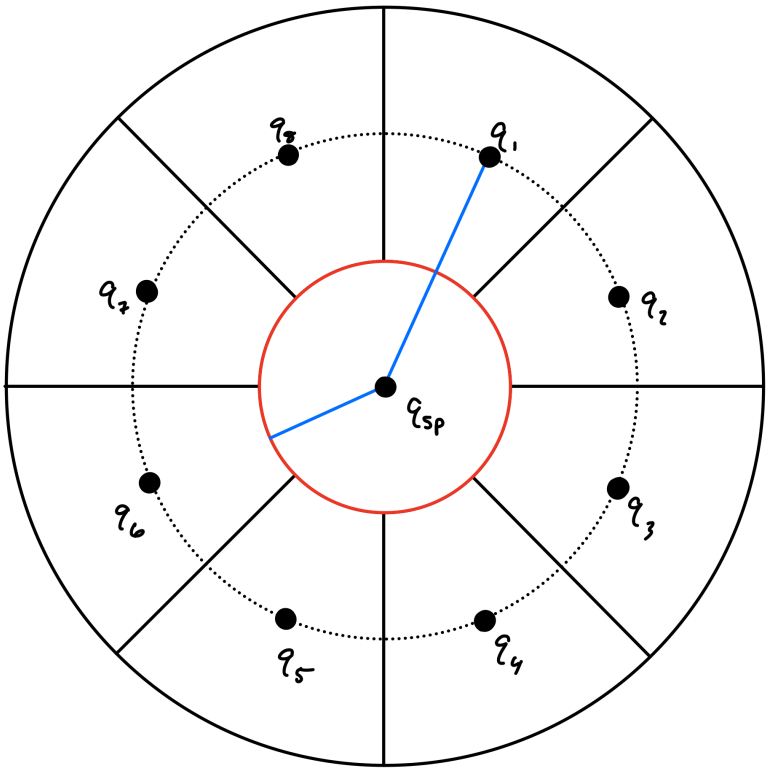

Figure A2: Schematic for a polar-cap grid cell.

Overcoming the Pole Problem

Unfortunately, the existence of the poles complicates our algorithm. We can get around this by defining a local “polar cap" coordinate system as illustrated in Fig. A2. Our data, stored digitally, is almost certainly rectangular, meaning that the number of grid cells at 90°S is equal to the number of grid cells at the equator, although they represent much smaller portions of the globe.

Our strategy will be to calculate the Laplacian for a single grid cell at 90° and them apply it uniformly to all grid cells which have a coordinate $\varphi = 90°$. In the figure, q_{SP} refers to the grid cell at the south pole, and q_1 through q_8 refer to all of the grid cells that border this imaginary polar cap[18].

[18] in practice there will almost certainly be more than 8 grid cells here, but this serves to illustrate the point